Molecular Beam Epitaxy and Characterization of Heterostructures with ZnCdSSe Quaternary Alloys for Light-Emitting Devices

December 1993

Kunio Ichino

Molecular Beam Epitaxy and Characterization of Heterostructures with ZnCdSSe Quaternary Alloys for Light-Emitting Devices

December 1993

Kunio Ichino

Acknowledgements

Contents

Chapter 1

Introduction

In these days, there is an increasing requirement for short wavelength light-emitting devices which operate in the spectral region from blue-green to ultraviolet (UV) [1,2]. For example, if blue light-emitting diodes (LEDs) with high luminance and efficiency are realized, full-color flat-panel LED displays can be constructed using the blue LEDs together with red and green LEDs ever available. It is considered that such LED displays will replace other displays, i.e., Braun tubes, liquid crystal and thin film electroluminescent displays [3] in some applications, and each of these will be used for its suitable purpose. On the other hand, infrared semiconductor laser diodes (LDs) operating at $\lambda \approx 780$ nm have widely been used for optical memories such as video and compact discs, and higher storage density is achieved today by using red ($\lambda \approx 670$ nm) LDs [4]. If the wavelength of laser can be altered to blue or UV, the storage bit density of the optical memory significantly increases [5]. In the application in laser printers, blue/UV lasers enhance printing speed by one or two orders of magnitude [2]. Furthermore, UV light-emitting devices will widely be used as compact light sources for measurement or medical applications.

For these applications, wide bandgap II-VI semiconductors such as ZnSe and ZnS (bandgap E_g=2.7 eV [6] and 3.73 eV [7] at room temperature (RT), respectively), as well as SiC [8–10] and GaN [11–14], have long been considered as promising materials [1]. However, the difficulty in obtaining p-type conduction remained to be solved [15]. Consequently, in the late 1970's and early 1980's, blue LEDs were fabricated using metal-insulator-semiconductor (MIS) structures with bulk ZnSe [16–19] and ZnS [20–25]. However, device characteristics and reproducibility were not satisfactory. Afterward, Nishizawa *et al.* reported p-type conduction in ZnSe and pn-junction blue LED by using a temperature difference method under controlled vapor pressure [26]. However, these results did not lead to the practical use to date. On the other hand, since the late 1970's, much attention has been paid to reduce intrinsic defects and

1

extrinsic residual impurities in ZnSe and ZnS by using new growth techniques, such as metal-organic vapor phase epitaxy (MOVPE) [27–32] and molecular beam epitaxy (MBE) [33–39]. In particular, for ZnSe, several groups reported p-type conduction by using MOVPE [40–42] or MBE [43,44] or metalorganic molecular beam epitaxy (MOMBE) [45]. However, the problem in reproducibility on electrical and optical properties were still remain unresolved.

Recently, a practical p-type doping level in ZnSe was demonstrated when nitrogen plasma source was used during MBE [46,47]. On the other hand, it became possible to make ZnSe-based high-quality heterostructures such as ZnSe-ZnMnSe [48,49], ZnSe-ZnSSe [50–52], ZnCdSe-ZnSe [53,54], ZnCdSe-ZnSSe [55] and Zn(S)Se-ZnMgSSe [56,57] by MBE and MOVPE. Laser operation by optical pumping was achieved in these structures. This success led to first operation of II-VI LDs operating in the blue-green spectral region [58,59] in 1991, and the first RT cw operation of blue-green LDs [60] in 1993. High efficiency blue LEDs have also been reported by using similar ZnSe-based structures [61].

On the other hand, for ZnS, only a few reports on p-type conduction have been made [62,63]. Although low resistive p-ZnS with a carrier concentration of the order of 10^{18} cm^{-3} grown by vapor phase epitaxy was reported [64], optical properties of p-ZnS were rather poor to fabricate efficient LEDs based on pn junction. Furthermore, technology for reproducible p-type ZnS crystals with quality high enough for device application has not been established yet. Structural control of heterostructures, as will be shown later, is also recognized to be inferior to that of ZnSe-based structures.

Toward practical device applications of these II-VI wide bandgap materials in the near future, many problems to be solved remain for further development. They can be classified into two major subjects: (1) for the practical use of blue/blue-green light emitting devices based on ZnSe-based structures, further improvement of the device structure as well as the quality of constituent layers are strongly desired; (2) it is required to shorten the emission wavelength toward the UV spectral region as the next target after blue/blue-green devices.

For the former subject, electrical and optical properties have still to be improved through the fundamental characterization of the layers as well as the development of growth technique to control material properties. At the same time, device structure should also be improved for more efficient carrier confinement and light emission. Currently, most II-VI blue-green light-emitting devices are composed of ZnCdSe quantum wells (QWs) with small sulfur content as barrier layers [65–70]. In designing such structure, as will be described in Chapter 2, there are severe restrictions such as emission wavelength, band-offsets, strain, and so on. In fact, the first LD

structure, having the ZnSe/ZnSSe wave guide as well as the ZnCdSe QW, contained a large number of misfit dislocations [58,59], which probably cause deterioration of device performance. Consequently, there is only small room for improvements of the device structure as long as the ZnCdSe/Zn(S)Se QW system is used. Therefore, development of new material system which increases flexibility in designing device structure is required. One of the approaches for this objective is the use of Zn(S)Se/ZnMgSSe system on GaAs, which was proposed by Okuyama *et al.* in 1991 [71]. This material system may have high potential for blue/blue-green LDs, because the bandgap can be varied under the lattice-matched condition like the conventional GaAs/AlGaAs or InGaAsP/InP system. In fact, the first RT cw operation of blue-green LDs was achieved using the Zn(S)Se/ZnMgSSe system on GaAs [60], although the life of the LD was several second. However, the stronger reactivity of magnesium than that of aluminum and the strong ionicity of MgSe and MgS may cause defects or difficulty in controlling physical properties, which may make it difficult to realize practical blue/blue-green light-emitting devices or more shorter wavelength devices.

For the latter subject, it is necessary to develop a new material system instead of the ZnSe-based structures, because it is impossible to shorten operating wavelength toward the UV spectral region using the ZnSe-based structures. For this purpose, ZnS is one of the possible candidates. However, unlike ZnSe, growth technique of high quality ZnS epitaxial layers in terms of crystallographic and optical properties has not been well established yet. In particular, reliable and reproducible p-type conduction has not been achieved as mentioned above. These results may be related to the high vapor pressure of sulfur or the stronger ionicity of ZnS than that of ZnSe. Recently, ZnCdS/ZnS multiple QWs on GaAs substrates were proposed for UV light-emitting devices [72,73] and successful results of stimulated emission by optical pumping [74,75] and current injection [76] have been reported. However, large lattice-mismatch between ZnS and GaAs (4.5 %) results in defects, which may be obstacle for the practical use. Therefore, a new material system using ZnS-based structures including the appropriate choice of substrates should be developed, and, at the same time, epitaxial growth technique of such ZnS-based structures should also be improved for the control of crystallographic, optical and electrical properties.

From the overview of background and present status of wide-bandgap II-VI semiconductors toward blue/blue-green and UV/near-UV light-emitting devices, it is strongly suggested to develop ZnCdSSe quaternary alloys, which would allow novel and flexible structural design of QWs. ZnCdSSe quaternary alloys with the composition close to ZnSe or ZnS are applicable to blue/blue-green or UV/near-UV light-emitting devices, respectively. The first success in epitaxial growth of ZnCdSSe

was reported in 1991 by MOVPE [77]. Before this report, it had been considered that high quality ZnCdSSe could not be grown because CdS and CdSe have hexagonal crystal structure, and growth technique for the II-VI semiconductor was not well sophisticated to control the composition of such multitudinous alloys with constituent elements having high vapor pressure. Among several physical parameters of ZnCdSSe needed for the design of light-emitting devices, the lattice constant and bandgap were estimated in the earlier publications [77, 78]. However, to design heterostructure devices, band-offsets are also important parameters. In addition, for the application of ZnCdSSe quaternary alloys for practical light-emitting devices, the layers should be subjected to strain in order to achieve carrier confinement heterostructures, as will be described later. Therefore, structural design with ZnCdSSe quaternary alloys including band-offsets should be carried out taking into account the strain effects on band structures and critical thickness, which was not considered in the earlier publications [77, 78]. Furthermore, MBE-based technique including metalorganic MBE (MOMBE) and gas-source MBE (GSMBE) is suitable for the growth of heterostructures with the uniform thickness and abrupt interfaces, and fundamental discussion of growth characteristics based on *in situ* monitoring.

In this study, on the basis of these backgrounds, the ZnCdSSe quaternary alloy is introduced to the design and the fabrication of short-wavelength light-emitting devices for the first time. The purpose of this study is (1) to estimate physical parameters of ZnCdSSe and to design heterostructures for light-emitting devices taking lattice strain into account and (2) to investigate growth and characteristics of epitaxial layers and their heterostructures for the application to light-emitting devices. The investigations are carried out both for blue/blue-green and for UV/near-UV light-emitting devices with ZnSe-based structures on GaAs substrates and ZnS-based structures on GaP substrates, respectively. Since the MBE technique of ZnS-based structures is not well established compared to that of ZnSe-based structures, a lot of efforts have been made for the growth of ZnS-based UV/near-UV light-emitting device structures.

Following this chapter, in Chapter 2, physical parameters are estimated in detail, and pseudomorphic light-emitting device structures with ZnCdSSe quaternary alloys are proposed and designed for the first time. In Chapter 3, MOMBE and characterization of ZnCdSSe quaternary alloys on GaAs substrates are described. Some characteristics of optically pumped lasing in ZnSe-based multi-layered structures with ZnCdSSe are also described. Chapters 4 and 5 concern with ZnS-based structures. In Chapter 4, gas-source molecular beam epitaxy (GSMBE) and characterization are described, while MBE using an elemental sulfur source and characterization are

presented in Chapter 5. In Chapter 5, fabrication of MIS LEDs is also described, and it is shown that near-UV electroluminescence is observed for the first time at 77 K from the LED with a pseudomorphic ZnCdSSe/ZnSSe quantum well, Finally, the results obtained in this study are summarized in Chapter 6.

Chapter 2

Structural design of short wavelength light-emitting devices using ZnCdSSe quaternary alloys

2.1   Introduction

Wide bandgap II-VI semiconductors such as ZnSe and ZnS have long been considered to be promising materials, and optical properties of their bulk crystals have been extensively investigated since 1950's [79–82]. On the other hand, for III-V semiconductors, the development of the heterostructure devices [83,84] has led to great success since the first cw operation of GaAs/AlGaAs double-heterostructure (DH structure) laser diodes (LDs) at room temperature (RT) [85]. In recent years, attempts have also been made for II-VI semiconductors to fabricate heterostructures, owing to great improvements of epitaxial growth technique. In early attempts, ZnSe/ZnMnSe [49] ZnSe/ZnTe [86,87], ZnSe/ZnS [87–89] and ZnSe/ZnSSe [50] heterostructures have been grown. However, since bulk CdS, CdSe, ZnCdS and ZnCdSe have hexagonal wurzite structure, it had been considered that they cannot construct heterostructure with cubic zinc blende ZnS, ZnSe and ZnSSe. Recently, it was shown that cubic CdS [90], ZnCdS [91,92], CdSe [93], and ZnCdSe [94] can be grown epitaxially on cubic GaAs substrates by metalorganic vapor phase epitaxy (MOVPE) or molecular beam epitaxy (MBE), and various heterostructures such as CdS/ZnS [90,95], ZnCdS/ZnS [72,73], ZnCdSe/ZnSe [94] and ZnCdSe/ZnSSe [55], which showed good optical properties, have been fabricated. On the other hand, no attempts have been made to grow ZnCdSSe quaternary alloy except a preliminary study by MOVPE [77].

For the use of ZnCdSSe quaternary alloy in short wavelength light-emitting devises, it is important to estimate various physical parameters of the ZnCdSSe system.

7

Among these parameters, lattice-constant and bandgap of ZnCdSSe have already estimated in earlier publications [77,78]. However, for the design of heterostructure devices, band-offsets between constituent layers are also important. In addition, as will be described later, since strained layers must be used for carrier confinement in this material system, strain effects should be taken into account in the estimation of band structure of each layer, and critical thickness of the strained layers should also be estimated. Furthermore, refractive indices are needed to estimate optical confinement factor of LDs.

In this Chapter, after describing lattice constant and bandgap without strain, band-edge energies of ZnCdSSe without strain are estimated [96,97]. The estimation of refractive index is also presented. To construct pseudomorphic device structure, the use of two substrates, i.e., GaAs and GaP, are proposed. Bandgap and band-offsets of the ZnCdSSe system are calculated for each case taking strain effects into account [98,99]. Calculation of the critical thickness of strained layer is also presented. On the basis of these parameters, several device structures with ZnCdSSe quaternary alloys are proposed [96,97,99]. The physical parameters used in the calculations as well as other values reported so far are listed in Tables 2.1–2.4. In this chapter, The calculation is carried out using RT values for practical applications, while in the following chapter the low temperature values are sometimes used for comparison with experimental results such as 4.2 K photoluminescence. At present, there remain several parameters which are not reliable, but are used for the design of the devices in the present study as a first trial. Those values should be corrected by the characterization of the designed and fabricated structure.

2.2   Physical parameters

2.2.1   Lattice constant

Lattice constant of the alloy was derived using Vegard's law. For $Zn_{1-x}Cd_xS_ySe_{1-y}$ quaternary alloys, lattice constant a is given by

$$a = (1-x)(1-y)a_{ZnSe} + (1-x)y\,a_{ZnS} + x(1-y)a_{CdSe} + xy\,a_{CdS} \qquad (2.1)$$

where a_{ZnS} denotes lattice constant of ZnS, and so on. Calculated results for whole composition area of $Zn_{1-x}Cd_xS_ySe_{1-y}$ is shown in Fig. 2.1. The solid lines represent compositions where lattice-constant is equal, and dashed lines indicate composition where lattice constant is equal to that of a III-V compound substrate. Since high-quality substrates of II-VI compounds are not readily available, III-V compounds or group-IV semiconductors are used as substrates for epitaxial growth. If group-IV

Table 2.1: Lattice constant and bandgap of binary compounds. The parameters used in this study are marked with "*".

Compound	Lattice constant (Å)	Bandgap (eV)		~ 0K
		RT		
ZnS	*5.4093[a]	3.69[c]	3.711[b]	3.83[f]
	5.4110[b]	*3.73[d]		3.78[e]
		3.68[e]		*3.84[g]
ZnSe	5.6687[a]	2.713[i]	*2.70[e]	2.82[e]
	*5.6681[b]	2.69[c]	2.695[b]	2.8201[j]
	5.6676[h]	2.724[d]		*2.8218[k]
CdS	5.820[a]	*2.355[m]		*2.46
	*5.832[l]			
CdSe	*6.05[a,l]	*1.691[m]		*1.77[n']
	6.077[n]	1.67[n]		

a   Roth [100] (1967).
b   Ebina *et al.* [101] (1982).
c   Ebina *et al.* [102] (1974).
d   Camassel [7] (1975).
e   Theis [6] (1979).
f   Shionoya [79] (1966).
g   Taguchi *et al.* [103] (1961).
h   Mohammed *et al.* [104] (1987).
i   Ebina *et al.* [105] (1974).
j   Venghaus [106] (1979).
k   Dean *et al.* [107] (1981).
l   Kiriyama *et al.* [108] (1979).
m   Tai *et al.* [109] (1976).
n   Samarth *et al.* [93] (1989).
n' Binding energy of free exciton is added to the result in ref. [93].

Table 2.2: Effective masses in binary compounds reported so far. The parameters used in this study are marked with "*". Several values are those for hexagonal materials, and are defined as "(hex)".

Compound	Effective mass (m^*/m_0)			
	electron		hole	
	m_e^*		m_{hh}^*	$m_{hh,\langle 100 \rangle}^*$ [1]
ZnS	*0.34[a]	0.262[d]	1.76[b]	*0.95[b',e]
	0.28[b]	0.23[e]		0.700[c]
	0.184[c]			1.036[d]
ZnSe	0.1[f]	0.130[c]	0.6[f]	*0.78[b',e]
	0.17[g]	0.135[j]	0.75[m]	0.546[c]
	0.14[b,e]	0.147[k]	1.44[b]	0.784[d]
	0.16[h]	0.173[d]	0.60[n]	
	*0.160[i]	0.145[l]	0.894[o]	
CdS	*0.20(hex)[p]	0.16[e]	1.25[q]	0.929[d]
	0.209[d]			*1.11[e]
CdSe	*0.13(hex)[r]	0.14[e]	1.23[q]	*0.78[e]

1. In a quantum well layered toward $\langle 100 \rangle$ direction and subjected to compressive strain (mainly treated case in this study), ground state of the hole bands is n=1 heavy hole state, and the energy level of the top of the state can be calculated using heavy-hole mass along $\langle 100 \rangle$ direction, $m_{hh,\langle 100 \rangle}^*$ [110, 111].

a. Kukimoto et.al. [112] (1968).

b. Lawaetz [113] (1971); calculation.

b'. Calculated from Luttinger parameters [114] given in ref. [113] according to the equation $m_{hh,\langle 100 \rangle}^* = (\gamma_1 - 2\gamma_2)^{-1}$ [110,111].

c. Wang et al. [115] (1981); calculation.

d. Huang et al.[116] (1985); calculation.

e. Nakayama [117] (1993); calculation.

f. Aven et al.[118] (1961).

g. Marple [119] (1964).

h. Mertz et al. [120] (1972).

i. Dean et al. [107] (1981).

j. Ohyama et al. [121] (1984).

k. Hölscher et al. [122] (1985).

l. Isshiki et al. [123] (1987).

m. Hite et al. [124] (1967).

n. Ruda [125] (1986); calculation.

o. Ohyama et al. [126] (1987).

p. Hopfield [127] (1961).

q. Harrison [128] (1980); calculation.

r. Wheeler et al. [129] (1962).

Table 2.3: Other physical parameters of binary compounds used in this study.

Compound	Valence-band-edge energy[a] (eV)	Spin-orbit splitting energy Δ_0 (eV)	Elastic stiffness constant		Deformation potential[b]		
			C_{11}	C_{12}	a_c	a_v	b
			$(\times 10^{11} \mathrm{dyn/cm^2})$			(eV)	
ZnS	−11.40	0.45[c]	10.46[e]	6.53[e]	−4.09	2.31	−1.25
ZnSe	−10.58	0.072[d]	8.10[e]	4.88[e]	−4.17	1.65	−1.20
CdS	−11.12		7.79[f]	5.27[f]			
CdSe	−11.35		6.67[f]	4.63[f]			

a   Harrison [128] (1980).
b   Shahzad *et al.* [130] (1988).
c   Aven *et al.* [118] (1961).
d   Segall *et al.* [131] (1967).
e   Berlincourt *et al.* [132] (1963).
f   Martin [133] (1972); transformation from values for hexagonal materials.

Table 2.4: Bowing parameters for ternary alloys reported so far. The parameters used in this study are marked with "*". The values for hexagonal materials are defined as "(hex)".

Alloy	Bowing parameter	Ref. and Comments.
ZnSSe	0.63	Ebina *et al.* [105] (1974), Soonckindt *et al.* [134] (1979).
	*0.41	Suslina *et al.* [135] (1977).
ZnCdS	*0.3(hex)	Hill [136] (1974).
ZnCdSe	0.75	Tai *et al.* [137] (1977).
	*0.30	This value is calculated results in ref. [138] and fits with experimental values in ref. [94] rather well.
CdSSe	*0.54(hex)	Hill [136] (1974).
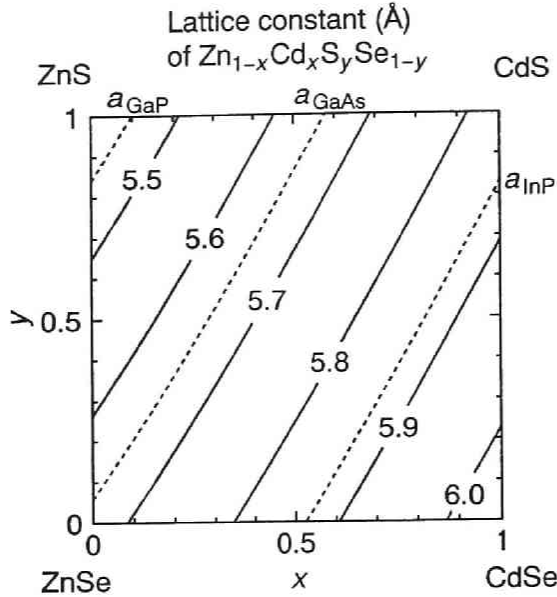
Figure 2.1: The x-y compositional plane for $Zn_{1-x}Cd_xS_ySe_{1-y}$ quaternary alloy system. The x-y coordinate of any point in the plane gives the composition. The solid lines indicate the compositions for lattice constant inserted in the figure. The dashed lines indicate the compositions at which lattice constant is equal to that of III-V compound substrate.

semiconductors are used as substrates for epitaxial growth of II-VI semiconductor, it will be difficult to avoid anti-phase domains. Therefore, the use of III-V compounds seems to be better.

As shown in Fig. 2.1, $Zn_{1-x}Cd_xS_ySe_{1-y}$ can be lattice-matched to three III-V compounds, GaP, GaAs and InP, all of which are readily available. When GaAs is used, two kinds of ternary alloys, $ZnS_{0.06}Se_{0.94}$ and $Zn_{0.42}Cd_{0.58}S$, and $Zn_{1-x}Cd_x$-S_ySe_{1-y} quaternary alloys with composition between above two ternary alloys can be lattice-matched, as seen from the figure. As for GaP, $ZnS_{0.86}Se_{0.14}$, $Zn_{0.90}Cd_{0.10}S$ and $Zn_{1-x}Cd_xS_ySe_{1-y}$ between these can be lattice-matched.

If a lattice-mismatched layer is grown beyond critical thickness, misfit dislocations and related defects are generated. Since these defects affect the performance and lifetime of the light-emitting devices, the devices should be designed on the basis of pseudomorphic structure to the substrates. Thus, for each substrate, the composition area of the epitaxial layers is restricted.
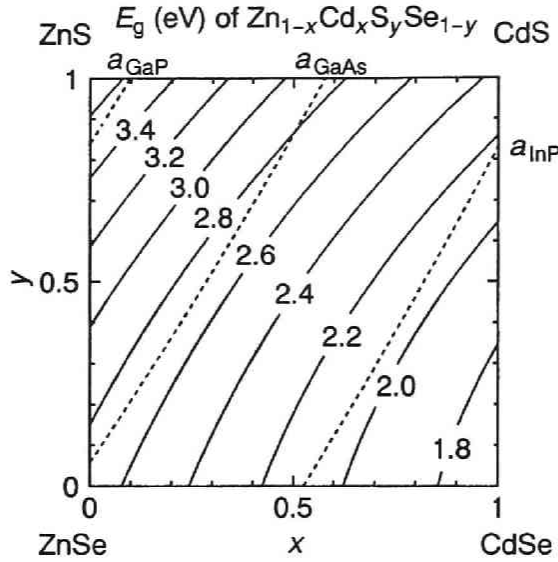
Figure 2.2: Calculated equi-bandgap-energy line in $Zn_{1-x}Cd_xS_ySe_{1-y}$ at RT. The compositions for lattice-matching to III-V substrates are also shown with dashed lines.

2.2.2 Bandgap

Bandgap (E_g) was calculated using the procedure proposed by Sasaki *et al.* [83] for III-V alloy semiconductors. Results at RT are shown in Fig. 2.2. The lines represent compositions where bandgap energy is equal. The compositions for lattice-matching to III-V substrates are also shown with dashed lines. When lattice-matched structure to a GaAs substrate is assumed, bandgap of $Zn_{1-x}Cd_xS_ySe_{1-y}$ is about 2.7–2.8 eV, which corresponds to the blue spectral region. As for GaP and InP substrates, bandgap of $Zn_{1-x}Cd_xS_ySe_{1-y}$ is around 3.5 eV (ultraviolet; UV) and 2.1 eV (orange), respectively. Since the purpose of the present work is to construct short wavelength light-emitting devices, the structures on GaAs and GaP will be treated.

2.2.3 Band-edge energy

Band-offsets are fundamental and important parameters in the heterostructures such as laser diodes [139]. Since Anderson had presented experimental results and theoretical consideration on the band-offsets of Ge/GaAs heterojunctions in 1962 [140],

much efforts have been made to determine the band-offsets of various heterojunctions both experimentally and theoretically.

Experimentally, the band-offsets have been measured using photoelectron spectroscopy [141,142], optical method [143,144] and electrical method [145,146]. However, there has been difficulty in determining band-offsets because reliability of the experimental data depends on the quality of the used heterojunction; it is difficult to obtain ideal structure in heterojunction rather than homojunction. Another reason for the difficulty is concerned with the interpretation of the experimental data. Even for GaAs/AlGaAs system, which is the most commonly studied heterostructure, the band-offset values were established only recently [147].

On the other hand, several theoretical models have been proposed: (1) calculation by self-consistent pseudopotential by Frensley and Kroemer [148], (2) linear combination of atomic orbitals (LCAO) theory by Harrison [128,149], (3) interface dipole model by Tersoff [150], (4) empirical method using transition-metal impurity levels by Langer and Heinrich [151] and (5) "model solid theory" by Van de Walle *et al.* [130,152–154].

Among these theories, it is well-known that Harrison's LCAO theory is relatively simple and fits experimental results rather well, except for heterojunctions with aluminum- and mercury-containing materials. Wei and Zunger pointed out that the effect of cation d orbitals, which is neglected in Harrison's theory, should be taken into account for these materials [155,156], and Sugawara presented a simple formulation including cation d orbitals [157]. However, as long as (Zn,Cd)(S,Se) materials system is treated, such effect is probably small. For these reasons, in this study, Harrison's LCAO theory was used to estimate band-lineups. In addition, deformation potentials obtained in "model solid theory" were used to treat strain effects, as will be described later.

According to the LCAO theory, band-offset is given as a difference in band-edge energy of constituent layers of heterostructure, which is calculated by tight binding method. Valence band-edge energy (E_v) and conduction-band edge energy (E_c) were calculated using following methods.

(1) For binary compounds, valence-band-edge energy ($E_{v,bin}$) was obtained by Harrison's LCAO method,

$$E_{v,bin} = \frac{E_p^c + E_p^a}{2} - \sqrt{\left(\frac{E_p^c - E_p^a}{2}\right)^2 + 4E_{xx}}, \; E_{xx} = 0.54\frac{\hbar}{md^2}, \qquad (2.2)$$

where E_p^c and E_p^a are energies of p orbital in cation (Zn, Cd) and anion (S, Se) atom, respectively, and $\hbar$, m and d are Plank's constant, electron mass and interatomic distance, respectively. Since LCAO method is not a good approximation for an empty state, i.e., conduction band, conduction-band-edge energy ($E_{c,\text{bin}}$) was determined by adding bandgap obtained experimentally to the $E_{v,\text{bin}}$.

(2) For common-anion compounds, ZnSe and CdSe, there is only small difference in E_v values. Therefore, for II-II-VI type ternary alloys, $\text{Zn}_x\text{Cd}_{1-x}\text{Se}$, $E_{v,\text{ZnCdSe}}$ was approximated by linear interpolation of E_v of binary compounds, ZnSe and CdSe;

$$E_{v,\text{ZnCdSe}} = (1-x)E_{v,\text{ZnSe}} + xE_{v,\text{CdSe}}. \tag{2.3}$$

$E_{c,\text{ZnCdSe}}$ was determined by adding bandgap to the $E_{v,\text{ZnCdSe}}$;

$$E_{c,\text{ZnCdSe}} = E_{v,\text{ZnCdSe}} + E_{g,\text{ZnCdSe}}. \tag{2.4}$$

Similar method was applied for $\text{Zn}_x\text{Cd}_{1-x}\text{S}$.

(3) For II-VI-VI type ternary alloys, $\text{ZnS}_y\text{Se}_{1-y}$ and $\text{CdS}_y\text{Se}_{1-y}$, E_c was approximated by linear interpolation of E_c of binary compounds. E_v was determined by subtracting E_g from the E_c.

(4) As for $\text{Zn}_{1-x}\text{Cd}_x\text{S}_y\text{Se}_{1-y}$ quaternary alloys, since it is expected that there is only small differences in E_c values between $\text{Zn}_{1-x}\text{Cd}_x\text{Se}$ and $\text{Zn}_{1-x}\text{Cd}_x\text{S}$ with the same cadmium composition x, E_c was linearly interpolated between those of $\text{Zn}_{1-x}\text{Cd}_x\text{Se}$ and $\text{Zn}_{1-x}\text{Cd}_x\text{S}$;

$$E_{c,\text{ZnCdSSe}} = (1-y)E_{c,\text{ZnCdSe}} + yE_{c,\text{ZnCdS}}, \tag{2.5}$$

$$E_{v,\text{ZnCdSSe}} = E_{c,\text{ZnCdSSe}} - E_{g,\text{ZnCdSSe}}. \tag{2.6}$$

The results for E_v and E_c are shown in Figs. 2.3 and 2.4. It should be noted that in these calculations strain effects on the band-edge energies are not considered. However, since the energy shift due to strain is in the order of a few tens of meV for relatively small (about 1%) mismatch, with which the layers can be used for the devices, outline of the band-lineups of heterostructures is discussed on the basis of these figures. As seen from the figures, E_v and E_c mainly depend on sulfur composition y and cadmium composition x, respectively. These are fundamental results of Harrison's LCAO theory, which is called common anion (cation) rule.

In addition, important feature can be seen from the figures. If we assume lattice-matched heterostructure, such as $\text{Zn}_{0.42}\text{Cd}_{0.58}\text{S}/\text{ZnS}_{0.06}\text{Se}_{0.94}$ on GaAs, both conduction- and valence-band-edge energies in $\text{Zn}_{0.42}\text{Cd}_{0.58}\text{S}$ are lower than those in $\text{ZnS}_{0.06}\text{Se}_{0.94}$. Therefore, it seems that so-called type-I band-lineup, which is
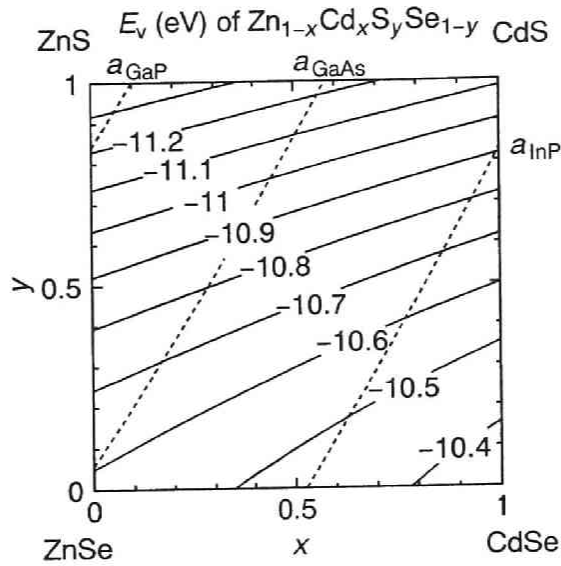
Figure 2.3: Calculated equi-valence-band-edge-energy lines for ZnCdSSe.
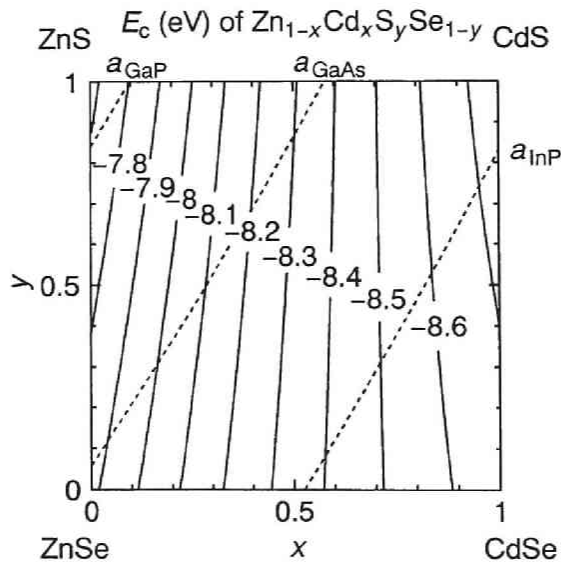
Figure 2.4: Calculated equi-conduction-band-edge-energy lines for ZnCdSSe.

necessary to confine electrons and holes in the active layer, cannot be realized by lattice-matched heterostructure on GaAs substrate, and this situation is the same for other substrates. Thus, in this material system, lattice-mismatched heterostructure should be used to fabricate double-heterostructure and quantum-well structure with type-I band-lineups.

Recently, in 1991, Okuyama *et al.* proposed ZnMgSSe quaternary system for blue LDs [71]. Using this material system, lattice-matched heterostructure having type-I band-lineup can be fabricated, which is different from ZnCdSSe quaternary system. In this point, ZnMgSSe system is suitable for blue/blue-green LDs and light-emitting diodes (LEDs). In fact, the first cw operation of blue-green LDs at room temperature has been reported in 1993 using this material system [60]. However, there seem to be the problems that magnesium readily reacts with oxygen and that MgS and MgSe have strong ionicity.

2.2.4   Refractive index

The efficiency of optical confinement in LDs is evaluated using refractive indices. For the light whose energy $\hbar\omega$ is smaller than the bandgap E_{g} ($=E_0$), the refractive index $n(\omega)$ is mainly contributed by E_0 and $E_0+\Delta_0$ gaps, and written as [158,159]

$$n(\omega)^2 = A \left\{ f(\chi) + \frac{1}{2} \left(\frac{E_0}{E_0 + \Delta_0} \right)^{\frac{3}{2}} f(\chi_{\mathrm{so}}) \right\} + B, \tag{2.7}$$

where

$$f(\chi) = \frac{2 - (1 + \chi)^{\frac{1}{2}} - (1 - \chi)^{\frac{1}{2}}}{\chi^2}, \tag{2.8}$$

$$\chi = \frac{\hbar\omega}{E_0}, \tag{2.9}$$

Table 2.5: Parameters A and B used in this work to calculate refractive indices.

Compound	A	B
ZnS	9.627	1.550
ZnSe	9.515	2.590
CdS	5.255	3.401
CdSe	9.012	3.416

$$\chi_{\text{so}} = \frac{\hbar\omega}{E_0 + \Delta_0},\tag{2.10}$$

and A, B are the fitting parameters. For binary compounds, the values of A and B have been determined by fitting Eq. (2.7) to the experimental data [160] and summarized in Table 2.2.4. For alloy layers, these parameters were interpolated from those of binary compounds, and refractive indices were calculated according to Eq. (2.7).

2.3   Design of device structures on GaAs

2.3.1   Physical parameters

As mentioned previously, blue/blue-green light-emitting devices can be fabricated on GaAs substrates. In this section, the design of such devices is presented. As discussed in the previous section, lattice-mismatched heterostructure should be used in the optical devices such as LDs and high-efficiency LEDs. When a simple DH structure or a quantum well (QW) is assumed as a structure of light-emitting device such as LD, cladding (barrier) layers should be thick enough for optical confinement, while active (well) layer is relatively thin. Therefore, the cladding layers should be lattice-matched to the substrate to avoid generation of misfit dislocations.

When GaAs is used as a substrate, among compositions for lattice-matching, either $ZnS_{0.06}Se_{0.94}$ or $Zn_{0.42}Cd_{0.58}S$ seems to be suitable for the cladding layers rather than quaternary alloys, because control of solid composition is easier for ternary alloys. In particular, the composition of $ZnS_{0.06}Se_{0.94}$ is close to that of ZnSe, whose growth techniques have been well established. Therefore, it is desirable to choose $ZnS_{0.06}Se_{0.94}$ as the cladding layer, and device structures with $ZnS_{0.06}Se_{0.94}$ cladding layers will be treated in the following argument.

On the other hand, active (well) layer must be lattice-mismatched to the cladding layers, and therefore also to the substrate for realizing type-I band lineup. In addition, the thickness of the active layer should be within critical thickness to avoid lattice relaxation, where the active layer is subjected to strain Therefore, when the device structures on GaAs substrates are discussed, it is not practical to use layers with very large lattice-mismatch, because critical thickness becomes very small for such layers. For this reason, discussion is concentrated in this section on the composition close to that of ZnSe, i.e., composition area of $0 \leq x \leq 0.3$ and $0 \leq y \leq 0.3$.

Lattice mismatch m against a substrate is defined as

$$m = \frac{(a - a_{\text{sub}})}{a_{\text{sub}}}\tag{2.11}$$
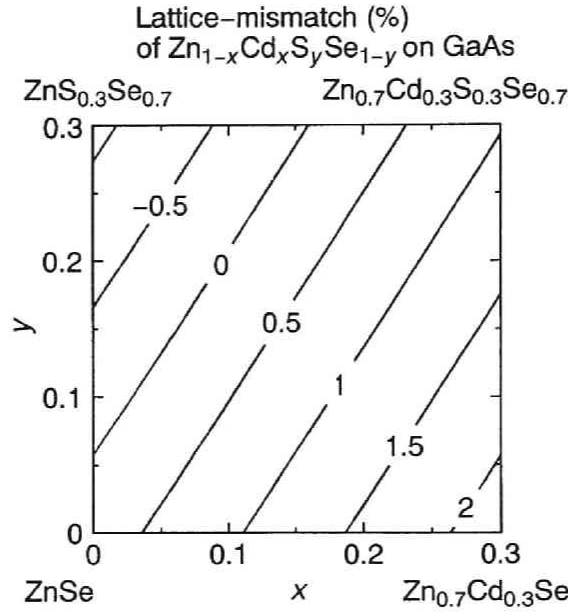
Figure 2.5: The equi-lattice-mismatch lines for the $Zn_{1-x}Cd_xS_ySe_{1-y}$ in the composition area of $0{\leq}x{\leq}0.3$ and $0{\leq}y{\leq}0.3$.

where a_{sub} is lattice constant of the substrate. Figure 2.5 shows lattice mismatch of $Zn_{1-x}Cd_xS_ySe_{1-y}$ to GaAs. Several models to calculate the critical thickness (t_c) as a function of lattice mismatch have been proposed to date. Matthews and Blakeslee [161] and People and Bean [162] proposed the theories for the estimation of critical thickness, t_c. Among zinc blende II-VI compounds, t_c of ZnSe grown on GaAs (lattice-mismatch of 0.26%) has been investigated experimentally by several groups, and reported to be about 1500 Å [163]. On the other hand, results of theoretical calculation are t_c=520 Å by Matthews and Blakeslee's model (MB model) [161] and t_c=2.3 μm by People and Bean's model (PB model) [162]. Therefore, for ZnSe or other II-VI materials, the actual critical thickness is probably between the values predicted by the above two models.

For example, if the ZnSe layer has lattice-mismatch of 1 %, it is estimated that t_c is between 97 Å (according to MB model) and 1000 Å (PB model); these values do not vary with composition sensitively. At present, these theories should be used as a guideline in designing and fabricating the device structures using the (Zn,Cd)(S,Se) system, because there are few experimental results of critical thickness for these materials. By characterization of the structure thus fabricated, *e.g.*, systematic

study of the optical and crystallographic quality of QWs with the same composition and different thickness, the theory of critical thickness should be amended.

In the calculation of band-lineups of the heterostructures including such strained layers, strain effects should be taken into account For the quaternary epitaxial layer coherently grown on (100)-oriented substrate, strain tensors ε_{ij} are given by

$$\varepsilon_{yy} = \varepsilon_{zz} = \varepsilon = \frac{(a_{\text{sub}} - a_{\text{bulk}})}{a_{\text{bulk}}}, \tag{2.12}$$

$$\varepsilon_{xx} = -2\left(\frac{C_{12}}{C_{11}}\right)\varepsilon, \tag{2.13}$$

$$\varepsilon_{xy} = \varepsilon_{yz} = \varepsilon_{zx} = 0, \tag{2.14}$$

where a_{sub} and a_{bulk} are the lattice constants of the substrate and the epitaxial layer without strain, respectively, C_{11} and C_{12} the elastic stiffness constants of the quaternary alloy, which were derived from those of binary compounds by composition-weighted averaging.

Conduction- and valence-band-edges of the ZnCdSSe epitaxial layers under strain are given by [130]

$$E_{\text{c,strain}} = E_{\text{c,0}} + E_{\text{hc}}, \tag{2.15}$$

$$E_{\text{v,hh,strain}} = E_{\text{v,0}} + E_{\text{hv}} - E_{\text{s}}, \tag{2.16}$$

$$\begin{aligned} E_{\text{v,lh,strain}} &= E_{\text{v,0}} + E_{\text{hv}} + \frac{1}{2}\Delta_0 + \frac{1}{2}E_{\text{s}} \\ &\quad + \frac{1}{2}\left(\Delta_0^2 + 2\Delta_0 E_{\text{s}} + 9E_{\text{s}}^2\right)^{\frac{1}{2}}, \end{aligned} \tag{2.17}$$

$$\begin{aligned} E_{\text{v,so,strain}} &= E_{\text{v,0}} + E_{\text{hv}} - \frac{1}{2}\Delta_0 + \frac{1}{2}E_{\text{s}} \\ &\quad - \frac{1}{2}\left(\Delta_0^2 + 2\Delta_0 E_{\text{s}} + 9E_{\text{s}}^2\right)^{\frac{1}{2}}, \end{aligned} \tag{2.18}$$

where

$$E_{\text{hc}} = a_{\text{c}}(\varepsilon_{xx} + \varepsilon_{yy} + \varepsilon_{zz}) = 2a_{\text{c}}\left\{1 - \left(\frac{C_{12}}{C_{11}}\right)\right\}\varepsilon, \tag{2.19}$$

$$E_{\text{hv}} = a_{\text{v}}(\varepsilon_{xx} + \varepsilon_{yy} + \varepsilon_{zz}) = 2a_{\text{v}}\left\{1 - \left(\frac{C_{12}}{C_{11}}\right)\right\}\varepsilon, \tag{2.20}$$

$$E_s = b\left(\varepsilon_{xx} - \varepsilon_{yy}\right) = -b\left\{1 + 2\left(\frac{C_{12}}{C_{11}}\right)\right\}\varepsilon, \tag{2.21}$$

and $E_{c,0}$ and $E_{v,0}$ are the conduction and valence band edge energies without strain, respectively, and subscripts hh, lh and so denote heavy hole, light hole and spin-orbit split off bands, respectively. Δ_0 is spin-orbit splitting energy. The parameters a_c and a_v are the hydrostatic deformation potentials for conduction and valence bands, respectively, and b is the shear deformation potential.

Deformation potentials for ZnSSe were linearly interpolated from those for ZnSe and ZnS. Since the deformation potentials for cubic CdS or CdSe are not available, deformation potentials for $Zn_{1-x}Cd_xS_ySe_{1-y}$ were substituted by those for ZnS_ySe_{1-y} with the same sulfur composition y. This substitution may cause discrepancy if cadmium composition in the alloy is high. However, as far as the cadmium composition x is less than 0.3 and thus the strain also is less than a few percent, the error is roughly estimated to be less than about 10 meV. Since the values of deformation potentials for ZnS and ZnSe themselves are not well established experimentally so far, the results obtained here should be taken as a guideline for the present purpose.

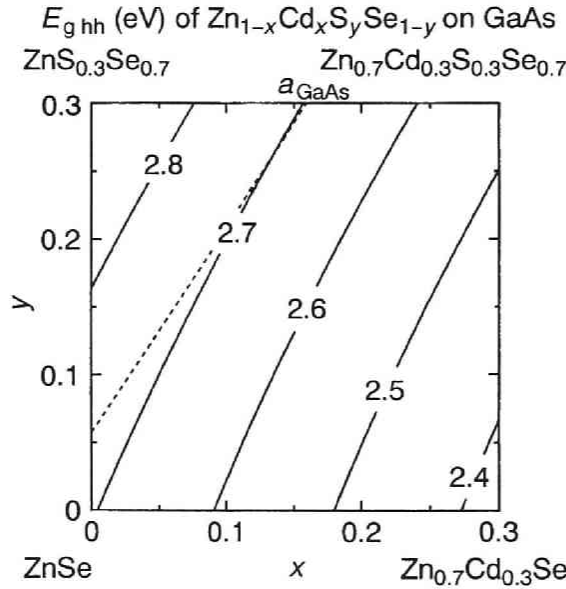
Figure 2.6: The equi-bandgap lines at RT for $Zn_{1-x}Cd_xS_ySe_{1-y}$ coherently grown on GaAs. Strain effects are taken into account.
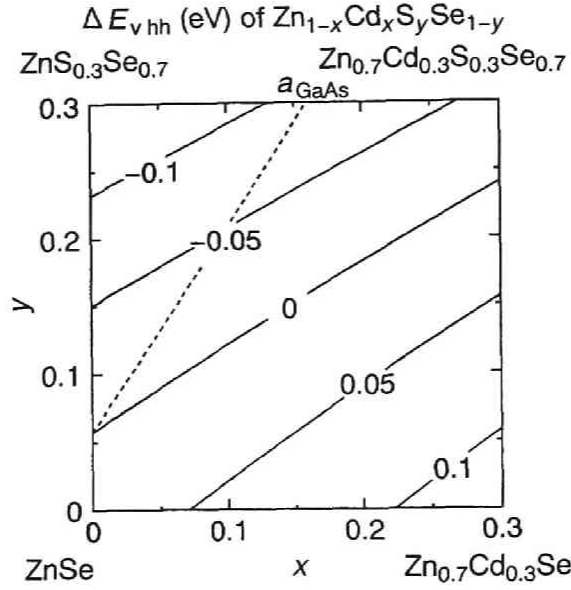
Figure 2.7:   The equi-valence-band-offset lines for $Zn_{1-x}Cd_xS_ySe_{1-y}$ against $ZnS_{0.06}Se_{0.94}$ lattice-matched to GaAs substrate.
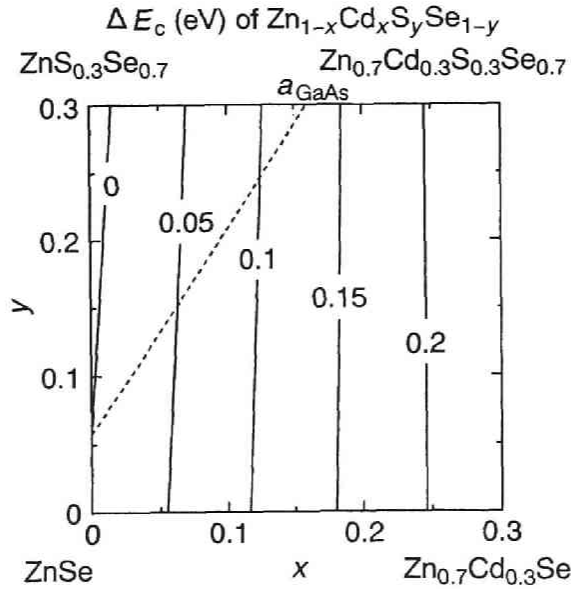

Figure 2.8:   The equi-conduction-band-offset lines for $Zn_{1-x}Cd_xS_ySe_{1-y}$ against $ZnS_{0.06}Se_{0.94}$.

Under the condition that cladding layers should be lattice-matched to the substrate, as described previously, it is thought to be necessary to use well layers with lager lattice constant than the cladding layers in order to realize so-called type-I band lineups, in which the well layers act as potential wells for both electrons and holes. Therefore, the well layers suffer from biaxial compressive strain, which results in the split of the valence band into heavy and light hole bands, and the heavy hole band at $k=0$ becomes the top of the valence band. Thus, the heavy hole band is emphasized in the following arguments. Here, bandgap under strain is given by

$$E_{\text{g,strain}} = E_{\text{c,strain}} - E_{\text{v,hh,strain}}, \tag{2.22}$$

and equi-bandgap lines thus calculated for pseudomorphic ZnCdSSe alloys grown on GaAs are shown in Fig. 2.6. As mentioned previously, it is assumed that $ZnS_{0.06}Se_{0.94}$, which is lattice-matched to GaAs, is used as a cladding layer. Therefore, valence- and conduction-band-offsets between cladding and active layers are given by

$$\Delta E_{\text{v}} = E_{\text{v,hh,strain}} - E_{\text{v,ZnSSe}}, \tag{2.23}$$

$$\Delta E_{\text{c}} = E_{\text{c,ZnSSe}} - E_{\text{c,strain}}, \tag{2.24}$$

where $E_{\text{v,ZnSSe}}$ and $E_{\text{c,ZnSSe}}$ refer to valence and conduction band edge energies of $ZnS_{0.06}Se_{0.94}$, respectively. It is should be noted that the sign of ΔE_{v} and ΔE_{c} are defined to be positive when a ZnCdSSe layer acts as a potential well in the Eqs. (2.23) and (2.24). For carrier confinement, therefore, both ΔE_{c} and ΔE_{v} should be positive. Figures 2.7 and 2.8 show calculated results for band-offsets of the pseudomorphic $Zn_{1-x}Cd_xS_ySe_{1-y}$ relative to $ZnS_{0.06}Se_{0.94}$ for valence and conduction bands, respectively.

2.3.2 Device structures

In designing light-emitting devices, there seem to be two fundamental requirements; (1) all the constituent layers must be grown coherently to substrates, (2) both conduction- and valence-band-offsets should be large enough to confine both electrons and holes into the active layer. $Zn_{1-x}Cd_xSe$-$ZnS_{0.06}Se_{0.94}$ heterostructure system, which was proposed first by Wu *et al.* [164], seems to satisfy these requirements. Since ZnSSe cladding layers are lattice-matched to GaAs, whole structure can be grown coherently by adjusting composition and thickness of the $Zn_{1-x}Cd_xSe$ well layer. In such QWs, type-I band-lineup will be realized as seen from Figs. 2.7 and 2.8. An example of calculated band-lineup for ZnCdSe-ZnSSe QWs is shown in

$ZnS_{0.06}Se_{0.94}(n{=}2.720)$
$Zn_{0.80}Cd_{0.20}Se\ (n{=}3.086)$
$ZnS_{0.06}Se_{0.94}$

$\Delta E_c{=}165$ meV

$\Delta a/a{=}1.61$ %

$E_g{=}2.478$ eV
$(500$ nm$)$

$\Delta E_{v\ hh}{=}92$ meV
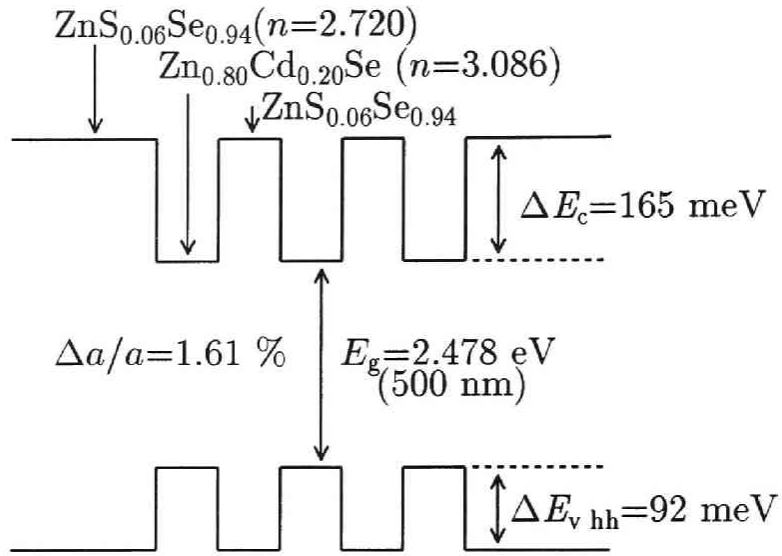
Figure 2.9: Calculated band-lineup for ZnCdSe-ZnSSe MQW on GaAs at RT.

$ZnS_{0.06}Se_{0.94}\ (n{=}2.720)$
$Zn_{0.80}Cd_{0.20}Se\ (n{=}3.086)$
$Zn_{0.95}Cd_{0.05}S_{0.03}Se_{0.97}\ (n{=}2.771)$

121 meV

165 meV

$E_g{=}2.478$ eV
$(500$ nm$)$

63 meV

92 meV
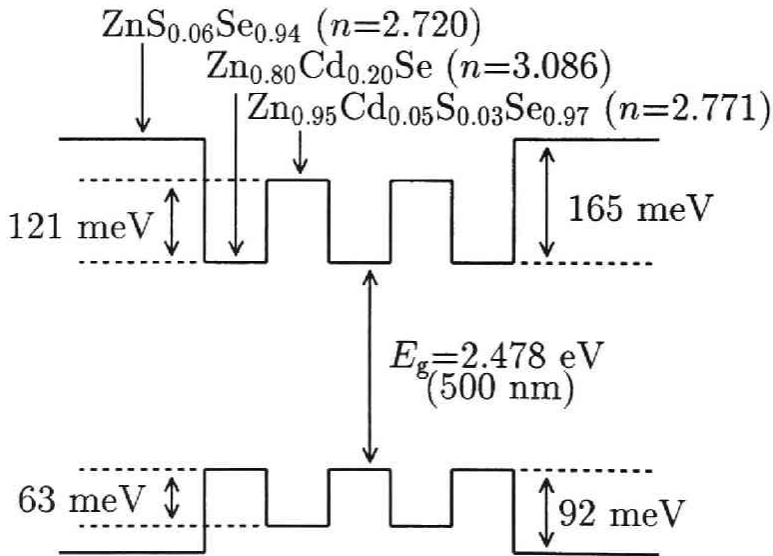
Figure 2.10: Example of calculated band-lineup at RT for modified MQW laser structure using ZnCdSSe quaternary system.

$$ZnS_{0.06}Se_{0.94}(n=2.720)$$
$$Zn_{1-x}Cd_xS_ySe_{1-y}$$
$$Zn_{0.80}Cd_{0.20}Se \ (n=3.086)$$

$$\Delta E_c = 165 \ \text{meV}$$

$$E_g = 2.478 \ \text{eV}$$
$$(500 \ \text{nm})$$

$$\Delta E_{v \ hh} = 92 \ \text{meV}$$
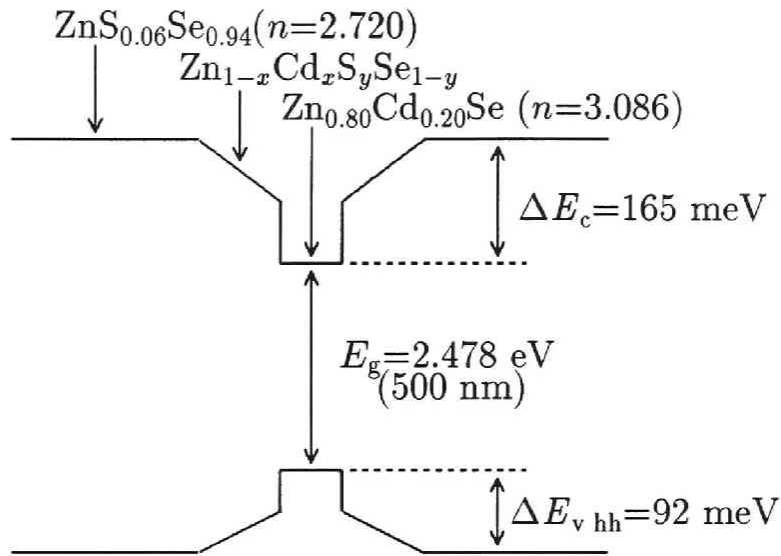
Figure 2.11: Example of calculated band-lineup for GRIN-SCH laser structure using ZnCdSSe quaternary system.

Fig. 2.9. Kawakami *et al.* have reported the first operation of optically pumped laser consist of this type of multiple quantum wells (MQWs) in 1991 [55]; the threshold excitation intensity was the lowest and the operating temperature was the highest in optically pumped lasers emitting blue-green light at that time. Furthermore, high performance of LDs [165] or LEDs [61] using this material system has been reported also by other groups later. These facts suggest high potential of this system for blue/blue-green light-emitting devices.

For further improvement in performance of blue/blue-green LDs and LEDs toward practical use, the structure have to be optimized precisely under severe restriction that the strain in the wells should be suppressed not to generate misfit dislocations. For this purpose, it is desirable to increase flexibility in designing by introducing ZnCdSSe quaternary alloy.

For example, if we assume a simple DH structure emitting light of certain wavelength, composition of the well is fixed when $Zn_{1-x}Cd_xSe$ is used, while using $Zn_{1-x}Cd_xS_ySe_{1-y}$, we can choose appropriate values of x and y, and therefore band-offset ratio $\Delta E_c : \Delta E_v$. In addition, by using ZnCdSSe quaternary alloy whose composition is between ZnSSe and ZnCdSe, it becomes possible to utilize a modified MQW [166] or a graded index separate confinement heterostructure QW (GRIN-SCH-QW) [167] which are effective for the improvement of LDs as has been

performed in III-V semiconductors. Examples of calculated band-lineups for these structures are shown in Figs. 2.10 and 2.11.

2.4   Design of device structures on GaP

2.4.1   Physical parameters

In this section, discussions will be concentrated on the pseudomorphic structures on GaP. Quaternary alloys lattice-matched to GaP possess alloy compositions between $ZnS_{0.84}Se_{0.16}$ and $Zn_{0.90}Cd_{0.10}S$, as shown in Fig. 2.1. Since the materials not highly lattice-mismatched to these quaternary alloys are of interest in a practical device structure, special emphasis is given on the physical parameters of the quaternary alloy, $Zn_{1-x}Cd_xS_ySe_{1-y}$ in the composition range of $0 \leq x \leq 0.3$ and $0.7 \leq y \leq 1$.

The procedure to calculate physical parameters is basically the same as in the case for GaAs substrates. Lattice mismatch of a $Zn_{1-x}Cd_xS_ySe_{1-y}$ alloy to a GaP substrate is shown in Fig. 2.12. As mentioned previously and also seen from Fig. 2.12, two kinds of ternary alloys, i.e., $ZnS_{0.84}Se_{0.16}$ and $Zn_{0.90}Cd_{0.10}S$ can be lattice-matched to GaP. These ternary alloys seem to be suitable for the cladding layers.
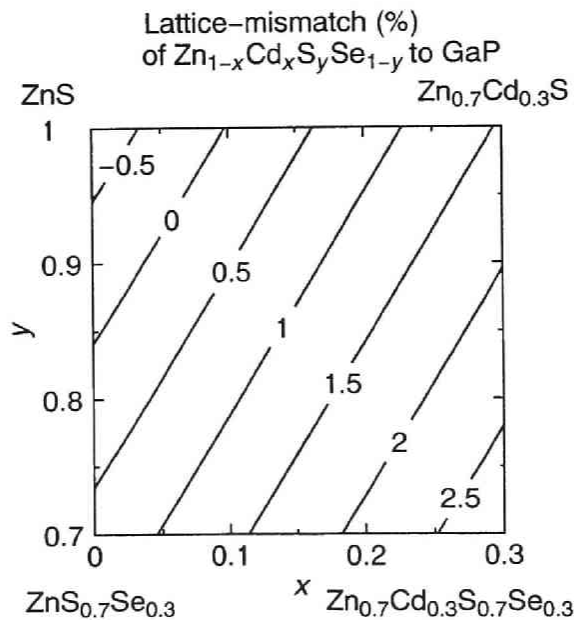
Figure 2.12: Lattice mismatch of $Zn_{1-x}Cd_xS_ySe_{1-y}$ to GaP substrate.

$E_{g\,hh}$ (eV) of $Zn_{1-x}Cd_xS_ySe_{1-y}$ on GaP
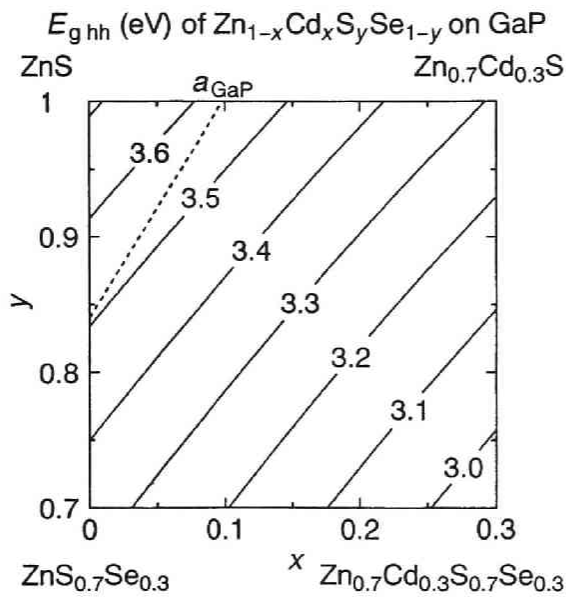
Figure 2.13: Bandgap of $Zn_{1-x}Cd_xS_ySe_{1-y}$ grown coherently onto GaP substrate at RT.

$\Delta E_{v\,hh}$ (eV) of $Zn_{1-x}Cd_xS_ySe_{1-y}$
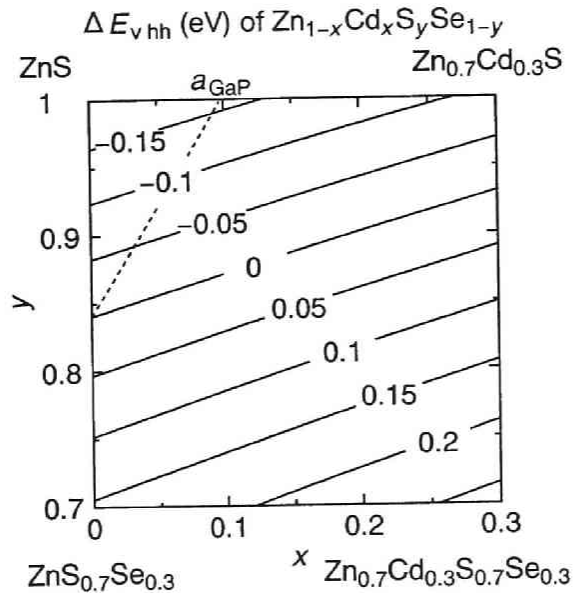
Figure 2.14: Valence-band-offset in $Zn_{1-x}Cd_xS_ySe_{1-y}/ZnS_{0.84}Se_{0.16}$ heterostructure grown coherently on GaP substrate.

ΔE_c (eV) of $Zn_{1-x}Cd_xS_ySe_{1-y}$

ZnS a_{GaP} $Zn_{0.7}Cd_{0.3}S$

1

0

0.05

0.9   0.1

0.15

0.2

0.25

0.8   0.3

0.7
0   0.1   0.2   0.3

$ZnS_{0.7}Se_{0.3}$ x $Zn_{0.7}Cd_{0.3}S_{0.7}Se_{0.3}$
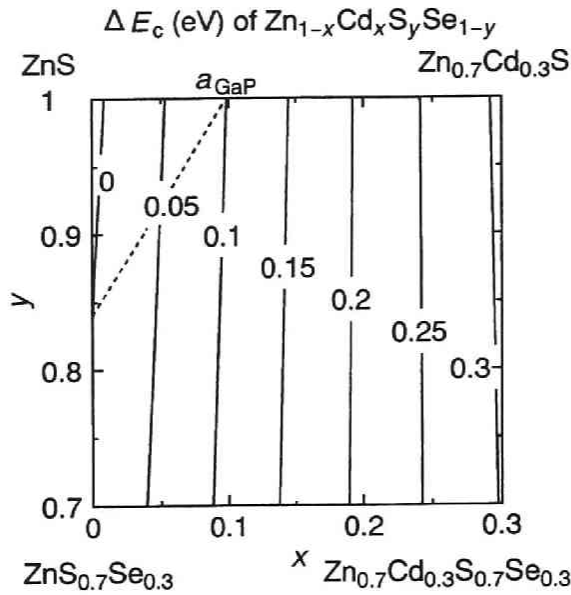
Figure 2.15: Conduction-band-offset in $Zn_{1-x}Cd_xS_ySe_{1-y}/ZnS_{0.84}Se_{0.16}$ heterostructure grown coherently on GaP substrate.

Here, calculated results are shown for the structure where $ZnS_{0.84}Se_{0.16}$ is used as a cladding layer. Similar calculations can be conducted for those with a $Zn_{0.90}Cd_{0.10}S$ cladding layer. Equi-bandgap lines calculated for pseudomorphic ZnCdSSe alloys grown on GaP are shown in Fig. 2.13. Band-offsets of the pseudomorphic ZnCdSSe for valence and conduction bands relative to $ZnS_{0.84}Se_{0.16}$ are shown in Figs. 2.14 and 2.15. As seen from Fig. 2.13, the bandgap is much larger than that for the case of GaAs substrate shown in Fig. 2.6, as a result of increased sulfur composition. As for band-offsets, the fundamental feature is similar to the case on GaAs substrate. However, the spacing of the lines in Figs. 2.14 and 2.15 is smaller than that in Figs. 2.7 and 2.8, while the spacings of the equi-lattice-mismatch lines in Figs. 2.12 and 2.5 are similar. This means larger band offsets can be obtained in the structure on GaP than in those on GaAs for the same lattice-mismatch values, which is due to bowing effect of bandgap.

2.4.2 Device structures

An example of a calculated band-lineup of the ZnCdSSe/ZnSSe heterostructure on GaP substrates is shown in Fig. 2.16. The well layer possesses lattice-mismatch

$ZnS_{0.84}Se_{0.16}(n{=}2.685)$
  ↓ $Zn_{0.85}Cd_{0.15}S_{0.80}Se_{0.20}$ $(n{=}3.018)$

$\Delta E_c{=}160$ meV

$\Delta a/a{=}1.33$ % $E_g{=}3.246$ eV
                          (382 nm)

$\Delta E_{v\,hh}{=}102$ meV
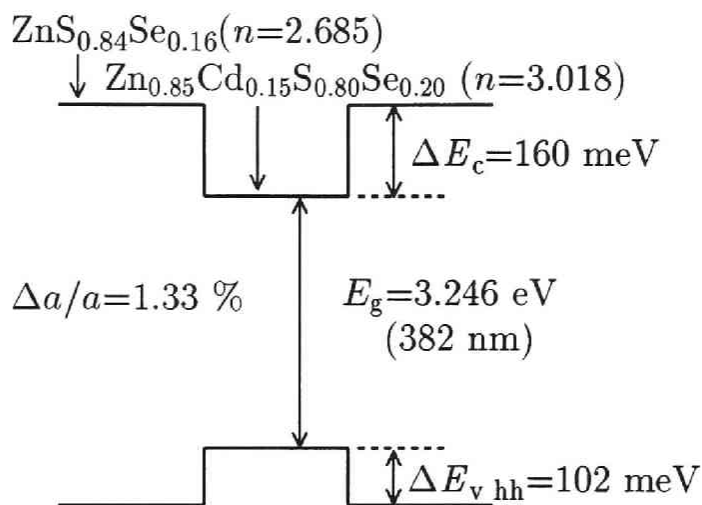
Figure 2.16: Example of calculated band-lineup of the ZnCdSSe/ZnSSe heterostructure on GaP substrates at RT.

$Zn_{0.90}Cd_{0.10}S$ $(n{=}2.660)$
  ↓ $Zn_{0.75}Cd_{0.25}S_{0.96}Se_{0.04}$ $(n{=}2.989)$

$\Delta E_c{=}159$ meV

$\Delta a/a{=}1.36$ % $E_g{=}3.304$ eV
                          (375 nm)

$\Delta E_{v\,hh}{=}107$ meV
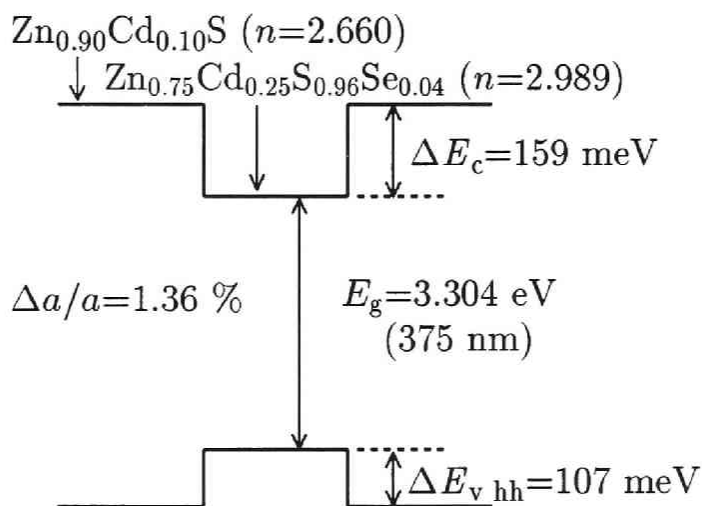
Figure 2.17: Example of calculated band-lineup of the ZnCdSSe/ZnCdS heterostructure on GaP substrates.

of 1.33%, which gives the calculated critical thickness (t_c) of 66 Å (according to MB model) and 490 Å (PB model). The bandgap of the well at RT is 3.246 eV , corresponding to the near-UV spectral region. The heterostructures have fairly large band-offsets compared with thermal energy at RT, reflecting the differences in compositions of both anion and cation between the well and the barrier layers; this is realized by using ZnCdSSe. If larger conduction or valence band-offset is needed, it would be possible to construct such a structure by changing cation or anion composition of the ZnCdSSe well layer, respectively, although the lattice mismatch obviously increases. It should be noted that ZnCdSSe quaternary well layers must be included in such structures as have large band-offsets for valence and conduction bands.

In addition to the structure where $ZnS_{0.84}Se_{0.16}$ ternary alloys are used as cladding layers, it is possible to construct a structure where $Zn_{0.90}Cd_{0.10}S$ ternary alloys are used as cladding layers. Figure 2.17 shows an example of the calculated band lineup for the system using the ZnCdS cladding layers. The values are similar to those in Fig. 2.16, because the solid compositions of the constituent layers in both structures are essentially close to that of ZnS. A key factor in determining which structure is

Figure 2.18: Effective bandgap and band-offsets of $Zn_{0.85}Cd_{0.15}S_{0.84}Se_{0.16}$-$ZnS_{0.84}Se_{0.16}$ SQW at RT.

Chapter 3

ZnSe-based structures with ZnCdSSe quaternary alloys on GaAs substrates

3.1   Introduction

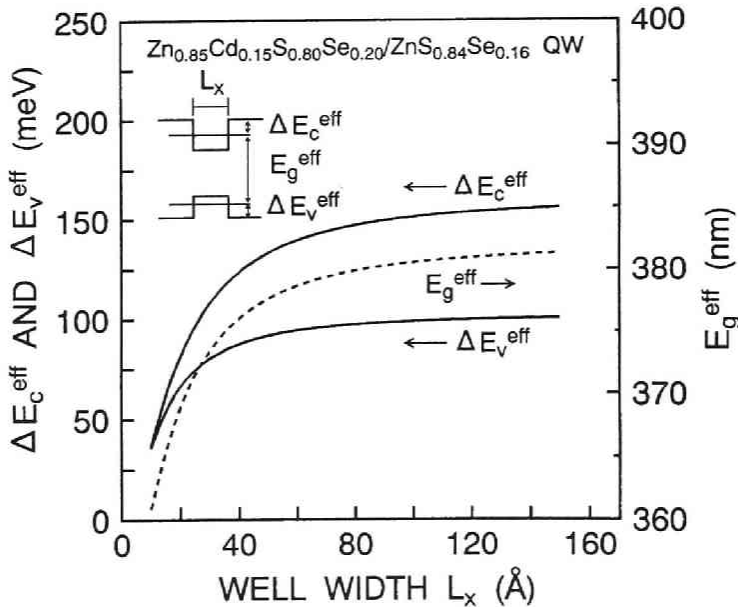ZnSe has long been studied as a material for blue-light-emitting devices, and recently the development of ZnSe-based heterostructure as well as the success in p-type conduction control by molecular beam epitaxy (MBE) lead to ZnSe-based blue-green laser diodes (LDs) and light-emitting diodes (LEDs), as mentioned in Chapter 1. For more flexible design of the devices with the ZnSe-based system, the use of ZnCdSSe quaternary alloys is proposed in this study.

For the epitaxial growth of ZnSe and ZnSe-based heterostructure, metalorganic vapor phase epitaxy (MOVPE) and MBE are considered to be suitable techniques. Both techniques enable us to reduce extrinsic impurity and intrinsic defects in ZnSe-based crystals owing to low growth temperature. One of the advantages of MOVPE technique is good controllability of growth rate and composition especially in the alloy growth, as a result of mass flow control of gaseous sources. On the other hand, MBE technique is suitable for the growth of heterostructure with uniform thickness and abrupt interfaces, and enables one to monitor surface structure *in situ* by reflection high-energy electron diffraction (RHEED).

Gas-source MBE (GSMBE) or metalorganic MBE (MOMBE) is a kind of MBE technique where all or a part of the sources are gaseous ones [169–171]. In general, such MBE-based techniques as use metalorganics in part are called MOMBE. These techniques have advantages of both MOVPE and MBE mentioned above, i.e., good controllability of composition and structure especially in the growth of alloys containing elements having high vapor pressure. Therefore, it is suitable for the growth of multi-layered structures with alloys, such as light-emitting devices with multiple quantum wells (MQWs). In particular, this technique seems to be

suitable for the growth of II-VI materials because both group-II and -VI elements have high vapor pressure. For ZnSe, several authors have reported the GSMBE growth [45, 172–175]. In addition, successful growth of ZnSe/ ZnSSe [176] and ZnCdSe/ZnSSe [164] short period strained layer superlattices have been reported. Furthermore, optically pumped blue-green laser using ZnCdSe/ZnSSe MQWs which showed the lowest threshold excitation intensity was fabricated by MOMBE technique [55]. On the basis of these background, MOMBE technique seems to be one of the most suitable technique for the growth of ZnSe-based structures with ZnCdSSe.

In this Chapter, MOMBE growth and characterization of ZnCdSSe quaternary alloys on GaAs substrates are described [177]. Since the growth condition of ZnSe or ZnSSe by using the present system is well-established, ZnCdSSe was grown by perturbing the condition from that for ZnSe or ZnSSe. As applications of ZnCdSSe, fabrication of optically pumped laser is also described [96].

3.2   Growth systems and techniques

The epitaxial growth for films described in this chapter was carried out using a MOMBE system (ANELVA KMV-101) which was designed especially for gas source applications. The MOMBE system is schematically illustrated in Fig. 3.1. It is equipped with RHEED and dynamic RHEED monitorring system, with which
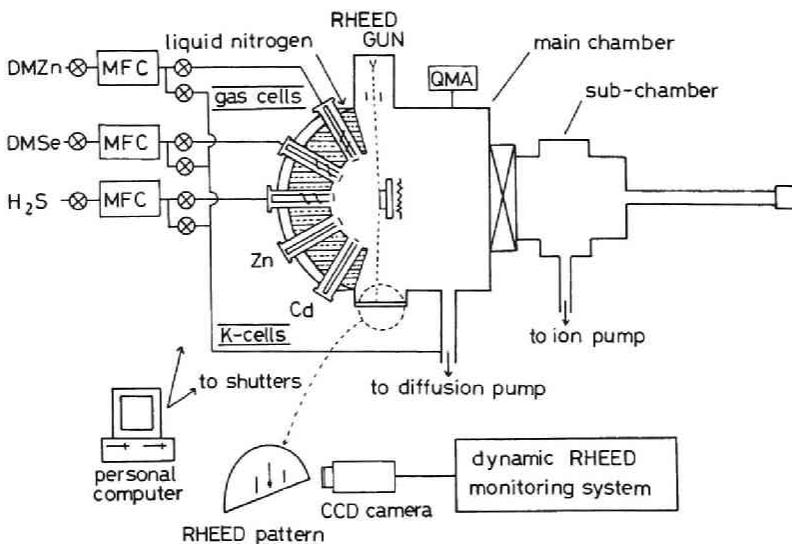

Figure 3.1: Schematic illustration of the MOMBE system.

Table 3.1: Typical growth condition of ZnCdSSe.

Substrate Temperature	280 °C
DMZ flow rate	22.4 μmol/min
DMSe flow rate	53.7 μmol/min
H_2S flow rate	0–81 μmol/min
Cd cell temperature	180–200 °C
(Cd flux)	(order of 10^{14} atoms/(cm^2·s))

RHEED pattern and intensity can be monitorred. The background pressure of the system is about 1×10^{-9} Torr and the working pressure during the growth is of the order of 10^{-5} Torr. Dimethylzinc (DMZn), hydrogen sulfide (H_2S) and dimethylselenide (DMSe) were used as gas-source materials for zinc, sulfur and selenium, respectively. Since metalorganic zinc source was used, the growth technique used in this chapter is called MOMBE, and is distinguished from that used in the next chapter, which is called GSMBE. The DMZn, H_2S and DMSe gas flows were controlled by mass flow controllers, and before the introduction of these source gases into the growth chamber, they were decomposed with tantalum crackers at 950, 1080 and 850 °C, respectively. For a cadmium source, metallic cadmium was used in order to avoid the excess generation of hydrocarbon, which causes a rise in background pressure and impedes the MBE growth mode. The flux intensity of cadmium was controlled using a conventional Knudsen cell. The (100)-oriented GaAs substrates were pretreated by degreasing, etching in H_2SO_4:H_2O_2:H_2O=5:1:1 solution and then dipping into a $(NH_4)_2S_x$ solution for a few minutes [178]. Prior to the growth, the substrates were preheated to 420 °C in the chamber to desorb the excess sulfur. This procedure has been reported to be very effective for the two-dimensional nucleation of ZnSe [179], ZnSSe [176] and ZnCdSe [164] from an early stage of growth. At first, ZnSe buffer layers were coherently grown with a thickness of several hundred Å at a substrate temperature (T_{sub}) of 280 °C, which has been established as the optimum temperature for the growth of ZnSe, using our MOMBE system [176,179]. As a first step, ZnCdSSe quaternary alloy layers with small cadmium and sulfur composition were grown on ZnSe buffers at T_{sub}=280 °C with constant flow rate of zinc and selenium sources, while varying the supply of cadmium and sulfur sources. Typical growth conditions are summarized in Table 3.1.

3.3   Growth and characterization of ZnCdSSe quaternary alloys

The dependence of lattice parameter normal to the surface plane $(a_\perp)$ and photoluminescence (PL) peak energy at 4.2 K (E_{PL}) of $Zn_{1-x}Cd_xS_ySe_{1-y}$ on the amount of source supply was investigated. Flow rates of DMZn and DMSe were kept constant, while the cadmium cell temperature and flow rate of H_2S were changed. For PL measurements, a He-Cd laser (325 nm) was used as an excitation source. Excitation power density was 500 mW/cm^2. Figures 3.2 and 3.3 show the results, where dependence on flow rate of H_2S are shown using cadmium cell temperature as a parameter. The lattice parameter was measured by X-ray diffraction. Since $Zn_{1-x}Cd_xS_ySe_{1-y}$ alloys whose data are shown in Fig. 3.2 and 3.3 are thin (500–3000 Å) and have small lattice-mismatch to GaAs (less than 1 %), they are probably pseudomorphic. (Note that the difference between $a_\perp$ and a_{GaAs} becomes large if the $Zn_{1-x}Cd_xS_ySe_{1-y}$ is pseudomorphic.) In fact, lattice parameter of the $Zn_{1-x}Cd_xS_ySe_{1-y}$ layers parallel to the surface plane was almost the same as that of GaAs, which was confirmed by (400) and (511) X-ray diffraction measurement. PL peak is probably due to the radiative recombination of free excitons or excitons bound to shallow impurities, although the origin has not been identified yet. It is seen from the figures that both lattice parameter and E_{PL} vary steadily with changing H_2S flow rate. Therefore, it seems that composition of $Zn_{1-x}Cd_xS_ySe_{1-y}$ can be controlled by changing source supply.

The composition of several quaternary alloys were evaluated by the analysis of the intensity ratio of Auger signals for each atom, while composition of the ternary layer was evaluated from lattice parameter measured by X-ray diffraction. For each composition thus determined, experimental values of $a_\perp$ and E_{PL} were compared with the calculated values of $a_\perp$ and heavy-hole bandgap under strain $(E_{g\,hh})$, respectively. In Figs. 3.4 and 3.5, the composition of the quaternary alloys are plotted with the experimental values, and calculated contours of $a_\perp$ and $E_{g\,hh}$ are also drawn, respectively. For $a_\perp$, the experimental and calculated values agree very well for small sulfur composition area $(y \leq 0.1)$, while the experimental values are somewhat larger than the calculated values. This discrepancy can be explained if it is assumed that sulfur composition was overestimated. As for E_{PL}, it should be noted that two ZnCdSe layers are not pseudomorphic but nearly free-standing owing to relatively large lattice-mismatch of 0.8 and 1.5 % and thickness of more than 1 μm, while the ZnCdSSe and ZnSSe layers are pseudomorphic. If it is assumed that the origin of the emission is the excitons bound to shallow impurity, the difference between the
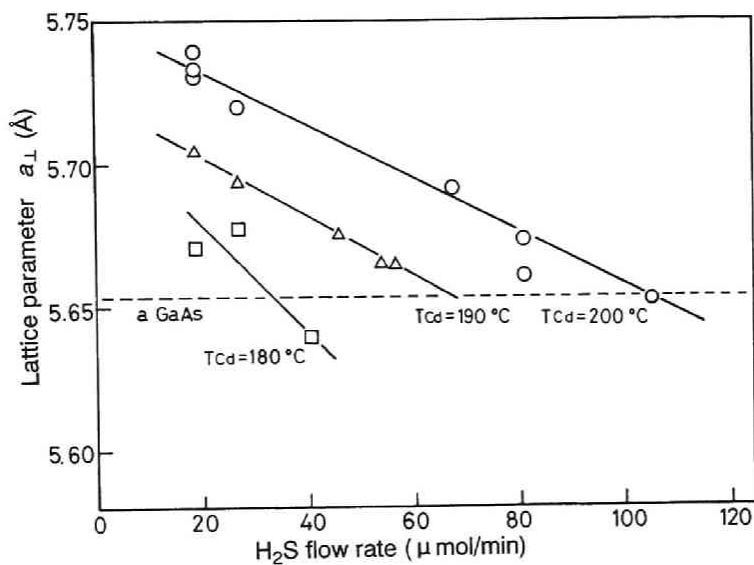
Figure 3.2: Dependence of lattice parameter $a_\perp$ on H_2S flow rate, using cadmium cell temperature as a parameter.
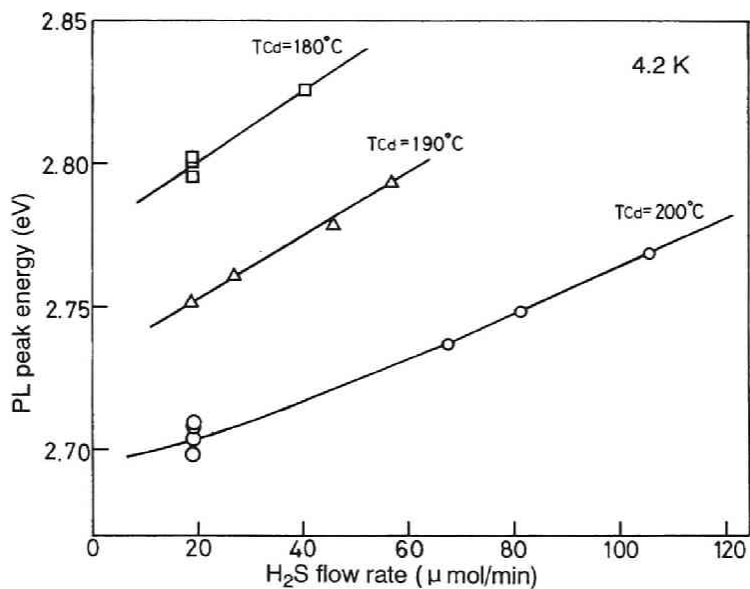
Figure 3.3: Dependence of 4.2 K PL peak energy on H_2S flow rate, using cadmium cell temperature as a parameter.
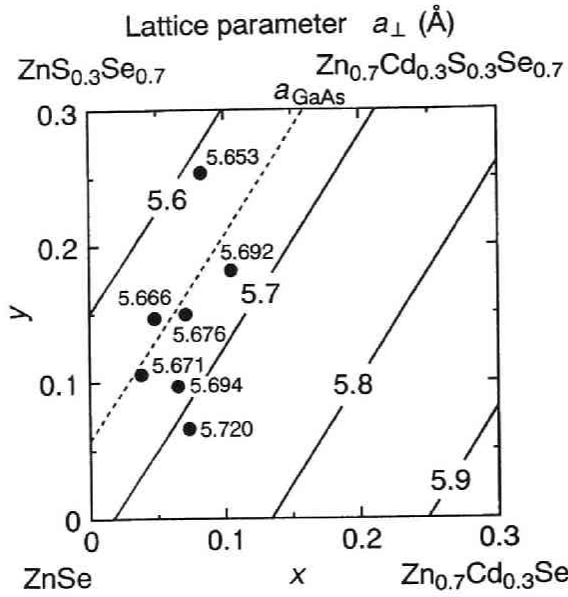
Figure 3.4: Measured and calculated lattice parameter $a_\perp$. Composition of $Zn_{1-x}Cd_xS_ySe_{1-y}$ samples are indicated by closed circles, and measured $a_\perp$ values are written beside the circles. Solid lines are calculated contours of $a_\perp$.
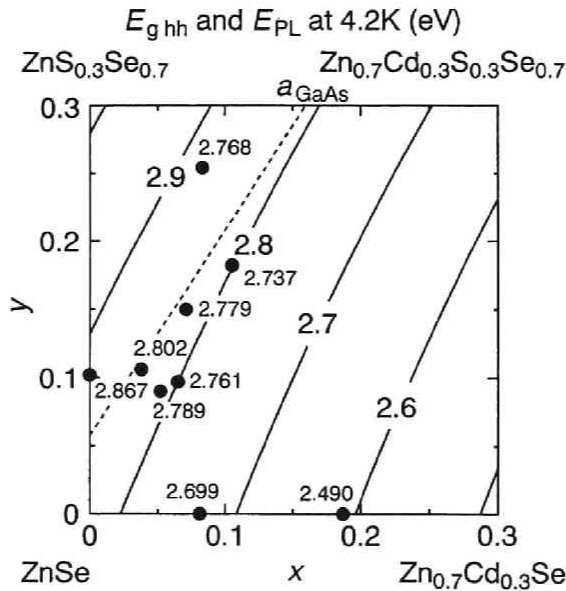
Figure 3.5: PL peak energy at 4.2 K (E_{PL}) and calculated contours of heavy-hole bandgap ($E_{g\,hh}$). Closed circles indicate composition, and numbers are observed E_{PL}.

bandgap and the peak energy is the sum of binding energy of free exciton (E_{bin}^{FE}=19 meV in ZnSe [107]) and localization energy to the impurity (several meV). As seen in Fig. 3.5, the discrepancy between calculated bandgap and observed E_{PL} becomes larger as the sulfur composition increases. This can also be explained qualitatively if overestimation of sulfur composition is assumed. Note that for $ZnS_{0.10}Se_{0.90}$, whose composition was determined by X-ray diffraction, energy of heavy-hole free exciton emission (2.867 eV) agrees very well with expected value of 2.863 eV ($=E_{g\,hh}$ (2.882 eV) $-E_{bin}^{FE}$ (19 meV)). Also note that for $Zn_x Cd_{1-x}Se$ (x=0.08, 0.19) expected bandgaps are 15 and 27 meV smaller than the values of pseudomorphic layers since lattice strain is relaxed. Anyway, it is difficult to discuss relationship between E_{ghh} and E_{PL} quantitatively because the origin of PL for each composition has not been identified yet. However, we may conclude that experimental and calculated values agree qualitatively for lattice parameters and bandgap. It is also pointed out that sulfur composition may be overestimated by Auger analysis.

Figure 3.6 shows the variation of cadmium and sulfur composition as a function of H_2S flow rate using cadmium cell temperature as a parameter, under constant
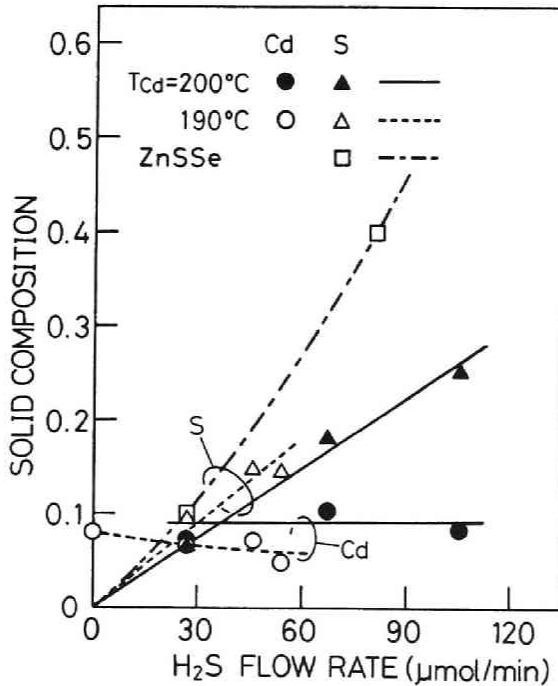
Figure 3.6: The variation of alloy compositions of Cd and S as a function of H_2S flow rate under a constant supply of Cd flux.

flow rates of DMZn and DMSe, 22.4 and 53.7 μmol/min, respectively. It was found that sulfur composition increases with increasing H_2S flow rate, while cadmium composition is kept at an almost constant value depending on the cadmium flux. It was also found that for the same flow rate of H_2S sulfur composition of ZnCdSSe is smaller than that of ZnSSe. Therefore, sulfur composition seems to decrease as cadmium flux increases. Since the sulfur composition of ZnCdSSe is probably overestimated by Auger analysis as mentioned above, i.e., actual sulfur composition of ZnCdSSe seems to be smaller, the reduction of sulfur composition by cadmium flux may be larger than shown in Fig. 3.6. This effect is probably related to the differences in bond strength between sulfur and selenium compounds and the variation in the VI/II flux ratio. Any way, a $Zn_{1-x}Cd_xS_ySe_{1-y}$ epilayer with alloy composition of x and y can be reproduced in the composition range of x=0–0.1 and y=0–0.25, by changing cadmium and sulfur fluxes.

The RHEED patterns along the [011], [010] and [01$\bar{1}$] azimuths for a (100) ZnCdSSe surface are shown in Fig. 3.7. The streaked (1×1) RHEED pattern with a strong specular spot remained unchanged during the growth, indicating the smooth surface and cubic-structured single-crystal nature of the growing layer. In the present growth system, RHEED intensity oscillations has been observed during the growth of ZnSe, ZnSSe [176] and ZnCdSe [164] alloy systems, and has been applied to the fabrication of multilayered structures. Likewise, as for ZnCdSSe quaternary alloys, the RHEED intensity oscillations during the growth were observed for the first time. Figure 3.8 shows the variation of the specular beam intensity in the RHEED pattern from a (100) ZnCdSSe surface along the [011] azimuth. When the growth was resumed by supplying group-II sources after growth interruption where only group-IV sources were supplied to the surface, cyclic intensity oscillations that continued to more than 40 periods were clearly observed. The oscillations became weaker with increasing layer thickness, but after interruption and resumption of the growth, strong oscillation was observed again. This indicates that the growth occurs with a two-dimensional layer-by-layer mechanism. Thus, it is possible to fabricate multilayered structures with very smooth and abrupt interfaces and precisely controlled thickness of each layer.

Structural quality was assessed by X-ray diffraction measurement. Figure 3.9 shows the double-crystal X-ray rocking curve of the (400) diffraction peak of a 0.96 μm-thick $Zn_{0.95}Cd_{0.05}S_{0.15}Se_{0.85}$ film on a 600 Å-thick ZnSe buffer layer. The crystal structures of CdSe and CdS are usually hexagonal wurzite while those of ZnSe and ZnS are cubic zinc blende In ZnCdSSe, which is their alloy, instability of the crystal structure may exist, which results in generation of defects with high

[011̄]   **[010]**   **[011̄]**
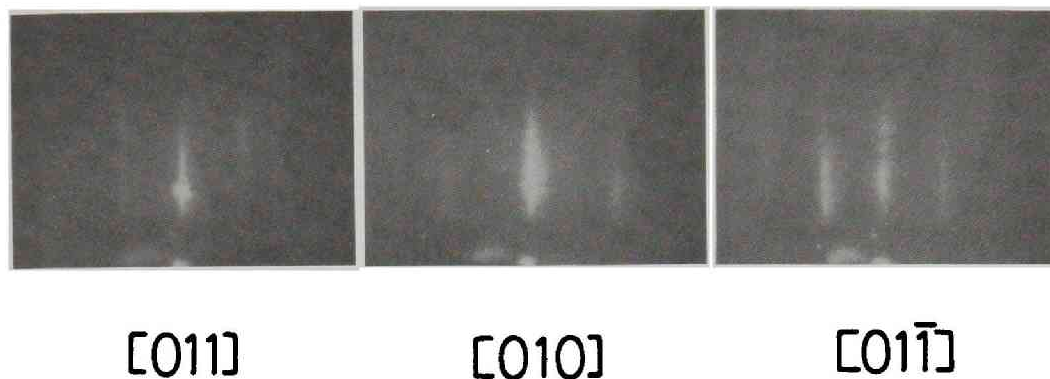
Figure 3.7: RHEED patterns observed along [011], [010] and [011̄] azimuths for a (100)-oriented ZnCdSSe surface.
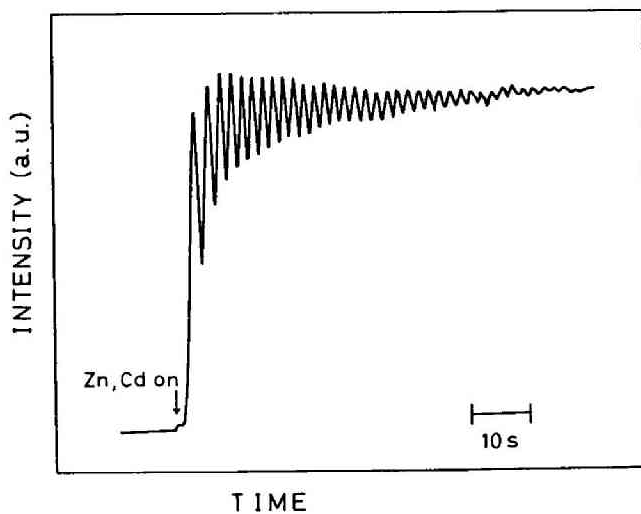
Figure 3.8: Intensity oscillations of the specular beam in the RHEED pattern observed for a (100) ZnCdSSe surface along the [011] azimuth.
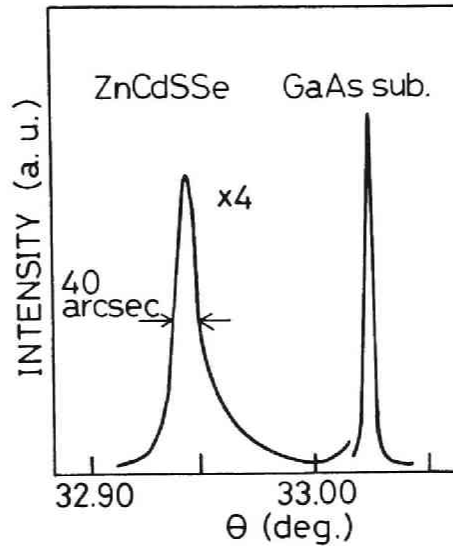
Figure 3.9: Double-crystal X-ray diffraction rocking curve of a 0.96 μm-thick layer of $Zn_{0.95}Cd_{0.05}S_{0.15}Se_{0.85}$ on a 600 Å-thick ZnSe buffer layer on GaAs. The lattice mismatch between this layer and the substrate is about 0.1 % assuming that elastic constant of the layer is equal to that of ZnSe.

concentration. However, as seen in Fig. 3.9, a full-width at half-maximum (FWHM) of a cubic (400) diffraction peak was as small as 40 arcsec. This implies that the ZnCdSSe quaternary layer has a zinc blende structure with excellent crystallographic quality. This is probably attributed to the relatively low cadmium composition of the ZnCdSSe layer and two-dimensional growth on the GaAs substrate in a nearly lattice-matched condition in the present experiments. As regards the quality of the ZnCdSSe layer with higher composition of cadmium and sulfur, further investigation is needed.

The 4.2 K PL and reflection spectra of $Zn_{0.95}Cd_{0.05}S_{0.15}Se_{0.85}$ are shown in Fig. 3.10. The main peak at 2.794 eV is probably due to the radiative recombination of bound excitons because it is located near the absorption edge determined by the reflection spectrum, as indicated by an arrow in Fig. 3.10(a). Temperature dependence of emission intensity of this peak shows two-step quenching characteristics with activation energy values of 4 and 19 meV, respectively, which indicates that the origin of this peak is a radiative recombination of excitons bound to neutral donors. However, the origin of donor species is not clear at this moment. Emission intensity of deep-level peaking at around 2.3 eV is considerably smaller than that

of the main peak, indicating a low concentration of deep radiative centers. These results indicate good optical quality and support the high quality of ZnCdSSe quaternary alloy epilayers grown by MOMBE.
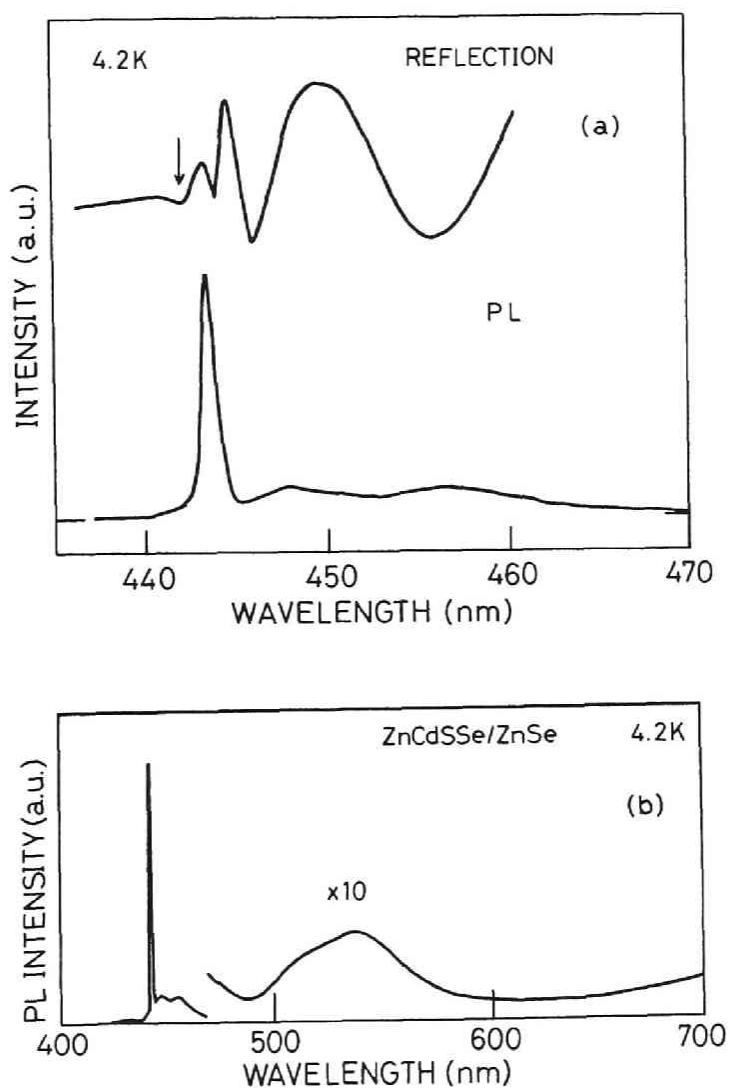
Figure 3.10: 4.2K PL spectra of a $Zn_{0.95}Cd_{0.05}S_{0.15}Se_{0.85}$ layer on GaAs: (a) excitonic emission region; and (b) entire visible region. Reflection spectrum is also drawn in (a).

3.4   Fabrication of optically pumped lasers

In this section, fabrication of optically pumped lasers with double-heterostructures (DH structures) and modified MQW structures on GaAs substrates using ZnCdSSe is described. Figures 3.11 and 3.12 shows the DH structures, "DH1" and "DH2", as well as the calculated results of band-lineups, refractive indices (n) and optical confinement factors (Γ_{opt}) [180]. For comparison with PL spectra taken at 4.2 K, the band-lineups were calculated using parameters at 4.2 K, while the band-lineups at room temperature (RT) were calculated in Chapter 2. In the calculation of band-lineups, effect of strain was taken into account assuming that all the layers were pseudomorphic. This assumption is probably valid judging from double crystal X-ray rocking curves and surface morphology. Γ_{opt} was calculated assuming that the thickness of the cladding layers was infinite. For a GaAs-$Al_{0.4}Ga_{0.6}As$ DH structure laser with a 1000 Å thick active layer, $\Gamma_{opt}=0.3$ [180], while $\Gamma_{opt}<0.1$ for a graded-index waveguide separate-confinement heterostructure single quantum well (GRIN-SCH) laser [167]. Therefore, Γ_{opt} values in the DH structures fabricated are comparable to those in conventional III-V lasers.

In the growth of these DH structures, source supply of sulfur and selenium was kept constant, i.e., the ZnCdSSe active layer was grown on the ZnSSe barrier only
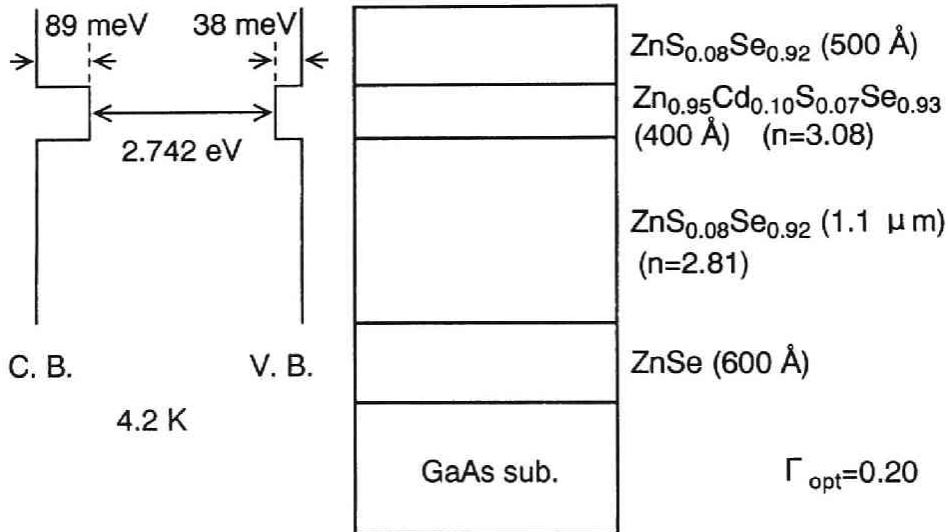
Figure 3.11: Schematic structure of DH structure "DH1". Calculated results of band-lineup, refractive indices n and optical confinement factor Γ_{opt} are also inserted.
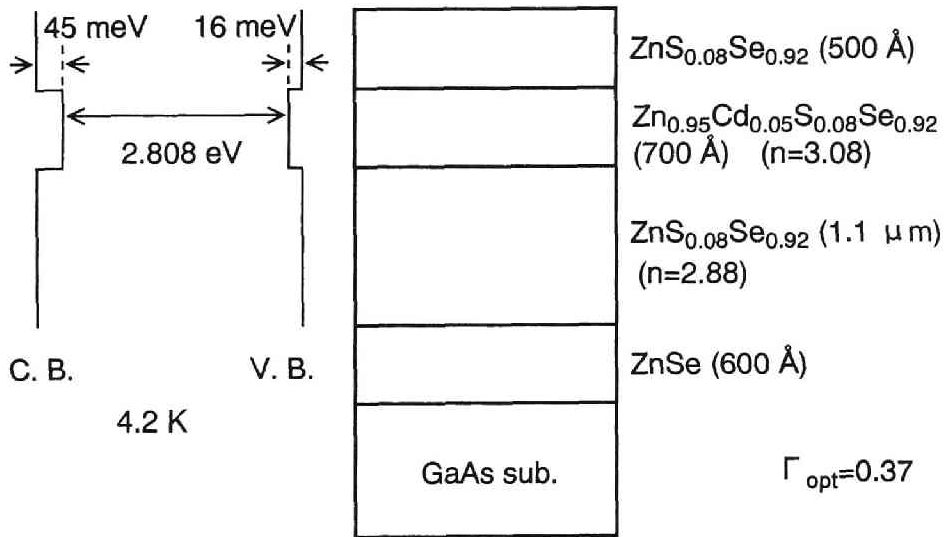
Figure 3.12: Structure of "DH2" and calculated results.
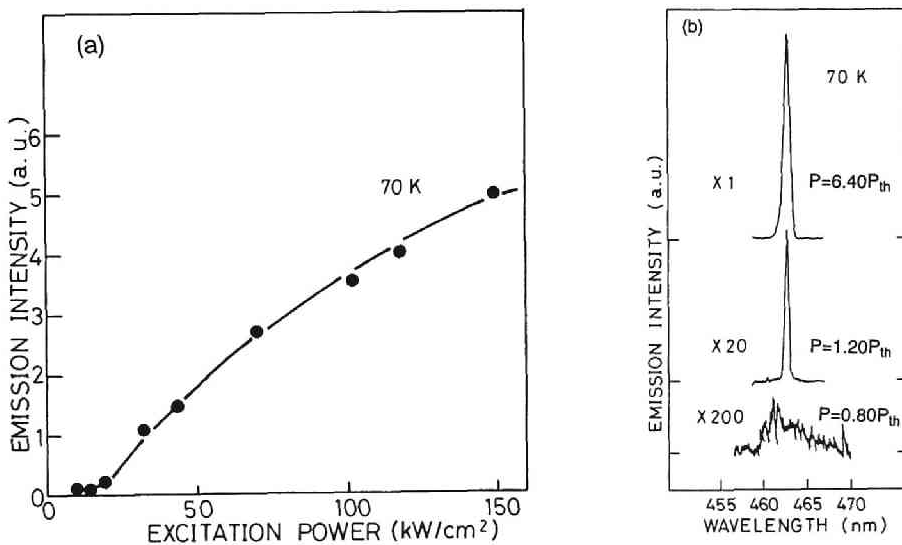
Figure 3.13: (a) Excitation power density dependence of emission intensity from the DH structure "DH1" at 70 K. P_{th} value is estimated at 18 kW/cm^2. (b) Emission spectra at 70 K below and above the lasing threshold.

by adding cadmium flux. As described in the previous section, it is likely that sulfur composition decreases by adding cadmium. By using this effect, it is expected that DH structures with type-I band-lineups can be easily realized, i.e., the incorporation of cadmium and the decrease of sulfur composition result in conduction- and valence-band-offsets, respectively.

4.2 K PL from the both DH structures exhibited the strong emission originated from the ZnCdSSe active layers, which indicated that excited carriers were collected in the active layer. Therefore, these DH structures seem to possess the type-I band-lineup, as has been predicted by the calculation. PL peak energies are 2.699 eV and 2.796 eV for DH1 and DH2, respectively, while the bandgaps calculated from the composition are 2.742 eV and 2.808 eV at 4.2 K, respectively.

To achieve laser action in these structures by optical pumping, samples were prepared by cleavage with the cavity length of 200–300 μm, and were excited by a pulsed N_2 laser, whose maximum output power, pulse width and repetition rate were 500 kW, 7 ns, and 10 Hz, respectively. Figure 3.13 (a) shows emission intensity dependence on excitation power density at 70 K. Above threshold excitation power density (P_{th}) of 18 kW/cm^2, emission intensity rapidly increases with increasing excitation power density. Figure 3.13 (b) shows the emission spectra below and above the threshold excitation power density. Above the threshold, a sharp emission peaking at 463 nm appeared, while a weak and broad emission was observed below the threshold. Above results are clear evidence of the laser action above the threshold. Laser action was observed also in DH2, as shown in Figs. 3.14 (a) and (b), which shows the P_{th} value of 200 kW/cm^2 and lasing wavelength of 447 nm. Larger P_{th} value in DH2 than in DH1 is probably due to smaller band offsets, i.e., weaker carrier confinement.

Figure 3.15 shows the schematic structure of a modified MQW structure together with the calculated band-lineups at 4.2 K and optical parameters. Although both ZnCdSSe and ZnCdSe layer are under strain in this structure, no crosshatched morphology was seen on the surface, which implies that the density of misfit dislocations is quite low. This structure exhibited intense PL emission peaking at 2.685 eV at 4.2 K as shown in Fig. 3.16. In reflection spectrum also drawn in Fig. 3.16, there is a dip at the energy almost equal to the emission energy; Stokes shift is less than 1 meV. Therefore, the origin of this emission is identified as the radiative recombination of free excitons confined into the ZnCdSe well layers. Furthermore, the very small value of Stokes shift suggests structural perfectness of the modified MQW. However, it should be noted that the calculated bandgap of 2.740 eV is different from the PL peak energy of 2.685 eV; this difference of 55 meV is too large for the
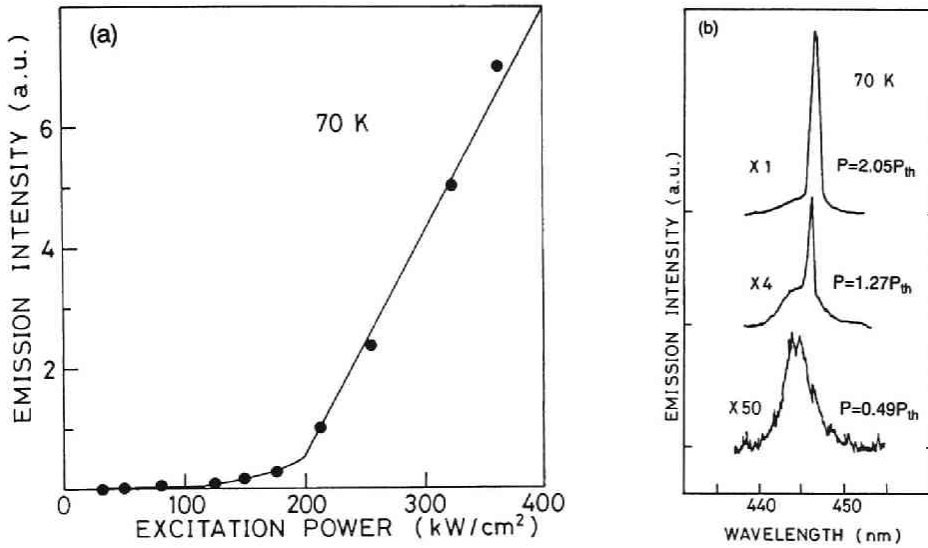
Figure 3.14: (a) Excitation power density dependence of emission intensity from the DH structure "DH2" at 70 K. P_{th} value is estimated at 200 kW/cm^2. (b) Emission spectra at 70 K.
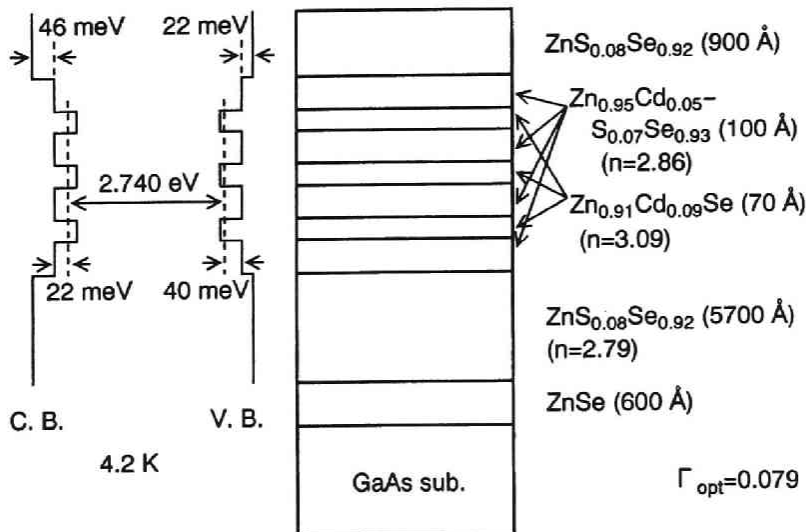

Figure 3.15: Schematic illustration of a modified MQW structure and calculated results of band-lineups, refractive indices and optical confinement factor.
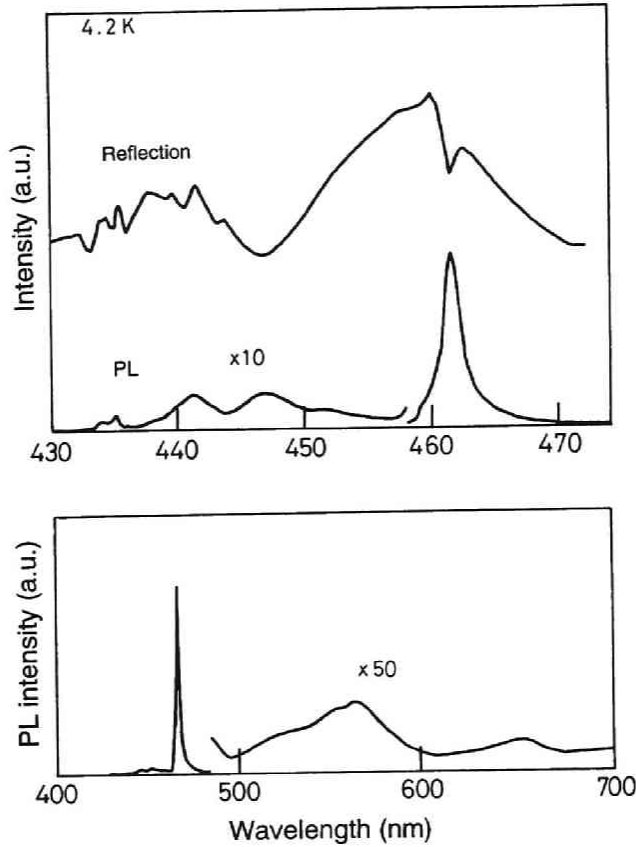
Figure 3.16: 4.2 K PL spectra of modified MQW structure. Strong emission peaking at 461.7 nm (2.685 eV) was observed. Reflection spectrum, in which a dip at 461.6 nm (2.686 eV) corresponding to the quantized level in the ZnCdSe well was observed, is also shown. Stokes shift is less than 1 meV.

binding energy of free exciton even if enhancement of the binding energy by quantum confinement is taken into account. This discrepancy seems to be due to uncertainty in solid composition in the MQW structure and/or in physical parameters used in the calculation. Therefore, more experimental data are needed to identify the factor.

Figure 3.17 (a) shows the excitation power density dependence of emission intensity peaking at 466 nm at 70 K. Figure 3.17 (b) shows emission spectra. From these figures, laser action was confirmed above P_{th} of 20 kW/cm^2.

As have been shown above, laser operation was obtained in the multilayered structures with ZnCdSSe quaternary alloy layers. This suggests that the quality of the ZnCdSSe layers is good enough to be used in the fabrication of blue/blue-
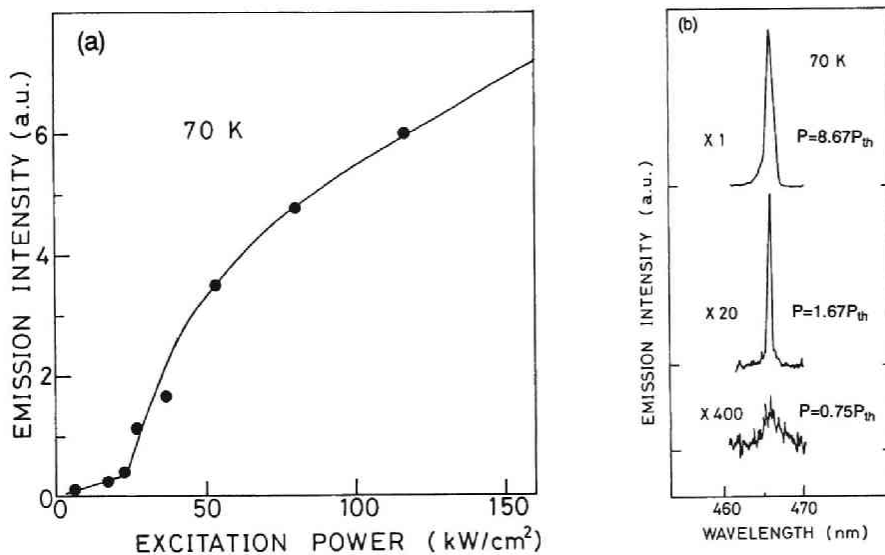
Figure 3.17: (a) Excitation power density dependence of emission intensity at 70 K from a modified MQW structure shown in Fig. 3.15. P_{th} value is about 20 kW/cm^2. (b) Emission spectra for various excitation power density.

green light-emitting devices. However, three samples mentioned above did not show lasing at RT, while the ZnCdSe-ZnSSe MQW system ever reported exhibited very low threshold at RT. This is mainly due to the larger bandgap of the active layer in the laser structure investigated in this study (2.6–2.7 eV at RT) compared to the ZnCdSe-ZnSSe MQW samples (about 2.5 eV). The advantage of the use of ZnCdSSe would be clear if the characteristics are compared at the same emission wavelength. In other words, high performance will be accomplished by optimizing the growth conditions and the structural parameters, e.g., layer thickness and alloy composition. In fact, very recently in 1993, Schetzina *et al.* reported blue LEDs with a ZnCdSSe-ZnSSe MQW structures on GaAs, which exhibited highly improved efficiency and luminance compared to the blue LEDs ever reported [181]. This improvement seems to be due to increased flexibility in the device design as a result of the use of ZnCdSSe quaternary alloys, which is just the same idea as proposed in this study.

3.5 Summary

In this chapter, growth and characterization of ZnCdSSe quaternary alloys on GaAs substrate were described. Experimental values of lattice constant and PL peak

energy were compared with the calculated values, and qualitative agreement was confirmed. RHEED intensity oscillation was observed during the ZnCdSSe growth by MOMBE technique, which indicates two dimensional growth. The quaternary alloys exhibited good crystallographic and optical properties.

Using ZnCdSSe, three types of multi-layered structures, i.e., two DH structures and a modified MQW structure, were fabricated. In particular, the modified MQW structure showed very small Stokes shift of less than 1 meV, which indicates perfectness of the structure. Optically pumped laser operation was observed at 70 K in these three types of the structures. These results suggest that designed type-I band-lineups was realized using ZnCdSSe, and that the ZnSe-based ZnCdSSe system has high potential for the application to the blue/blue-green region optoelectronic devices such as LEDs and LDs.

Chapter 4

ZnS-based structures grown by gas-source molecular beam epitaxy on GaP substrates

4.1 Introduction

In Chapter 2, two types of light-emitting device structures, i.e., ZnSe-based structure on GaAs for blue/blue-green region and ZnS-based structure on GaP for ultraviolet (UV)/near-UV region, have been proposed. The former one, where ZnCdSSe *assists* the ZnCdSe/ZnSSe system, has been investigated in Chapter 3, and it was shown that high-quality ZnCdSSe layers and their heterostructures were fabricated. In this chapter and the next chapter, the subject is shifted to the latter one, where ZnCdSSe plays an essentially important role for the desired band-lineups for light-emitting devices.

High-quality undoped and n-type ZnS has been grown by metalorganic vapor phase epitaxy (MOVPE) [89, 182, 183] and molecular beam epitaxy (MBE) [184], while low-resistive and reproducible p-type ZnS has not been reported yet [62, 64]. As for ZnS-based alloys and their heterostructures, there have been only a small number of reports on the growth of ZnSSe lattice-matched to GaP by MOVPE [185], and ZnCdS/ZnS strained-layer superlattices on GaAs by MOVPE [72, 74] and MBE [186]. Generally speaking, the growth technique for ZnS and ZnS-based alloys is not well-established, unlike the case for ZnSe.

To construct multilayers with controlled thickness and flat and abrupt interfaces, such as ZnCdSSe/ZnSSe proposed in this study, MBE-based techniques seems to be suitable. In these techniques, the choice of sulfur source is an important problem since it is not easy to treat an elemental sulfur source with a conventional Knudsen cell (K cell) owing to its very high vapor pressure. One possible solution is the use of a specially designed cell for an elemental sulfur source. This approach will be

described in the next chapter. The other solution is the use of the alternative sulfur source, i.e., other solid source or a gaseous source of sulfur.

As a solid sulfur source other than elemental sulfur in molecular beam epitaxy, ZnS [39,187] is commonly used. In particular, it is widely used in the growth of ZnSSe nearly lattice-matched to GaAs, i.e., alloys with small sulfur composition [188,189]. However, for the growth of ZnS and ZnS-based alloys, i.e., films with large sulfur composition, it is impossible to control the flux ratio of sulfur to zinc, especially in S-rich condition. This would result in the difficulty for the control of electrical and optical properties of the ZnS-based crystals. Another interesting approach is the use of electrochemical sulfur source reported by Prior *et al.* [190]. However, they could produce ZnSSe alloys with only small sulfur composition; maximum sulfur composition was 0.2. Therefore, it is considered that large sulfur flux, when growth rate was reduced down to 0.05 μm/h. which is needed to grow ZnS-based crystals, cannot be obtained using this technique.

Another alternative sulfur source is a gaseous source. Gas-source MBE (GSMBE) technique including metalorganic MBE (MOMBE), which uses gaseous source(s), is essentially suitable for the growth of materials which consist of elements having high vapor pressure, such as sulfur. This is because supply of gaseous source can be directly controlled stably by mass flow controller (MFC), while that of solid source is controlled only by the cell temperature and becomes unstable for low operating temperature as a result of high vapor pressure.

GSMBE of ZnS has been reported by a few authors [191–193]. However, the technique for high quality ZnS including the choice of sources for sulfur and other elements is not well-established. Furthermore, ZnS-based alloys and their heterostructures has not grown by GSMBE to the best of author's knowledge.

In this chapter, on the basis of these background, growth and characterization of ZnS-based crystals by GSMBE are described. Investigations to fabricate multi-layered structure is also presented [99].

4.2 Growth systems and techniques

The epitaxial layers were grown in ANELVA KMV-101 GSMBE system, where metallic zinc, metallic cadmium, dimethylselenide (DMSe), and hydrogen sulfide (H$_2$S) were used as source materials. This system is basically the same as that used in Chapter 3, except that metallic zinc was used instead of the metalorganic. This change made it possible to reduce the background pressure during the growth for equivalent source supply of zinc, and to increase the supply of sulfur maintaining a

Table 4.1: Typical growth conditions.

Substrate temperature	200 °C
Zn cell temperature	330 °C
Cd cell temperature	220–240 °C
DMSe flow rate	18–54 μmol/min
H$_2$S flow rate	260 μmol/min

MBE condition, i.e., sufficient mean free path. Flow rates of DMSe and H$_2$S were controlled by MFCs and these source gases were cracked at 820 °C and 1100 °C, respectively. For zinc and cadmium, conventional K cells were used. GaP was used as a substrate. The orientation of the surface was (100)±0.5° or (100) tilted 6° toward [01$\bar{1}$].

The pretreatment process of GaP for the epitaxial growth of ZnS-based crystals is not well established. In this study, the GaP substrates were pretreated tentatively as following: (1) degreasing; (2) etching in a HNO$_3$:HCl:H$_2$O=1:2:2 solution; (3) cleaning in water; (4) dipping into a HF solution for several sec; (5) dipping into a (NH$_4$)$_2$S$_x$ solution for 5 min; (6) cleaning in methanol; (7) drying; (8) loading into the exchange chamber; and (9) heating up to about 400 °C before growth. Here, the (NH$_4$)$_2$S$_x$ treatment [178] is reported to be effective for two dimensional nucleation of ZnSe-based crystals on GaAs substrates [179,194]. For GaP substrates, reduction of surface state density by the (NH$_4$)$_2$S$_x$ treatment, as in the case for GaAs [195], was reported [196], and effectiveness of the treatment for MOVPE of high-quality (Al,Ga)P was also shown [197]. Therefore, the (NH$_4$)$_2$S$_x$ treatment is believed to be effective for GSMBE of ZnS-based crystals. Typical growth conditions are summarized in Table 4.1. As for the flow rate of H$_2$S, preliminary experiments indicated that large H$_2$S flow rate was needed for the practical growth rate owing to very low sticking coefficient of sulfur source molecules. Therefore, the flow rate of H$_2$S was fixed at as large as 260 μmol/min, which is almost the maximum value in the present growth system.

4.3 Growth and characterization

4.3.1 ZnS

To construct ZnCdSSe/ZnSSe (ZnCdS) heterostructures, it is necessary to control composition of ternary and quaternary alloys. However, since fundamental growth

parameters such as the substrate temperature and the ratio of group-VI flux to group-II flux for GSMBE of ZnS-based crystals are not established, the situation is complicated; composition control and optimization of the above parameters should be accomplished at the same time, which seems to be rather difficult. Therefore, it is thought that these parameters are established for the simple binary compound, ZnS, and then, the growth conditions of ternary and quaternary alloys are investigated as a perturbation from the ZnS growth.

Firstly, dependence of growth rate on substrate temperature (T_{sub}) was investigated. At $T_{sub} = 300\,°C$, which is the normal temperature for MBE of ZnSe, growth rate was small, typically less than 1000 Å/h even for the very large H_2S flow rate of $260\,\mu mol/min$. This low growth rate is not practical for the device fabrication. This is probably due to incomplete decomposition of H_2S and low sticking coefficient of source species. Quadrupole mass analysis (QMA) study of the cracking characteristics of H_2S in the present system showed that H_2S pyrolysis began at the cracking temperature (T_{cr}) of about 900 °C, and cracking efficiency continued to increase as T_{cr} was raised up to 1200 °C [198]. Therefore, at $T_{cr} = 1100\,°C$, which was chosen to suppress corrosion of tantalum baffle by H_2S, only a small amount of H_2S was decomposed. On the other hand, it was reported that in MBE growth of ZnS using elemental sulfur, growth rate decreased when sulfur molecules were cracked [199]. This means that the cracked molecules have the lower sticking coefficient than the molecules evaporated from elemental sulfur (S_8). Therefore, sulfur source species produced by the cracking of H_2S, probably S_1 or S_2, have a low sticking coefficient. For these reasons, lower T_{sub} of 200 °C, where the growth rate of ZnS was typically 2000 Å/h, was adopted to increase the sticking coefficient of the source molecules and to avoid the degradation of crystallographic quality due to too low T_{sub}.

Since the flow rate of H_2S was fixed at $260\,\mu mol/min$, which was near the upper limit in the present growth system, the ratio of the group-VI flux to the group-II flux was changed only by changing the zinc cell temperature. The effect of the flux ratio on the film quality was not clearly observed. Therefore, in the following section, the zinc cell temperature, typically 330 °C, was chosen so that growth was carried out under the condition between Zn-rich and Se-rich condition which was judged by the growth rate dependence on the zinc cell temperature.

4.3.2 ZnSSe and ZnCdS

As cladding layers in UV/near-UV light-emitting devices proposed in this study, ZnSSe or ZnCdS lattice-matched to GaP should be used. In this section, growth
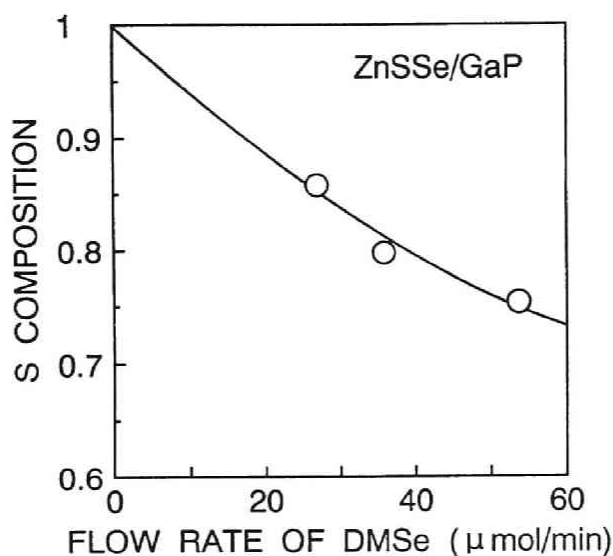
Figure 4.1: Sulfur composition of the ZnSSe ternary alloys grown on GaP substrates at different flow rate of DMSe.

and characterization of ZnSSe and ZnCdS are described. A comparison of ZnSSe and ZnCdS as cladding layers is also discussed.

Figure 4.1 shows the sulfur composition y in the ZnS_ySe_{1-y} ternary layers as a function of the DMSe flow rate under a constant H_2S flow rate of 260 μmol/min. The sulfur composition was determined by X-ray diffraction. As the flow rate ratio of $[H_2S]/([H_2S]+[DMSe])$ was decreased from 1 to 0.81 by increasing the DMSe flow rate, sulfur composition decreased from 1 to 0.75. Surface morphology was typically specular to the naked eyes. However, double-crystal X-ray rocking-curve (XRC) measurements revealed large full-width at half maximum (FWHM) of the diffraction peaks for the epitaxial layers with thicknesses of about 0.6–0.8 μm irrespective of the composition (*e.g.* about 1000 arcsec), even for the composition for lattice-matching ($y \sim 0.84$).

$Zn_xCd_{1-x}S$ alloys were also grown, and cadmium composition was controlled by changing zinc and cadmium cell temperature. However, FWHM of XRC of ZnCdS was larger than that of ZnSSe, typically 1500–2000 arcsec for the thickness of about 0.5 μm. In addition, the lattice-matching effect, i.e., redution of FWHM around the composition for lattice-matching ($x \sim 0.10$), was not observed.

Poor quality of these ternary alloy epitaxial layers in the high sulfur composition range prepared by the present growth technique may be due to the fluctuation of
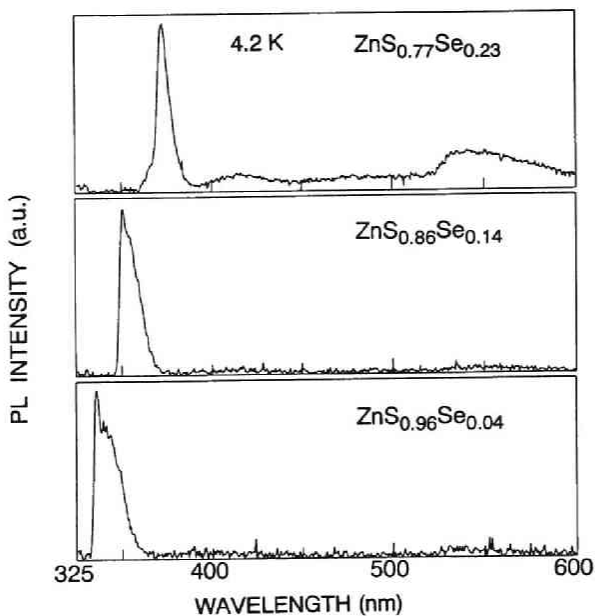
Figure 4.2: 4.2 K PL spectra of ZnSSe for various composition.
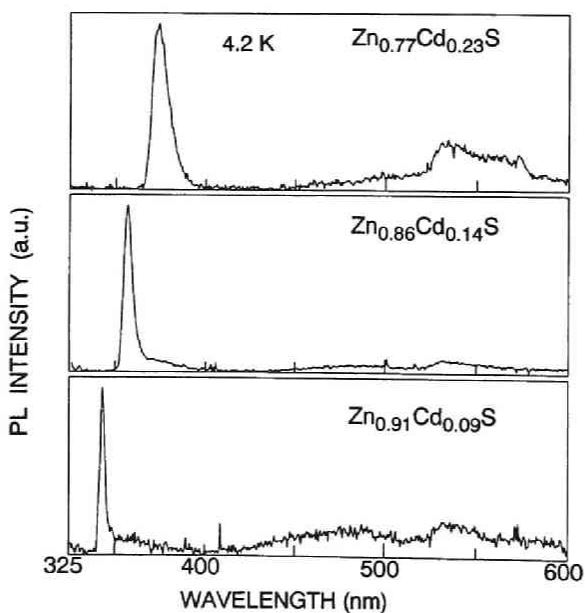
Figure 4.3: 4.2 K PL spectra of ZnCdS for various composition.

alloy composition during the growth or large defect density, although we could not identify any cause at the present stage.

Photoluminescence (PL) spectra were measured using a He-Cd laser (325 nm) as a excitation source with excitation power density of about 500 mW/cm^2. Figures 4.2 and 4.3 show PL spectra of ZnSSe and ZnCdS at various composition, respectively. Although FWHM values of XRC of ZnCdS layers were larger than those of ZnSSe layers, ZnCdS layers exhibited a relatively sharp PL peak especially at $x=0.09$, where FWHM was 34 meV. Therefore, ZnCdS would be a good material for optical devices if the crystallographic quality is further improved.

Although both ZnSSe and ZnCdS are not satisfactory in the point of crystallographic quality, ZnSSe had better crystallographic quality than ZnCdS. Therefore, at the present stage, it seems better to use ZnSSe as the cladding layers.

4.3.3 ZnCdSSe

Several ZnCdSSe quaternary alloys were grown on GaP substrates. Table 4.2 shows the growth conditions of ZnCdSSe quaternary alloys. Composition of ZnCdSSe was determined by energy dispersive X-ray analysis (EDX).

Figure 4.4 shows PL spectra of ZnCdSSe alloy layers grown under the conditions summarized in Table 4.2. Each of them is seen to consist primarily of a broad emission band, which is thought to be close to band edge. In Table 4.3, some physical properties of these epitaxial layers obtained experimentally as well as the estimated values by calculation are summarized. Namely, solid compositions of the alloys were determined by EDX and lattice constants were measured by X-ray diffraction. $E_{PL}{}^h$ is defined as the highest energy in the luminescence tail, as indicated by arrows in Fig. 4.4. Lattice constant at room temperature and bandgap at 4.2 K ($E_{g,cal}$) calculated from the alloy composition are also shown in Table 4.3. The measured lattice constants are seen to agree fairly well with the calculated results. Regarding

Table 4.2: Growth conditions of ZnCdSSe.

Sample	Zn cell temperature (°C)	Cd cell temperature (°C)	H$_2$S flow rate (μmol/min)	DMSe flow rate (μmol/min)	Substrate temperature (°C)
A	330	220	260	54	200
B	330	240	260	36	200
C	330	240	260	54	200
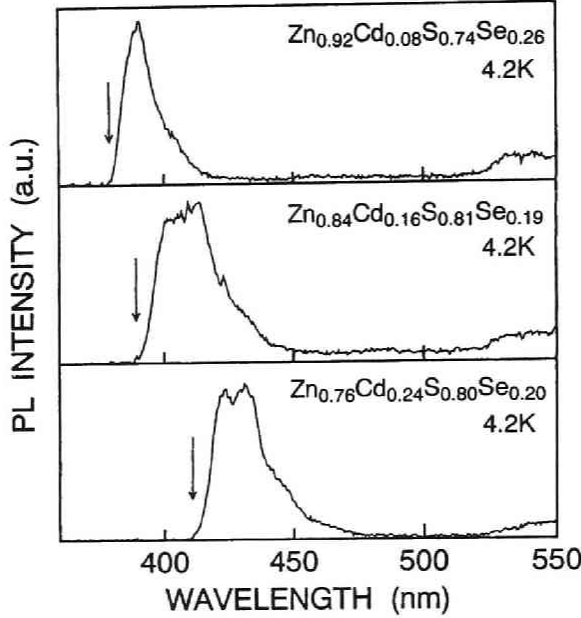
Figure 4.4: 4.2 K PL spectra of ZnCdSSe quaternary alloys. The arrows indicate the highest energies in the luminescence tail, E_{PL}^h.

$E_{g,cal}$ and E_{PL}^h, the trend of the change with composition is consistent for the two parameters. The relationship between $E_{g,cal}$ and E_{PL}^h will be more clear if the origin of the luminescence is known.

Table 4.3: Physical properties of $Zn_{1-x}Cd_xS_ySe_{1-y}$.

Sample	Compositions determined by EDX		Measured lattice constant	Calculated lattice constant	E_{PL}^{h*} at 4.2 K	$E_{g,cal}^{**}$
	x (Cd)	y (S)	(Å)	(Å)	(eV)	(eV)
A	0.08	0.74	5.51	5.510	3.27	3.365
B	0.16	0.81	5.53	5.525	3.19	3.327
C	0.24	0.80	5.57	5.561	3.02	3.194

*defined as the highest energies in the photoluminescence tail, as indicated by arrows in Fig. 4.4.
**calculated bandgap at 4.2 K.

$ZnS_{0.89}Se_{0.11}$ $ZnS_{0.89}Se_{0.11}$

$Zn_{0.84}Cd_{0.16}S_{0.81}Se_{0.19}$

$\Delta E_{c}=175$ meV

4.2 K

$\Delta a/a_{sub}$
$=1.36$ %

$E_{g}=3.356$ eV
(369 nm)

$\Delta E_{v,hh}=153$ meV

Figure 4.5: Calculated band lineup of the ZnCdSSe/ZnSSe DH structure fabricated on a GaP substrate, assuming that the entire DH structure was coherently grown on the GaP.

4.3.4 Double-heterostructure

As a first trial, a ZnCdSSe/ZnSSe double-heterostructure (DH structure) was fabricated. The ZnCdSSe layer was grown under the same conditions as those of sample B in Table 4.2. The band lineup was calculated from the compositions, assuming that all the layers are coherently grown on a GaP substrate, as shown in Fig. 4.5. Since the sulfur composition of the cladding layer is slightly larger than that under the lattice-matching condition because of the difficulty in achieving the accurate composition control in the present GSMBE system, the strain accumulated into the DH structures may be partially released. However, since the effect of strain on band-offset is not large enough to change the characteristics of the band lineup, the type-I band lineup is thought to be realized.

Figure 4.6 shows 4.2 K PL spectrum of the DH structure. Although the active layer is very thin compared with the barrier layers, PL from the active layer was clearly observed. This suggests that excited electrons and holes generated at the cladding layers flow into the active layer and recombine radiately there. It is reasonable to conclude from this PL result that the type-I band lineup as shown in Fig. 4.5, which is necessary for light emitting devices, is achieved on a GaP substrate. However, relatively broad emissions from both the barrier and the active

Figure 4.6: A 4.2K PL spectrum of ZnCdSSe/ZnSSe DH structure. A schematic illustration of the structure is also inserted.

layers indicate poor qualities of the respective layers. A fairly large discrepancy of 180 meV between the calculated bandgap shown in Fig. 4.5 and the PL peak energy may be related to the broadness and the uncertainty in physical parameters used in the calculation.

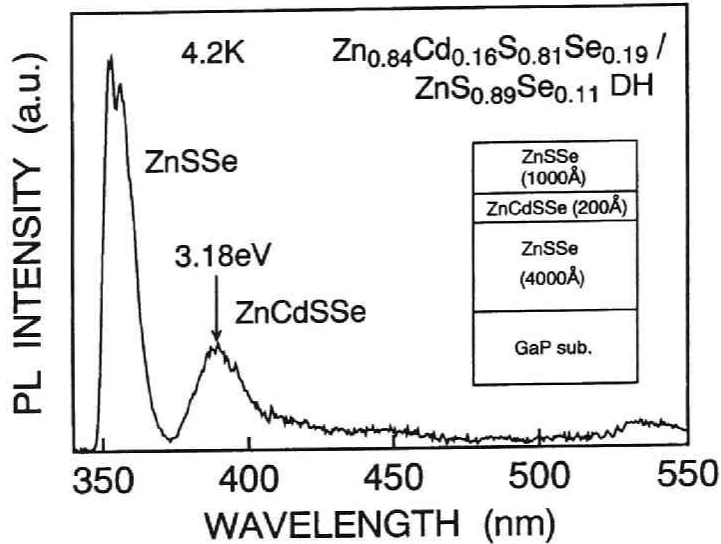Although the DH structure was fabricated as a first trial as stated above, the quality of layers must still be significantly improved. Considering the fact that the high-quality ZnSSe/GaP is realized by MOVPE [185], we believe that the poor quality of the layers is related to the difficulty in growth of alloy layers with large sulfur compositions by GSMBE. Therefore, some improvements on present GSMBE technique are clearly necessary. The key factor seems to be the choice of gaseous source of sulfur. The problem of the use of H_2S seems to be the low cracking efficiency (high decomposition temperature) and the low sticking coefficient of source species (resulting low substrate temperature). Therefore, a gaseous source which can be decomposed at low temperature into the species having a high sticking coefficient is desired. Organic compounds of sulfur, diethylsulfide and tertiary-butylmercaptan were tentatively used, although the detail is not described here. These compounds were decomposed at lower temperature than H_2S, which was judged from QMA study, but the growth rate was considerably low; even lower than the case using H_2S. This may be due to the difference of molecular species or influence of hydrocarbon

radicals. On the other hand, the background pressure became higher owing to generated hydrocarbon radicals.

Therefore, the use of other appropriate gaseous source or some improvements of the growth system, such as bubbling with hydrogen or reduction of the distance between a cell and a substrate [172], or the use of a high-pressure type gas-cell [169] for the more efficient cracking, seems to be needed.

4.4 Summary

In this chapter, growth and characterization of ZnS-based crystals were described. Solid composition of ternary and quaternary alloys can be controlled by GSMBE. For ZnCdSSe, experimental results of lattice constant and PL energies were compared with calculated values. Quantitative agreement was obtained for lattice constant, while calculated bandgaps and experimental PL energies agreed qualitatively. However, it was found that the crystallographic quality of the epitaxial layers was rather poor, which may result from composition fluctuation or large defect density caused by the relatively low substrate temperature (200 °C). In principle, GSMBE technique is probably suitable for the material containing elements having high vapor pressure such as sulfur, but, appropriate gas-source should be developed instead of H_2S.

Although the quality of the film needed to be improved, ZnCdSSe/ZnSSe DH structure was fabricated. Photoluminescence was observed from the active layer of the DH structure, which indicates carrier confinement to the active layer.

Chapter 5

ZnS-based structures grown by molecular beam epitaxy using an elemental sulfur source on GaP substrates

5.1   Introduction

As mentioned in Chapter 4, although the use of a gaseous source of sulfur is one of the promising techniques for molecular beam epitaxy (MBE) of ZnS-based crystals [191–193], an appropriate gaseous source has not been found yet. One of the problems is the low sticking coefficient of the sulfur molecular species, which are produced by cracking of the source gas, onto the substrate surface. This seems to result in the low growth rate and difficulty in stoichiometry control owing to insufficient supply of sulfur species. One of the solutions for this problem is to increase the flow rate of the source gas, but it does not allow the MBE condition, i.e., necessary mean free path, owing to the generation of excess gas by cracking.

It is expected that this problem can be solved by the use of elemental sulfur. To date, several groups have reported MBE growth of ZnS using an elemental sulfur source [38,199–203], but the growth technique of high quality crystals has not been established yet. Moreover, there have been only a small number of reports on the growth of ZnS-based alloys in MBE [70,186] and also in metalorganic vapor phase epitaxy (MOVPE) [72,74,185].

One of the problems of the use of elemental sulfur is its very high vapor pressure, which is about 10^{-6} Torr at room temperature (RT). Since the conventional Knudsen cells (K-cells) have been designed mostly for the high-temperature use of the materials such as aluminum and gallium having low vapor pressure, it is difficult to control sulfur flux stably at low temperature using them. Therefore, for the use of elemental sulfur, a cell should be designed for the exclusive use, especially for alloy growth.

63

In this chapter, the growth and characterization of ZnS-based crystals, using an elemental sulfur source with a specially designed cell, is described. First, to establish a growth technique of the ZnS-based crystals, growth conditions of ZnS and ZnS-based alloys were extensively investigated by means of reflection high-energy electron diffraction (RHEED) observation, X-ray rocking curve (XRC) measurement, transmission electron microscope (TEM) observation, photoluminescence (PL), and electrical characterization [204]. Second, fabrication of light-emitting devices, which consists of the metal-insulator-semiconductor (MIS) structure, is also presented [205].

5.2 Growth systems and techniques

Figure 5.1 shows a MBE system used in this chapter. The system consists of four vacuum chambers, i.e., a loading chamber, a transfer chamber, a II-VI growth chamber and a III-V growth chamber which is not used in this work. The loading chamber and the II-VI chamber are evacuated with a turbo molecular pump and an oil diffusion pump, respectively. The transfer chamber and the III-V chamber are pumped
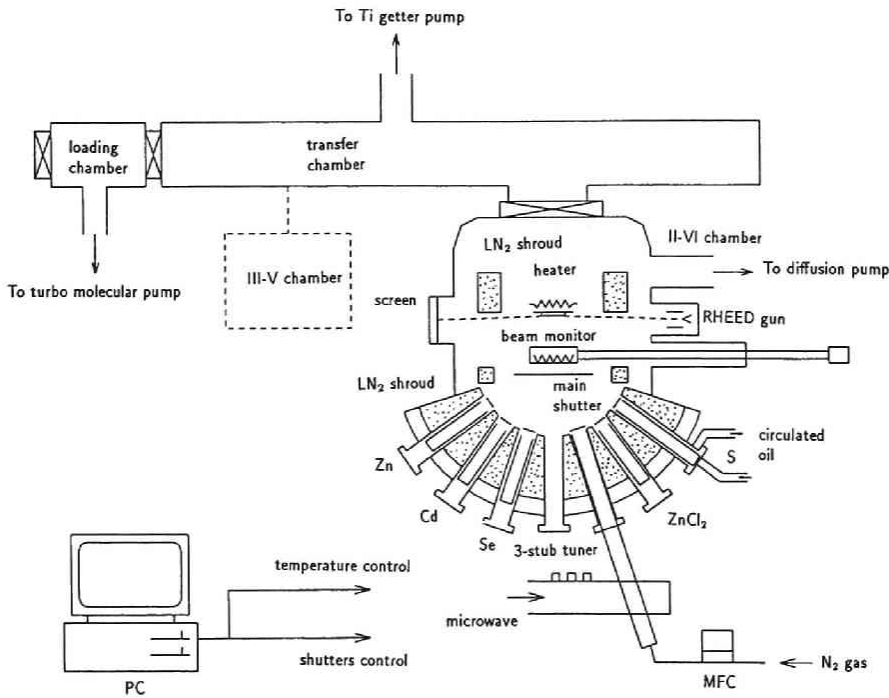

Figure 5.1: Schematic illustration of MBE system.

with ion pumps and titanium getter pumps. The background pressures in the loading chamber and the transfer chamber are the low 10^{-8} Torr and below 10^{-8} Torr, respectively. The background pressure in the II-VI chamber is relatively high owing to very high vapor pressure of sulfur at RT when the liquid nitrogen shroud is empty. However, after introduction of liquid nitrogen into the shroud, it is reduced down to less than 1×10^{-8} Torr. The growth chambers are equipped with RHEED, with which surface structure of the films can be characterized *in situ* during the growth.

Four square substrates, in the size of $1 \text{cm} \times 1 \text{cm}$, can be set into the loading chamber and the transfer chamber. Therefore, the growth can be carried out successively without interval for evacuation. Source materials for the growth are elemental zinc, cadmium, sulfur and selenium (6N purity each). As for the n-type doping, $ZnCl_2$ (5N purity) was used. Conventional K-cells were used with crucibles made of pyrolytic boron nitride (PBN), except for sulfur. Since group-II and VI elements have higher vapor pressure than group-III elements, the operating temperature of the K-cells is a relatively low value of around 200 to 300 °C. This results in instability of temperature or a large time constant of temperature variation owing to relatively small temperature difference between the cell and the surrounding. In order to raise the operation temperature as high as possible, crucibles were capped with PBN plates whose centers were drilled by 2 or 3 mm in diameter.

For sulfur, however, if we use a conventional K-cell, accurate control of beam flux cannot be achieved, owing to very low operating temperature (less than 100 °C) resulting from its very high vapor pressure. This makes it difficult to grow alloys such as ZnSSe and ZnCdSSe with sufficient uniformity of sulfur composition. In this study, a cracking cell specially designed for the use of sulfur (made by ULVAC JAPAN Ltd.) is used. Figure 5.2 shows the sulfur cell. It consists of a source effuser, a transport tube and a cracker. They are made of stainless steel, quartz and graphite, respectively. These materials are not damaged by the reaction with sulfur, although several materials, especially copper, are attacked by vapor of sulfur. The temperature of a sulfur-source effuser was kept constant using oil flowing from a constant-temperature oil bath. Stabilities of the temperature and flux intensity measured by a nude ion gauge were in the range of ±0.1 °C and ±5 %, respectively. The temperature of the cracker is kept at 200 °C. In this condition, sulfur molecules, which are S_8 for the main part, are probably not cracked to smaller species such as S_2.

Two types of GaP substrates, whose orientations are just (100) (a just (100) substrate) and misoriented 6° toward [01$\bar{1}$] (a misoriented substrate) were used. The substrates were degreased and etched and followed by the $(NH_4)_2S_x$ treatment

Cracking cell for sulfur
(made by ULVAC JAPAN, Ltd)

cracker (graphite)

transport tube (quartz)

thermocouple

oil

source effuser (stainless steel)

constant-temperature oil bath
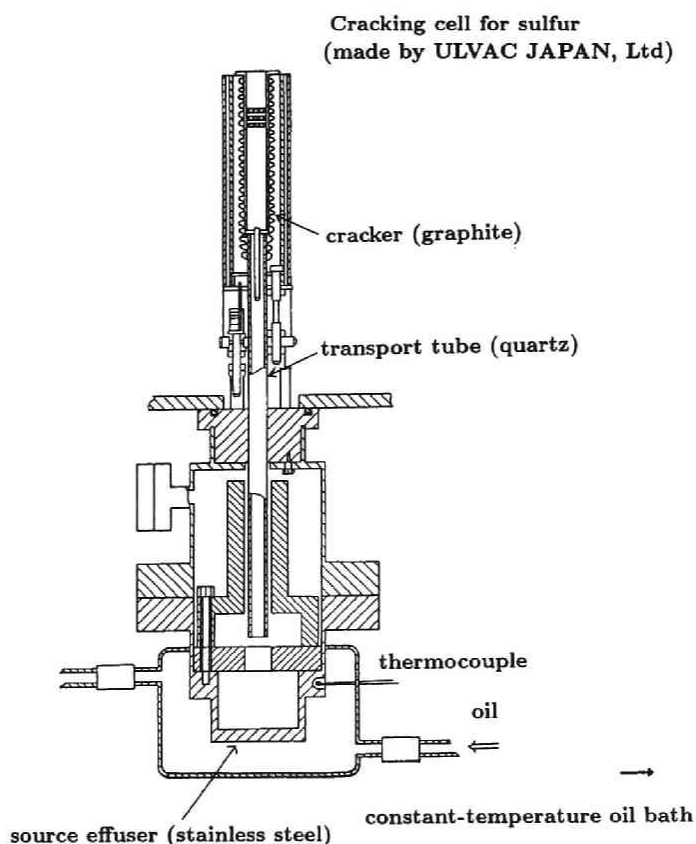
Figure 5.2: S cell specially designed for low temperature operation.

[196,197]. Before the growth, the substrates were heated in the growth chamber up to about 400 °C, or above growth temperature if the growth temperature was higher than 400 °C. In any case, thermal treatment for the desorption of surface oxide was not performed, because the oxide are not formed after the $(NH_4)_2S_x$ treatment [196]. The substrate temperature was calibrated using the melting point of tin (232 °C) and lead (327 °C).

5.3 Growth and characterization

5.3.1 ZnS

Figure 5.3 shows RHEED patterns observed when ZnS was grown directly on the misoriented substrate at the substrate temperature (T_{sub}) of 330 °C. In this case,
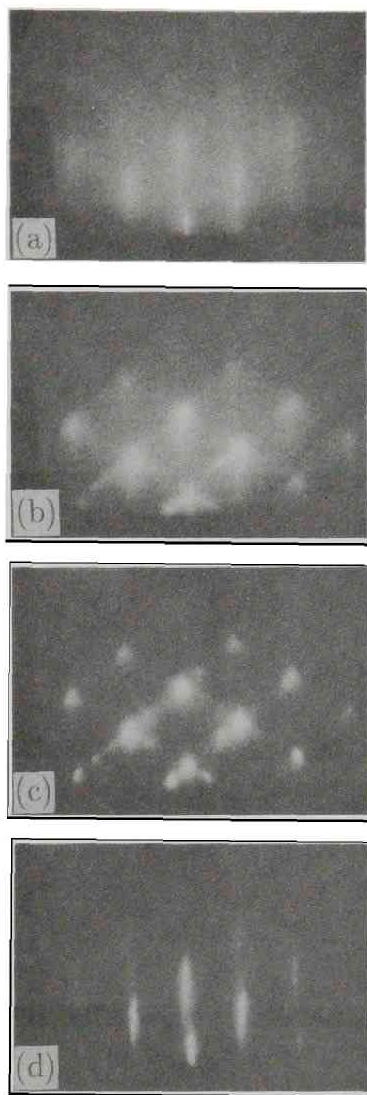
Figure 5.3: RHEED patterns along [011] direction for ZnS grown directly on GaP substrate at several thickness: (a) 270 Å; (b) 480 Å; (c) 780 Å; (d) 2300 Å. Twin spots were observed at the thickness of around 480 Å. The substrate surface is misoriented 6° toward [01$\bar{1}$] with respect to (100). Thicknesses are estimated assuming that the growth rate in the early stage of nucleation is the same as that in the growth of thick layer.
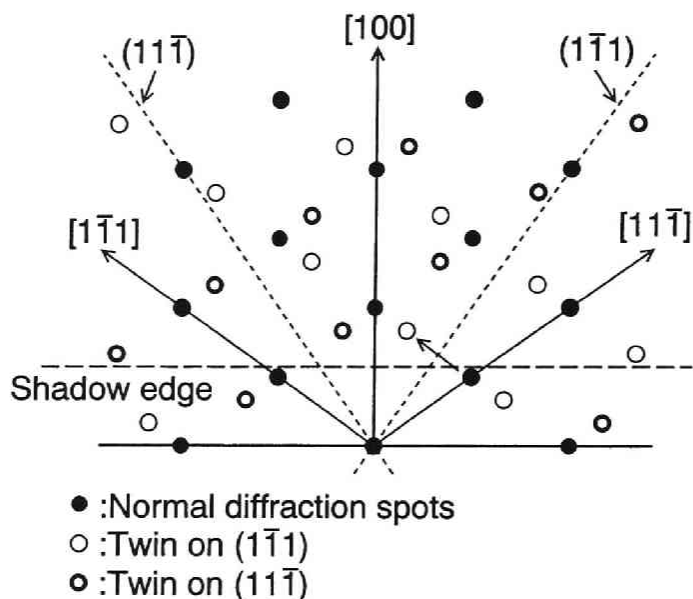
Figure 5.4: Explanation of twin spots.

RHEED pattern changes as follows: (1) diffuse spots, (2) lattice pattern, (3) spotty pattern with extra spots, (4) streak pattern. The cause of the extra spots are well-explained by formation of twin crystals. As shown in Fig. 5.4, the extra spots and normal diffraction spots are symmetrical with respect to the dashed lines which indicate $(1\bar{1}1)$ and $(11\bar{1})$ planes of the epitaxial layer. Therefore, the extra spots are due to twin crystals rotated on $(1\bar{1}1)$ and $(11\bar{1})$ planes. Such twin spots have been sometimes observed during the growth of ZnS [38,191]. In this study, twin spots were observed under wide range of growth conditions, such as substrate temperature and flux intensity of group II and VI sources, on either the just (100) or the misoriented substrates. Therefore, it seems that ZnS has tendency to form twin crystals easily. In addition, twin spots were also seen during the growth of ZnS-based alloys such as ZnSSe and ZnCdS. Appearance of such twins shows that a large number of defects are produced at the initial stage of the growth, and thus it is desirable that epitaxial growth is carried out without the twin formation. It was found that twin spots are not observed during the growth of thin ZnS buffer layer up to the thickness (t) of about 200 Å at T_{sub}=490 °C, and following ZnS growth at T_{sub}=330 °C, as shown in Fig. 5.5. In other words, ZnS can be grown without twin formation by inserting the buffer layer grown at the high T_{sub}. As will be shown later, this insertion of ZnS buffer layer improves the crystallographic quality effectively.
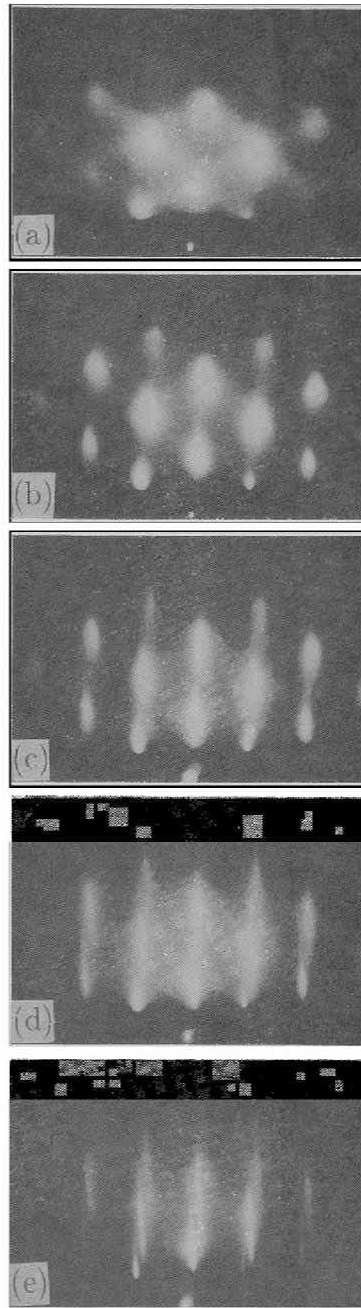
Figure 5.5: RHEED pattern observed during the growth of ZnS buffer at 490 °C ((a)–(c)) and following ZnS growth at 330 °C ((d),(e)) on the misoriented substrate: (a) 50 Å; (b) 150 Å; (c) 200 Å; (d) 410 Å; (e) 4300 Å. Twin spots were not observed during whole stage of the growth.
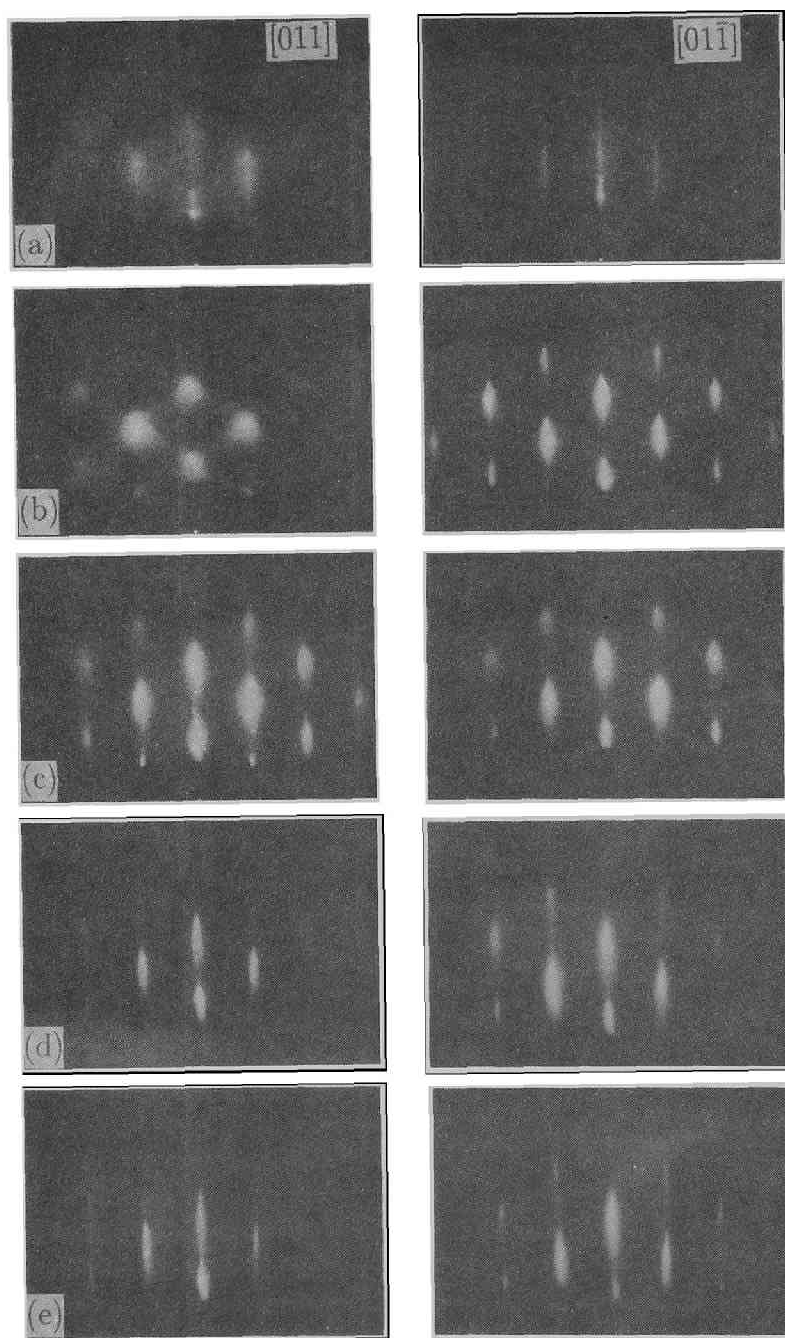
Figure 5.6: RHEED pattern along [011] and [01$\bar{1}$] direction for ZnS buffer ((a)–(c)) and ZnS ((d),(e)) on just (100)-oriented GaP substrate: (a) 20 Å; (b) 100 Å; (c) 200 Å; (d) 400 Å; (e) 6200 Å. V-shape streaks, which were not seen on the misoriented substrate, were observed along [011] direction during upper-ZnS growth ((d),(e)).

From RHEED patterns at the initial stage of the growth, it is suggested that three dimensional (3D) nucleation occurs at any substrate temperature. It is also suggested that twins were readily formed on the (11$\bar{1}$) facet at a typical substrate temperature of 330 °C. However, since twin spots became weak and disappeared as the growth proceeded, it is likely that such twins are not formed on the (100) oriented flat surface. On the other hand, during the growth of ZnS buffer layer at the high substrate temperature of 490 °C, twins are not formed probably owing to the enhancement of migration of the source species, although the initial nucleation is still 3D mode. It is also likely that ZnS or ZnSSe growth proceeds without twin formation even at T_{sub} =330 °C once the surface becomes relatively flat as a result of the high temperature growth of the ZnS buffer.

Figure 5.6 shows RHEED patterns observed during the growth of ZnS with the buffer layer on the just (100) substrate. Narrow v-shape streaks were observed along [011] direction at t=400 Å and t=1600 Å, while such patterns were not observed during the growth on the misoriented substrate (see Fig. 5.5). This indicates that two kinds of facets with small misorientation from (100) plane were readily formed, i.e., the surface was relatively rough, when the just (100) substrate was used. On the other hand, it is suggestd that smoother surface was formed on the misoriented substrate than on the just (100) substrate. Therefore, the misoriented substrates will be mainly used in the following sections.

Figure 5.7 shows full-width at half maximum (FWHM) of XRC for ZnS as a function of the thickness. FWHM values decrease with increasing thickness. For undoped and Cl-doped layers, FWHM values are clearly reduced by using the buffer layers. In addition, at t~1.7 μm, FWHM values are almost the same for undoped, Cl-doped and N-doped layers with buffers. Furthermore, FWHM values for the layers with and without buffers decrease continuously each as the thickness increases, whether the layers were doped or undoped. Therefore, it can be concluded that FWHM values are much reduced by using the buffers grown at the high substrate temperature, and that the effect of doping on FWHM of XRC is small. In Fig. 5.7, fluctuation of the data for Cl-doped layer without buffers, represented by closed squares, may indicate the effect of doping, but those data are clearly distinguished from the data with buffers. For the layers with the buffers, FWHM values are reduced down to about 300 arcsec with increasing the thickness up to 2.5 μm. This fact suggests that the crystallographic quality would be much better even for thinner films if lattice mismatch and the other bad effect of the substrate on the films, $e.g.$, influence of initial 3D nucleation, can be removed.
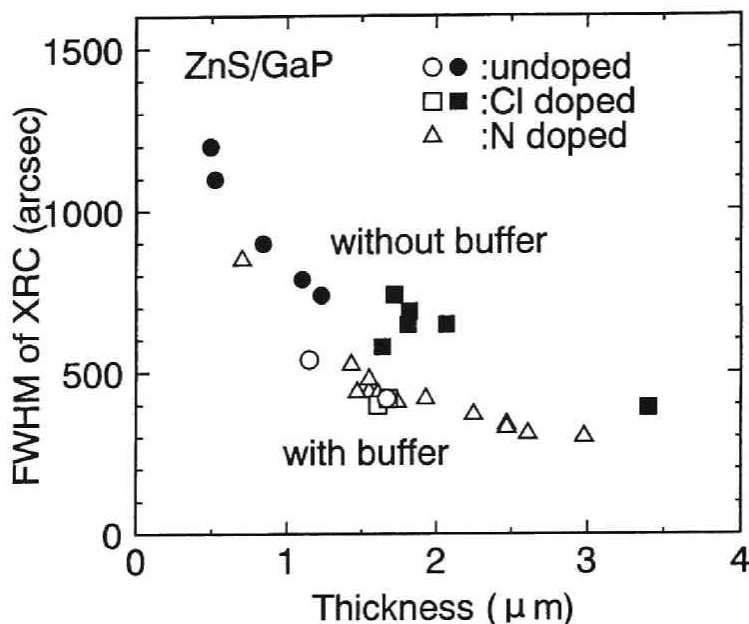
Figure 5.7: FWHM of XRC for ZnS with and without buffers as functions of film thickness. Open and closed symbols denote data point for the layers with and without buffer layers, respectively.

Figures 5.8 and 5.9 show TEM bright field images of ZnS without and with the buffer layer, respectively. In both figures, the regions with high concentration of defects, the dark region, are seen near the ZnS/GaP interfaces. The thickness of the defect region is thinner in the film with the buffer. This is probably related to the fact that twin spots were not observed by RHEED when the buffers were used, and coincides with the results of of XRC measurement. These results suggest that the control of the interface between the GaP substrate and the epitaxial layer is very important for the growth of high quality epilayers.

The 200 Å thick ZnS buffer layers grown at T_{sub}=490 °C have been used for the growth of lattice-matched ternary alloys as shown in the following sections. If the lattice of the buffer relaxes owing to lattice-mismatch between ZnS and GaP (0.76 %), the pseudomorphic structure based on ZnSSe (ZnCdS)/GaP system cannot be realized. Therefore, it is important to investigate whether the buffer is grown coherently or not. Calculated critical thickness of ZnS grown on GaP is about 130 Å by the Matthews and Blakeslee's model or 1800 Å by the People and Bean's model. Therefore, 200 Å seems to be close to actual critical thickness. Lattice parameter
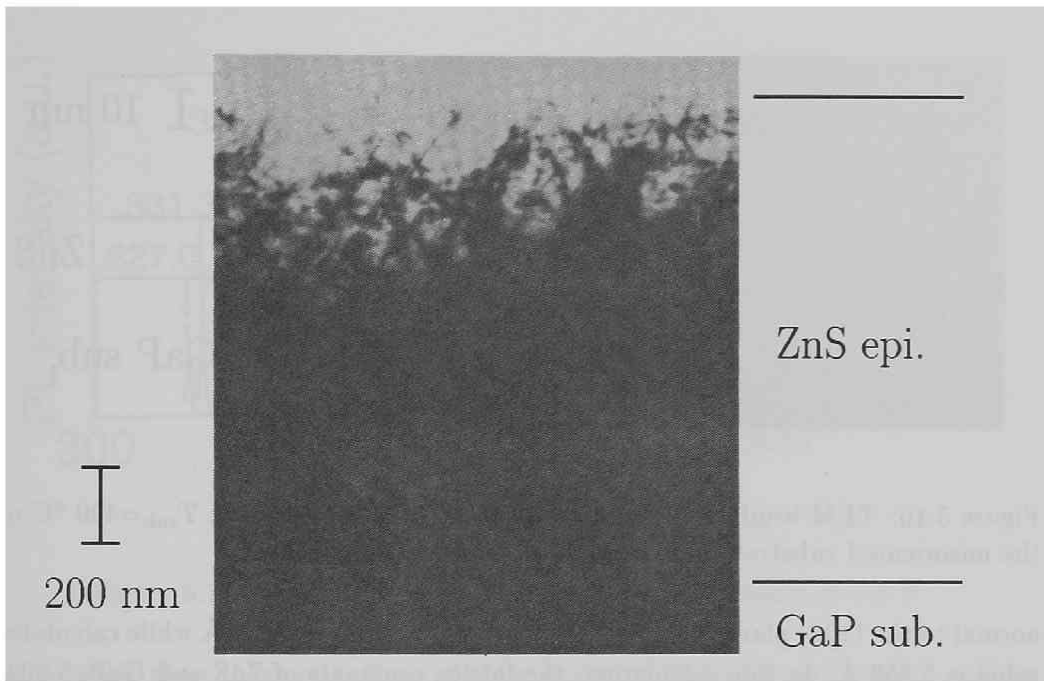
Figure 5.8: TEM bright field image of ZnS directly grown on (100) GaP misoriented 6° toward [01$\bar{1}$].
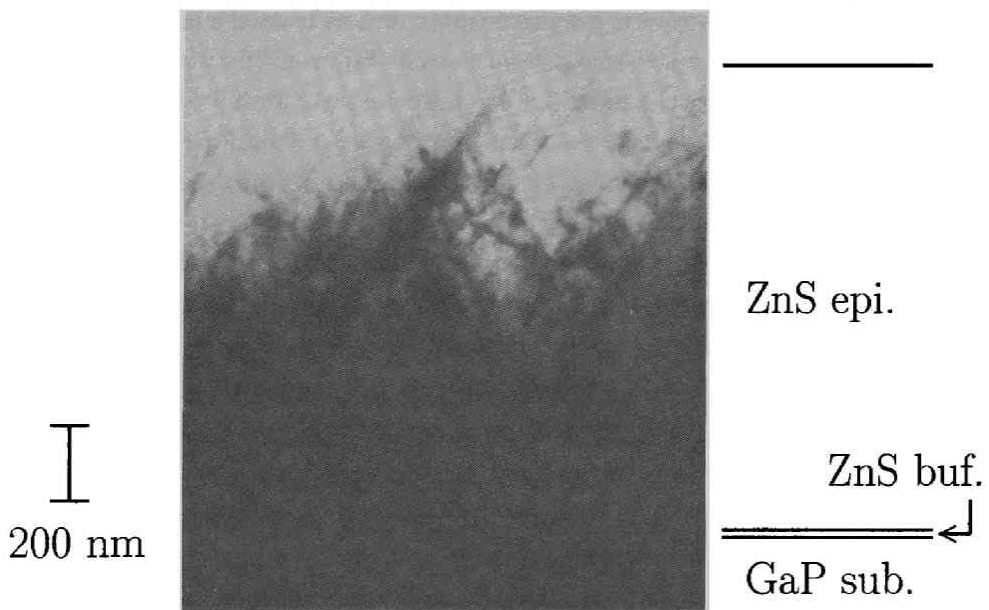

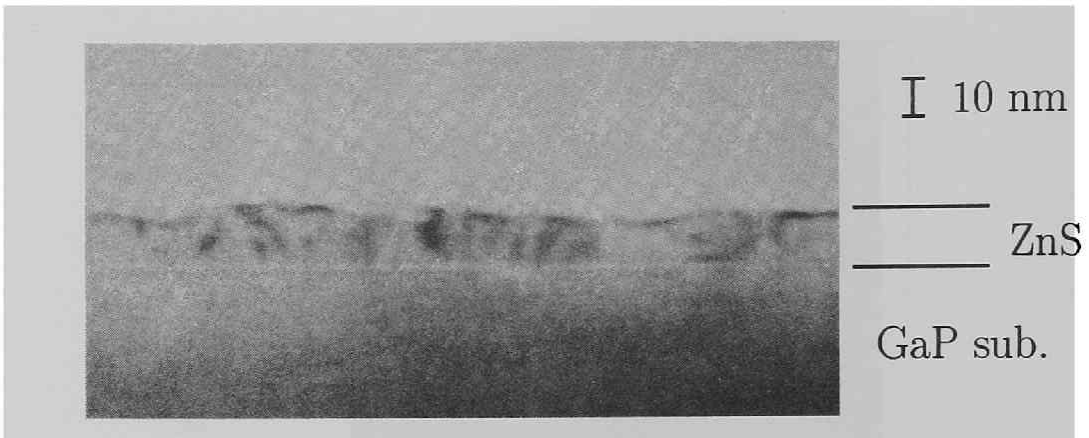Figure 5.9: TEM image of ZnS with the buffer layer on (100) GaP misoriented 6° toward [01$\bar{1}$].

Figure 5.10: TEM bright field image of 200 Å thick ZnS grown at T_{sub}=490 °C on the misoriented substrate. This layer was used as a buffer layer.

normal to the (100) plane measured by X-ray diffraction was 5.37 Å while calculated value is 5.358 Å. In this calculation, the lattice constants of ZnS and GaP, 5.4093 Å and 5.4506 Å, respectively, and the elastic stiffness constants of C_{11} and C_{12} of ZnS were used. A discrepancy between measured and calculated values may be due to uncertainty of the elastic constants. From this result only, it cannot be concluded that the ZnS buffer is pseudomorphic, but at least the lattice of the buffer is considerably distorted by the lattice-mismatch. Figure 5.10 shows TEM image of 200 Å thick ZnS grown on the misoriented GaP substrate at 490 °C, which was used as the buffer layer. In the figure, no defect can be seen. Therefore, it seems that the lattice of the 200 Å thick ZnS on GaP does not relax. Rather rough surface seems to be due to initial 3D nucleation, as observed by RHEED.

PL spectra were measured at 4.2 K using a He-Cd laser (3.814 eV, 325.0nm) as a excitation source with excitation power density of about 500 mW/cm^2. Figure 5.11 shows a typical PL spectrum of undoped ZnS. Similar spectra were observed from undoped ZnS grown in this chapter under wide range of the growth conditions. In other words, PL spectrum of undoped ZnS is not sensitive to growth conditions. In the exciton region, emission peaks were observed at 3.790 eV (327.0 nm) and 3.741 eV (331.3 nm), which have been assigned to I_2 (radiative recombination of excitons bound to neutral donors) and I_1 (radiative recombination of excitons bound to neutral acceptor), respectively. The peak energy of I_2 line corresponds to a shallow donor such as iodine [183, 206]. On the other hand, the peak energy of the I_1 line is smaller than $I_1{}^{Na}$ (3.783 eV) [207]. Therefore, it seems to be due to a deeper acceptor. However, FWHM values of the I_2 and I_1 lines are about 10 meV and
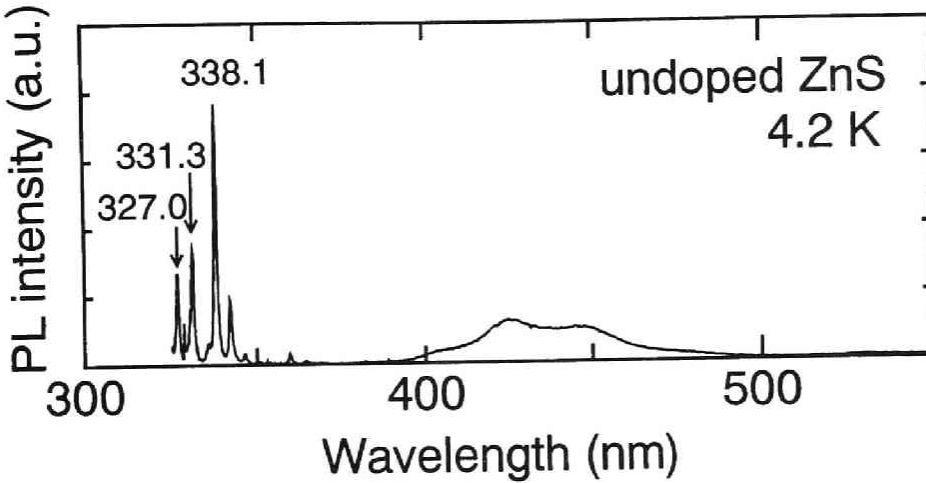
Figure 5.11: Typical PL spectrum of undoped ZnS taken at 4.2 K.

much larger than those of I_2 lines of chlorine-doped ZnS (3.7 meV) which will be described later. This suggests that I_2 and I_1 emissions in undoped ZnS are not due to a simple donor and an acceptor, respectively, but overlaps of plural emissions. The peak at 3.666 eV (338.1 nm) has been reported to be due to radiative recombination of free electrons and holes bound to acceptors (FB) [89], where acceptor species was shallow one such as sodium. However, since the corresponding shallow I_1 line was not observed, this assignment seems not to be applicable to this case. Similar PL spectra of undoped ZnS have been reported for the layers grown by MBE [202] and by MOVPE [89]. The fact that PL spectra is similar for the layers grown by different techniques indicates that emissions observed in undoped ZnS, i.e., I_2, I_1 and FB, may be related to some native intrinsic defects.

5.3.2   ZnSSe and ZnCdS

In this section, growth and characterization of ZnSSe and ZnCdS ternary alloys are described. First, ZnSSe ternary alloys were grown on the misoriented GaP substrates with and without ZnS buffers grown at T_{sub}=490 °C, and XRC of (400) diffraction peak was measured. Figure 5.12 shows the dependence of FWHM on sulfur composition for ZnSSe grown directly on the substrates (solid line). Dashed line in Fig. 5.12 shows inclination of the crystal axis of the epitaxial layers with respect to the substrates. FWHM values are rather large in the whole sulfur composition range and do not show the effect of lattice-matching to GaP. On the other hand, inclination is reduced around lattice-matched composition. Figure 5.13 shows FWHM

ZnSSe(1.2–1.4 μm)/GaP

Figure 5.12: FWHM of XRC and inclination of ZnSSe layers grown directly on the substrate as functions of S composition.
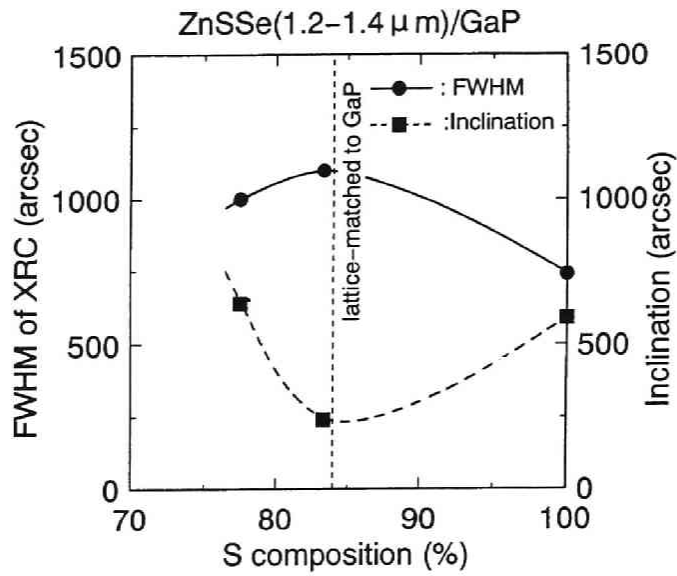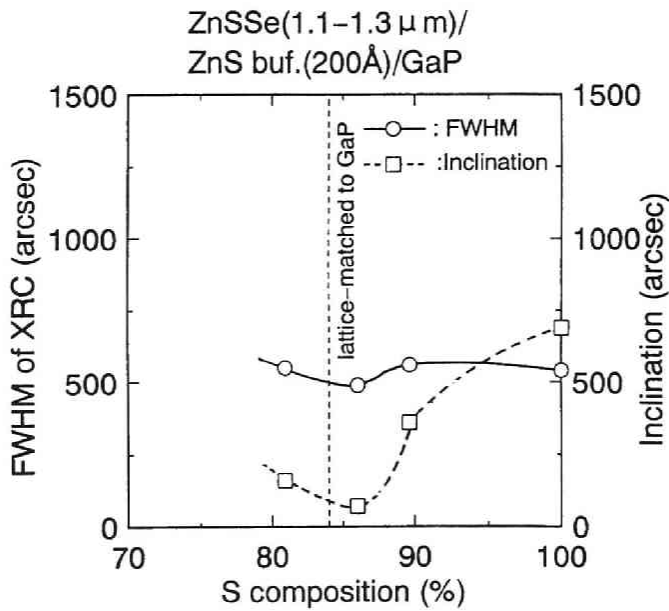
ZnSSe(1.1–1.3 μm)/
ZnS buf.(200Å)/GaP

Figure 5.13: FWHM of XRC and inclination of ZnSSe layers grown on the buffer as functions of S composition.
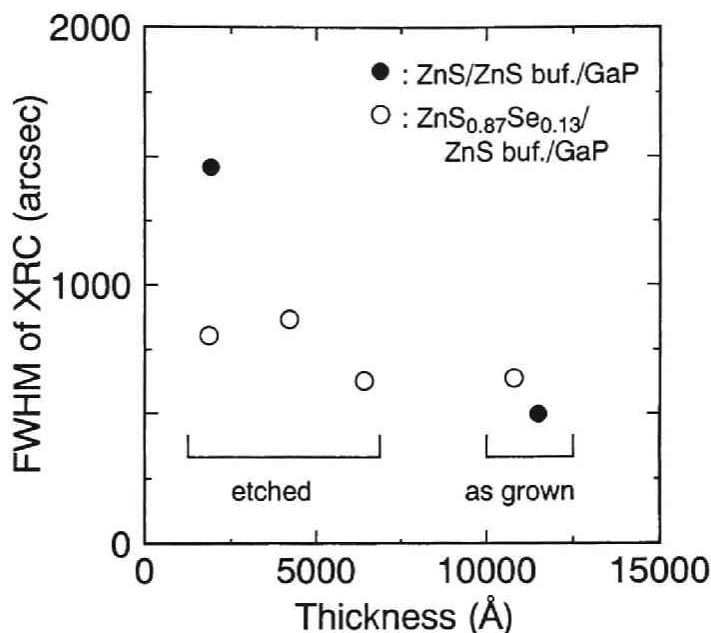
Figure 5.14: FWHM of ZnS and $ZnS_{0.87}Se_{0.13}$ vs. film thickness. As grown ZnS and ZnSSe layers were thinned by chemical etching and were characterized by XRC.

and inclination dependence for the layers grown on the ZnS buffer layers. Compared to Fig. 5.12, FWHM values are drastically reduced. This is most likely caused by the improved process in which twins are not produced. However, narrowing of XRC peaks by lattice-matching is still not observed.

To investigate the reason why lattice-matching effects on FWHM of XRC were not observed, thickness dependence of FWHM were assessed. Two samples, nearly lattice-matched $ZnS_{0.87}Se_{0.13}$ and ZnS, both of which were grown on the ZnS buffers, were chemically etched in H_2SO_4 and $K_2Cr_2O_4$ solution. Figure 5.14 shows the results. For as-grown layers (t=1.1 μm), FWHM for ZnS and ZnSSe are similar values of around 500–600 arcsec. However, when the layers were thinned to the thickness of 1900 Å, FWHM values for the ZnS increases to 1500 arcsec, while the value for ZnSSe show only slight increase to about 800 arcsec. From this result, we see that lattice-matching effects on FWHM of XRC can be observed for thin layers while the effects is screened by other factors for thick (t>1 μm) layers. If the unexpected large FWHM value of 500 arcsec for ZnSSe layers grown in the lattice-matching condition is due to the composition fluctuation during the growth, it corresponds to the fluctuation of more than 7 % in the solid composition of sulfur ([S]) or selenium

([Se]). For the growth of ZnS_ySe_{1-y} with $y\sim0.84$ which is nearly lattice-matched to GaP, since [Se] is relatively small, we can assume that [Se] is nearly proportional to $P_{Se}/(P_S+P_{Se})$, where P_{Se} and P_S denote beam pressure of selenium and sulfur flux, respectively, and typically $P_{Se}\ll P_S$ in this study. Therefore, for example, 10 % fluctuation in P_{Se} or P_S will result in the fluctuation in [Se] of about only 16 %×10 %=1.6 %, and thus 7 % fluctuation is too large to be explained by the variation of the beam flux, which was typically less than 10 % in this study. In fact, the position of the X-ray diffraction peak was almost the same when the layer was thinned by etching. Therefore, the fluctuation in composition is not the main factor. As described in the previous section, FWHM values of ZnS films are reduced down to about 300 arcsec with increasing the thickness to about 2.5 μm. If larger FWHM values of thinner ZnS films are only due to misfit dislocations, FWHM values for nearly lattice-matched ZnSSe are supposed to be at least less than 300 arcsec. However, the values remain at about 500 arcsec. Therefore, it is speculated that the ZnS(Se)/ZnS-buffer/GaP interface has unexpected influence on the quality of the ZnS(Se) epitaxial layers, and that this causes the relatively large FWHM values. One possibility for such influence is that the rather rough surface of the ZnS buffer
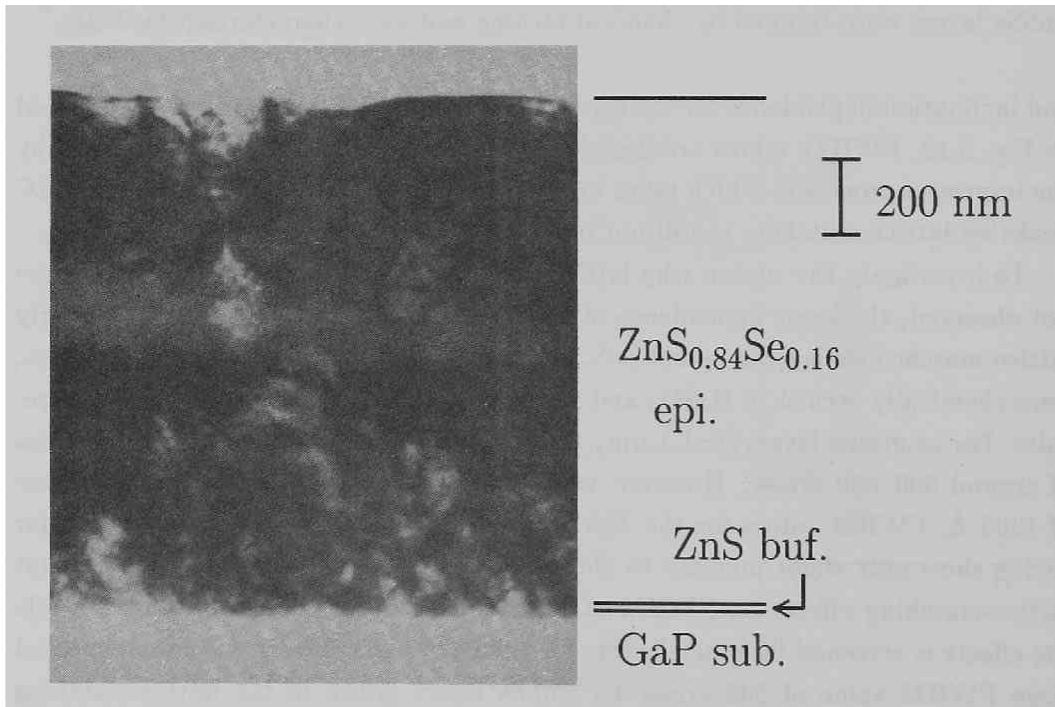
Figure 5.15: TEM bright field image of $ZnS_{0.84}Se_{0.16}$ grown on ZnS buffer.

as seen in Fig. 5.10 causes the defect formation in upper ZnS(Se), since the crystallographic quality of ZnS(Se) is sensitive to the surface smoothness, as discussed about twin formation in the previous section.

Figure 5.15 shows TEM bright field image of $ZnS_{0.84}Se_{0.16}$ grown on the ZnS buffer. Compared to ZnS, concentration of defects near the interface between epitaxial layer and substrate seems to be low, however, fairly large number of defects are seen in whole region, although the film is nearly lattice-matched to GaP. The fairly large FWHM values of XRC, therefore, can be attributed to these defects. It seems that the defects are generated at the epitaxial layer/substrate interface and spread toward the surface. Therefore, the quality of the interface between the epitaxial layer and the substrate should be improved further, although it became better to a certain extent by using the ZnS buffer grown at high substrate temperature. As for ZnSe grown on GaAs, it has been reported that the formation of Ga_2Se_3 interfacial layer results in good nucleation [208]. However, the nature of chemical bonding and its effect on the interfacial properties have not assessed yet for the ZnS(Se)/GaP system. We expect that the further modification of GaP surface and/or the utilization of some refined growth techniques such as cracking of a sulfur source [199, 203] would be effective for the two dimensional nucleation and also for the improvement of crystallographic quality of ZnS-based alloy layers.

Figure 5.16 shows a typical PL spectrum of ZnSSe taken at 4.2 K. Sulfur composition was 83 %. A relatively broad emission peaking at 359.0nm (3.453 eV) with
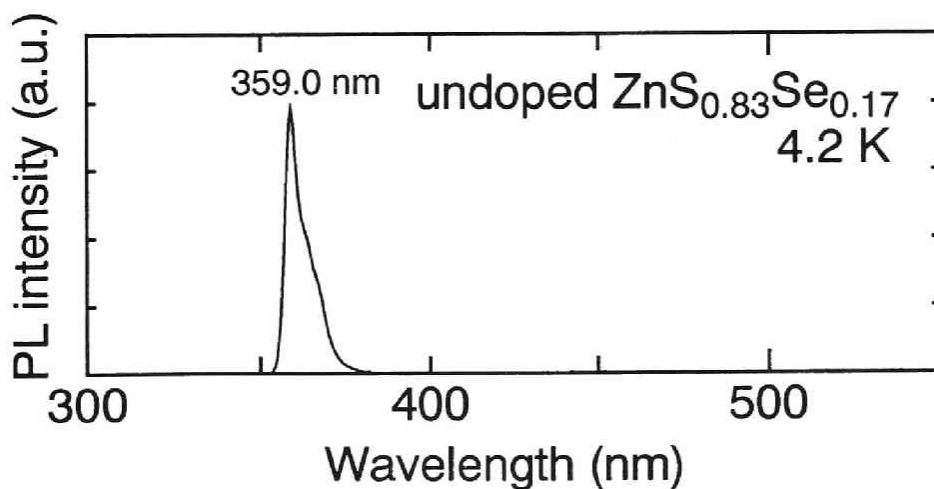
Figure 5.16: Typical 4.2 K PL spectrum of ZnSSe.
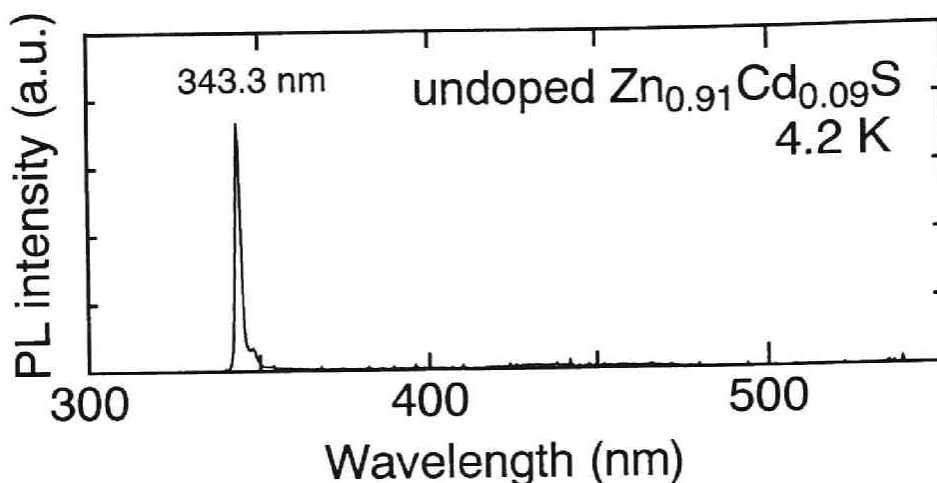
Figure 5.17: Typical 4.2 K PL spectrum of ZnCdS.

the tail in longer wavelength side was observed near the band edge expected from the composition. This emission probably consists of two or more emissions, although the origin of each emission is unknown at present. Any way, this emission was fairly strong compared with emissions from ZnS, which is possibly due to some localization of excitons to alloy disorder.

ZnCdS films were also grown. The effect of the ZnS buffer layers grown at high substrate temperature, i.e., the reduction of FWHM of XRC, was also observed for ZnCdS. However, FWHM of XRC of ZnCdS nearly lattice-matched to GaP were larger than those of ZnSSe. For example, FWHM of XRC for 1.2 μm thick $Zn_{0.92}Cd_{0.08}S$ on the ZnS buffer was 890 arcsec; this value is larger than those for ZnSSe and ZnS. This may be related to the increasing wurzite nature; since CdS has wurzite structure in bulk crystals, twin or related defects may be produced more easily as cadmium composition is increased. On the other hand, ZnCdS exhibited relatively sharp PL at 4.2 K compared with ZnSSe as shown in Fig. 5.17. The layer has cadmium composition of 9 %, and nearly lattice-matched to GaP. The peak located at 343.3 nm (3.611 eV) and had FWHM of 20 meV.

As mentioned in Chapter 2, two kinds of ternary alloys, ZnSSe and ZnCdS, both of which are lattice-matched to GaP, can be used as cladding layers in the device structure. However, in the present growth technique, ZnSSe seems to have higher crystallographic quality compared with ZnCdS. Therefore, ZnSSe was used in the device structure described in the following sections.

Table 5.1: Typical growth condition and solid composition of ZnCdSSe quaternary alloy.

Beam pressure ($\times 10^{-6}$ Torr)				Substrate temperature (°C)	Composition	
Zn	Cd	S	Se		x (Cd)	y (S)
2.8	0.8	9.5	0.8	330	0.23	0.23

5.3.3 ZnCdSSe

In ZnCdSSe/ZnSSe heterostructure systems on GaP substrates, ZnCdSSe is used as pseudomorphic active layers, and suffers from strain. As described in Chapter 2, ZnCdSSe active layers should have lattice-mismatch of more than 1 % to GaP in order to achieve sufficient carrier confinement. Therefore, the thickness of ZnCdSSe in actual heterostructures for light-emitting devices should be thin, *e.g.*, $t < 200$ Å. However, for optical or crystallographic characterization, the layer thickness is required to be larger than several thousand Å, where the lattice would be relaxed owing to lattice-mismatch and dislocation defects would be formed. In other words, the characterization of pseudomorphic ZnCdSSe is almost impossible. In this section, therefore, only growth conditions of ZnCdSSe are investigated for the composition control of ZnCdSSe in multi-layered device structures. Thick ($t > 1~\mu$m) ZnCdSSe layers were grown and solid composition of those layers were determined by energy dispersive X-ray analysis (EDX). Typical growth conditions and composition are shown in Table 5.1.

5.3.4 Chlorine and nitrogen doping

To date, there have been numbers of reports on doping to ZnS films. As concerns n-type conduction, the electron concentration (n) of about 10^{19} cm^{-3} or higher has been achieved by aluminum [182] and iodine [183,209] doping in MOVPE and aluminum doping in MBE [184]. On the other hand, in MBE of ZnSe, ZnCl$_2$ is commonly used and maximum electron concentration of the order of 10^{19} cm^{-3} can be obtained [210]. By doping with ZnCl$_2$ to ZnS in MBE, Cook *et al.* has reported maximum electron concentration of 3.8×10^{17} cm^{-3}. However, further improvement of electron concentration is expected by optimization of the growth conditions. In addition, sufficient flux of ZnCl$_2$ can be obtained at lower temperature (< 200 °C) compared with aluminum. This is a merit for avoiding contamination arising from degassing. Therefore, ZnCl$_2$ was used for n-type doping in this section.

As for p-type doping, lithium [62] and sodium [207] in MOVPE and phosphorus [63] in MBE have been used as impurities. By doping nitrogen using ammonia in VPE of ZnS, p-type conduction with hole concentration of 6×10^{18} cm^{-3} was reported [64] as mentioned in Chapter 1. For ZbSe, practical doping levels have been achieved using a rf nitrogen plasma source [46,47] and led to the realization of pn junction light-emitting devices, such as the first blue-green lasers [58,59]. From these results, it is considered that a nitrogen plasma source may also be effective for p-type doping of ZnS. However, the application of such technique for ZnS has never been reported. Therefore, a nitrogen plasma source excited by microwave was used for p-type doping in this section.

As for doping to ZnS-based alloy films, there have been few reports on both n-type as well as p-type doping. To fabricate pseudomorphic device structures on GaP, doping to ZnSSe ternary alloy is also investigated in this section.

First, Cl-doping to ZnS is described. Figure 5.18 shows electrical characteristics of Cl-doped ZnS as a function of T_{ZnCl_2} measured at RT. It seems that buffer layers do not have clear effects on electrical characteristics. High carrier concentration of 2×10^{18} cm^{-3} and low resistivity of 0.1 $\Omega\cdot$cm were achieved. The measured Hall mobility (μ) of about 30 cm$^2\cdot$V$^{-1}\cdot$s^{-1} for $n=2\times10^{18}$ cm^{-3} is comparable to the values
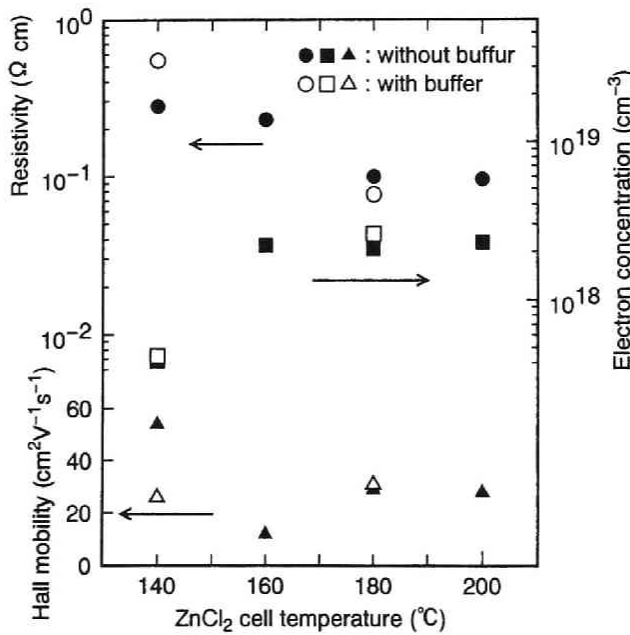
Figure 5.18: Electrical characteristics of Cl-doped ZnS vs. T_{ZnCl_2} measured at RT.

reported so far, typically 20–100 $cm^2 \cdot V^{-1} \cdot s^{-1}$ for n on the order of 10^{17} to 10^{19} cm^{-3} [182–184,202,209], or a little lower. According to the theoretical calculation by Ruda and Lai [211], the values of $\mu=30$ $cm^2 \cdot V^{-1} \cdot s^{-1}$ and $n=2 \times 10^{18}$ cm^{-3} give a high compensation ratio N_a/N_d of about 0.9, where N_a and N_d are acceptor and donor concentration, respectively. However, it should be noted that the mobility may be underestimated because the samples were not patterned as cloverleaf shape, and that the effect of the high concentration of defects as shown in TEM images (see Figs. 5.8 and 5.9) was not taken into account in the theoretical calculation. Therefore, the compensation ratio of 0.9 may not be reliable. Any way, for more detailed discussion further investigation such as measurement of temperature dependence of the mobility is necessary. Figure 5.19 shows PL spectra of Cl-doped ZnS grown with various T_{ZnCl_2}. For $T_{ZnCl_2}=160$, 180 and 200 °C, electrical characteristics are very similar, however, clear differences can be seen in the PL spectra. For T_{ZnCl_2} of 160 °C, strong exciton emission, which is probably assigned as I_2, was observed. However, it becomes weak and disappears as T_{ZnCl_2} is increased, although electrical characteristics are almost the same. Therefore, saturation in carrier concentration is probably due to some kind of compensation, *e.g.*, formation of self-activated (SA) centers (V_{Zn}-Cl_S) as observed in the deep level emission in PL spectra [212–214],
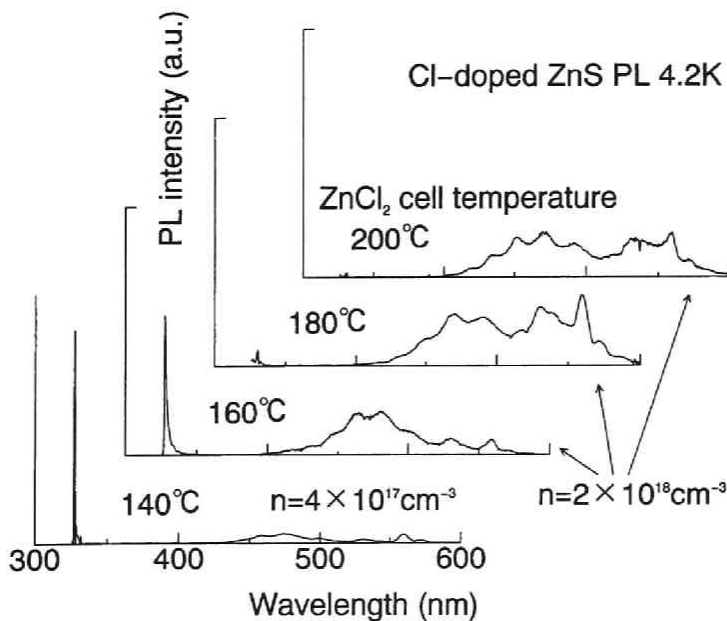
Figure 5.19: PL spectra of Cl-doped ZnS.
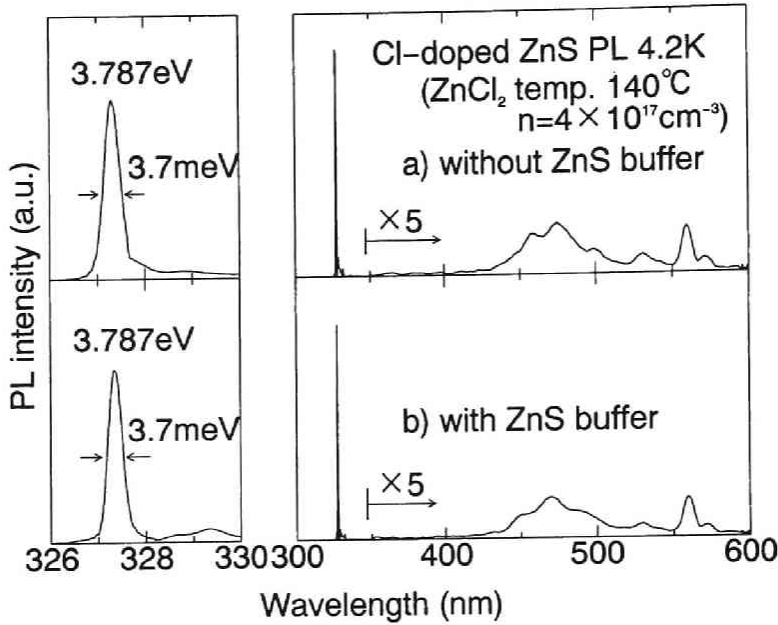
Figure 5.20: PL spectra of Cl-doped ZnS with and without buffer.

rather than saturation of incorporation. For T_{ZnCl_2} of 140 °C, very sharp I_2 emission was observed. As shown in Fig. 5.20, FWHM of the I_2 emission was as small as 3.7 meV, for the layers both with and without the buffers. Therefore, the effect of the buffers was not observed also in PL spectra.

ZnSSe was also doped with chlorine. $ZnS_{0.87}Se_{0.13}$ could be doped to $n=5\times10^{17}$ cm^{-3} when $T_{ZnCl_2}=160$ °C.

Second, nitrogen doping to ZnS was investigated. Flow rate of nitrogen was typically 0.2 sccm, and microwave input power was 160 W. ZnSe doped with nitrogen under this condition showed net acceptor concentration N_a-N_d of the mid 10^{17} cm^{-3}. However, all ZnS films doped with nitrogen showed very high resistivity. Some of the N-doped ZnS films exhibited sharp excitonic PL emissions at 4.2 K, although the emissions could not be identified as those related to the nitrogen acceptor substituting for sulfur assuming the simple effective mass theory. PL spectra of the rest of N-doped ZnS are very similar to those of undoped samples. Therefore, the formation of N-acceptor could not be confirmed by PL. It seems that nitrogen can hardly be incorporated into ZnS, which is a different situation from the case for ZnSe.

5.4 Fabrication of metal-insulator-semiconductor light-emitting diodes

To date, numbers of MIS LEDs using bulk ZnS [20, 22, 23, 25, 215] and epitaxial ZnS films [209, 216] have been reported. Among these devices, the highest external quantum efficiency is about 0.1 %. In all these devices, self-activated (SA) emission band [212–214], which corresponds to blue spectral region, was utilized. However, there has been no reports until now, to author's best knowledge, on the UV or near-UV electroluminescence from ZnS-based structures, except for the recent results on ZnCdS/ZnS multiple quantum wells (MQWs) on GaAs [76].

In this section, several types of MIS light-emitting devices are fabricated to obtain UV or near-UV emission. Although the quality of ZnS and ZnS-based alloys are still to be improved as described previously, evaluation of the potential of the material system proposed in this study is examined at the present stage. Four types of MIS LED are demonstrated. They are a ZnS-MIS LED, a ZnSSe-MIS LED, a ZnCdSSe/ZnSSe quantum-well (QW) MIS LED (QW-MIS LED) and a ZnCdSSe/ZnSSe QW LED with a N-doped layer (QW LED with N-doped layer). The former three devices use undoped layers as insulator (I) layers, while the last device uses a N-doped layer as an I layer.

The devices were fabricated on S-doped n-GaP whose orientation was (100) tilted 6° toward [01$\bar{1}$]. ZnS buffer layers were grown on the substrate at T_{sub}=490 °C, and doped with chlorine. However, resistivity in the buffer may be relatively high owing to low incorporation of chlorine as a result of the high T_{sub}. If this is the case, operating voltage will be increased by a few volts, considered from thickness of the buffer. In fact, in the structure of n-ZnS/ZnS buffer/n-GaP sub., turn-on voltage was about 2 V. Therefore, when the bias is applied to the device, about 2 V is probably applied to the buffer layer. A MIS structures was fabricated on the buffer layer. Semitransparent gold was formed on the top of the devices by vacuum evaporation, and used as a contact. Emission was detected through this semitransparent contact. An ohmic contact to the GaP substrate was made by the deposition of AuGe and Ni, followed by annealing in H_2 ambient at 320 °C.

5.4.1 ZnS-MIS LED

Figure 5.21 shows the schematic structure of the ZnS-MIS LED. Cl-doped n-type and undoped ZnS layer were used as a light emission layer and an I layer, respectively. Figure 5.22 shows electroluminescence (EL) spectra of the ZnS-MIS LED. At 77 K, two emission bands peaking at around 470 nm and 550 nm were observed. The

Semitransparent Au

Undoped ZnS
800Å

ZnS:Cl 0.9 μm
n=2×10^{18}cm^{-3}

ZnS:Cl buf. 200Å

GaP:S
n∼5×10^{17}cm^{-3}

AuGeNi
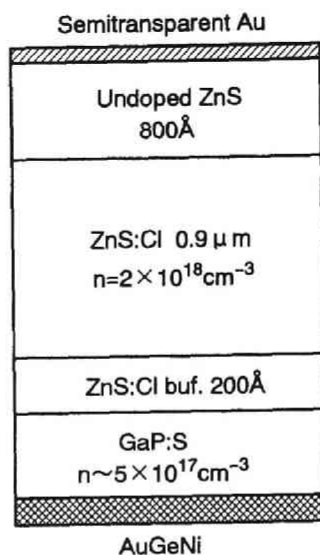
Figure 5.21: Cross section of ZnS-MIS LED.
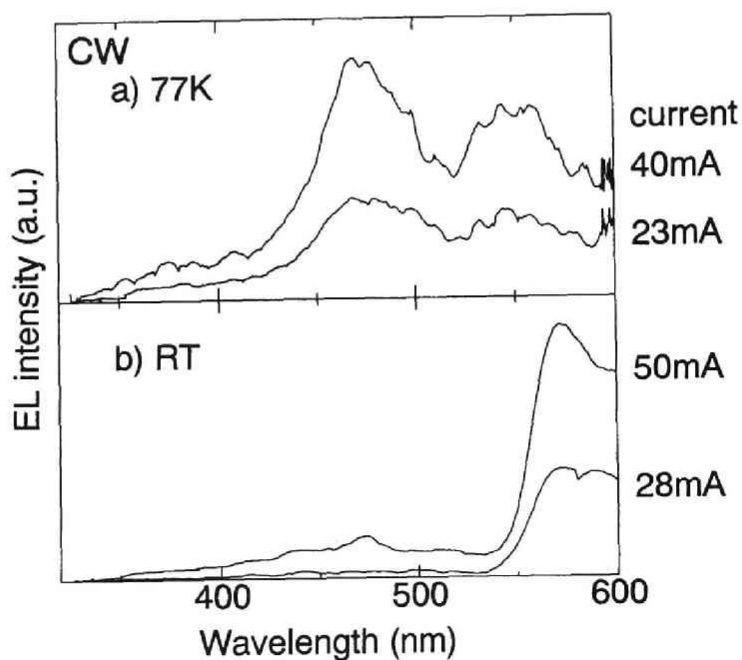
Figure 5.22: EL spectra of ZnS-MIS LED.

former is probably due to SA emission band of n-ZnS, while the latter seems to be emitted from the GaP substrate. In the wavelength range from 330 nm to 400 nm, broad UV emission was observed, although it is weaker than visible emission. At RT, emission from ZnS became weak, and that from GaP was dominant. The emission from GaP may be due to photoluminescence excited by emission from ZnS, and/or hole injection to n-GaP by avalanche breakdown in the high resistivity layer near the ZnS/GaP interface. If the GaP substrate is removed by the selective etching, emission from only ZnS would be possible. From these results, it is considered that strong UV emission cannot easily obtained from MIS LED using ZnS.

5.4.2 ZnSSe-MIS LED

Figure 5.23 shows the structure of the ZnSSe-MIS LED. The structure is the same as the ZnS-MIS LED except that epitaxial layers are ZnSSe nearly lattice-matched to GaP instead of ZnS. As shown in section 5.3.2, ZnSSe exhibits strong UV photoluminescence at low temperatures. Therefore, it is expected that ZnSSe-MIS LED emits UV light. Figure 5.24 shows EL spectra of the ZnSSe-MIS LED. At 77 K, UV emission peaking at around 360 nm was observed, although emission from GaP around 550 nm is still stronger. Visible emission ranging from 450 nm to 500 nm, which corresponds to deep level emission such as SA from n-ZnSSe, was also observed. However, at RT, the UV emission almost disappeared. This suggests that nonradiative recombination process dominated in the ZnSSe layer at RT.

Semitransparent Au

Undoped $ZnS_{0.88}Se_{0.12}$
1300Å

$ZnS_{0.88}Se_{0.12}$:Cl 1.2 μm
$n=5\times10^{17}cm^{-3}$

ZnS:Cl buf. 200Å

GaP:S
$n\sim5\times10^{17}cm^{-3}$

AuGeNi
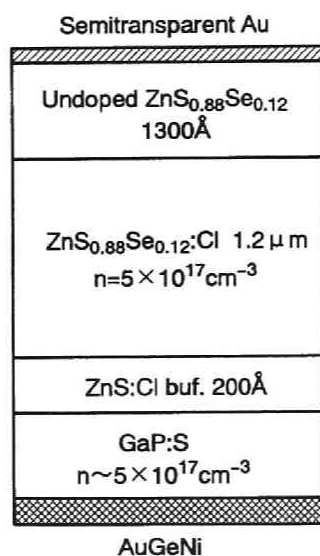
Figure 5.23: Cross section of ZnSSe-MIS LED.
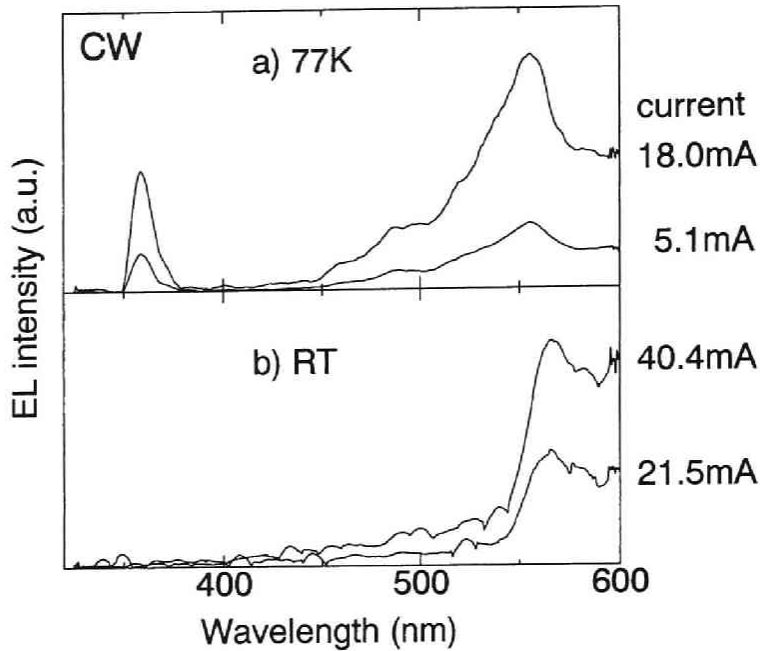
Figure 5.24: EL spectra of ZnSSe-MIS LED.

5.4.3 QW-MIS LED

Figure 5.25 shows the structure of the QW-MIS LED. A $Zn_{0.77}Cd_{0.23}S_{0.77}Se_{0.23}/$ $ZnS_{0.86}Se_{0.14}$ quantum well structure was grown at 330 °C on the ZnS buffer layer. It was assumed that alloy compositions of the quaternary well layer are the same as those of a single quaternary layer grown under the same conditions. To ensure the reproducibility of the composition, the single quaternary alloy and the QW-MIS LED were grown successively. The upper undoped ZnSSe layer was used as an I layer, and the lower ZnSSe layer was doped with Cl to achieve n-type conduction. $ZnS_{0.86}Se_{0.14}$ barrier layers are nearly lattice-matched to GaP, while the $Zn_{0.77}Cd_{0.23}S_{0.77}Se_{0.23}$ well layer has a lattice mismatch of 2.1% to the substrate, which gives the calculated critical thickness values of 36 Å and 155 Å using the Matthews and Blakeslee's (MB) model [161] and the People and Bean's (PB) model [162], respectively. The well layer thickness of 80 Å, therefore, is probably close to the actual critical thickness. Since no evidence of lattice relaxation, such as crosshatched surface morphology, was observed, the well layer was probably grown coherently on the ZnSSe layer. Figure 5.26 shows the calculated band lineup of the structure using the procedure described

Semitransparent Au

Undoped $ZnS_{0.86}Se_{0.14}$
1300Å

$Zn_{0.77}Cd_{0.23}S_{0.77}Se_{0.23}$ 80Å

$ZnS_{0.86}Se_{0.14}$:Cl 1.1 μm
$n = 5 \times 10^{17} cm^{-3}$

ZnS:Cl buf. 200Å

GaP:S
$n \sim 5 \times 10^{17} cm^{-3}$

AuGeNi
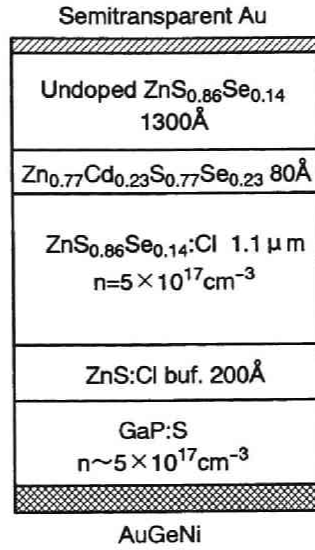
Figure 5.25: Cross section of QW-MIS LED.

4.2K

$ZnS_{0.86}Se_{0.14}$ $ZnS_{0.86}Se_{0.14}$
$Zn_{0.77}Cd_{0.23}S_{0.77}Se_{0.23}$

$\Delta E_c = 227 meV$

$\Delta a/a = 2.2\%$ Eg=3.217eV
(385.3nm)

$\Delta E_{v\,hh} = 185 meV$
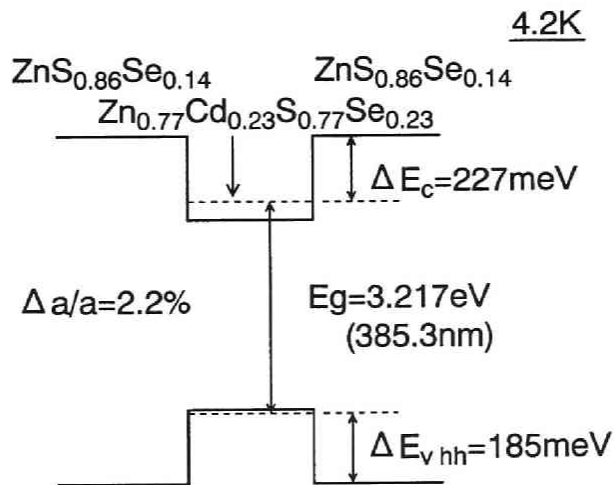
Figure 5.26: The calculated band lineup for the QW in the QW-MIS LED.

in Chapter 2. For comparison with 4.2 K PL, the values at 4.2 K was calculated. The calculated values for conduction- and valence-band offsets are 227 meV and 185 meV, respectively. One of the advantages of the ZnCdSSe/ZnSSe QW system is that both conduction- and valence-band offset can be large, as shown in Fig. 5.26.

A 4.2 K PL spectrum of the QW structure is shown in Fig. 5.27 where there are four major peaks at 358 nm, 384 nm, 398 nm and 416 nm. The differences in wavelength of the latter three peaks are very close to the interval of the peaks in the reflection spectrum caused by interference within the film. Therefore, it is suggested that the PL spectrum is modulated by the interference and that the true PL spectrum consists of two emission peaks which are located in the vicinity of 358 nm and 384 nm. The former peak is attributed to the emission from ZnSSe barrier layers because it coincides with the PL spectrum from the ZnSSe single layer. On the other hand, the wavelength of 384 nm agrees rather well with the estimated bandgap shown in Fig. 5.26. Therefore, the latter peak probably originates from the $Zn_{0.77}Cd_{0.23}S_{0.77}Se_{0.23}$ well layer. Although the well layer is very thin (80 Å), the emission from the well is clearly observed, indicating effective collection of the excited carriers into the well layer.
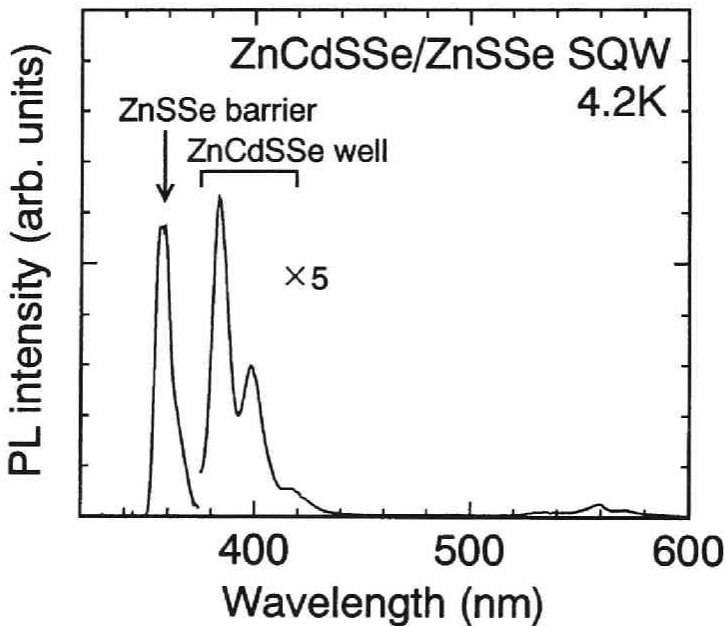
Figure 5.27: A 4.2 K PL spectrum of the QW structure.

Current-voltage (I-V) characteristics of the QW-MIS LED at RT and 77 K are shown in Fig. 5.28. Although the current transport mechanism is too complicated to be explained, the slopes of the I-V curves are seen to be almost the same between RT and 77 K, which strongly suggests that a tunneling process is related to current transport. Figure 5.29 shows the electroluminescence (EL) spectra of QW-MIS LED at 77 K as a function of the current density. When the sample was forward-biased (Au:+) at 77 K, two emission peaks at around 361 nm (A) and 391 nm (B) were observed. Owing to the interference, the spectra were modulated as in the case of the PL spectrum. By comparison with the PL spectra, it is reasonable to conclude that peaks A and B originate from radiative recombination in the ZnSSe barrier layers and the ZnCdSSe well layers, respectively. Emission from the GaP substrate in the range from 530 nm to 600 nm was also observed. At the current density of 180 mA/cm^2, the emission was very weak and peak A (from the ZnSSe barrier) was stronger than peak B (from the ZnCdSSe well). When the current density was increased to 360 mA/cm^2, peak B became stronger than peak A. At the current density of 5.4 A/cm^2 (current of 30 mA), peak B dominated the spectrum and
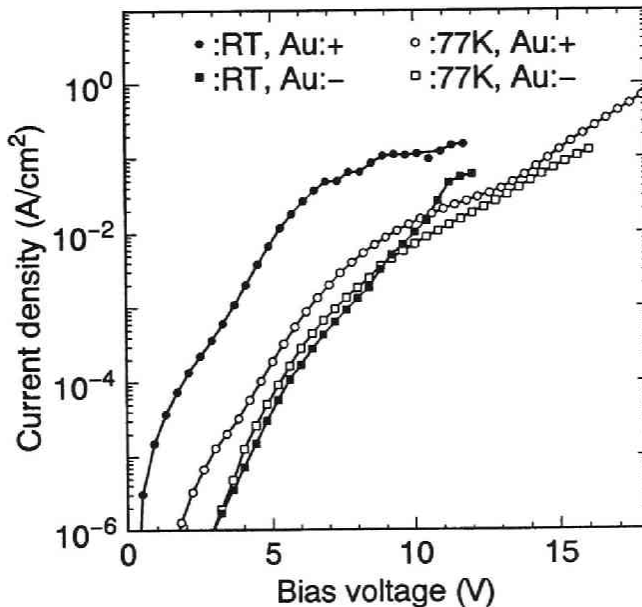
Figure 5.28: Current-voltage characteristics of the QW-MIS LED. Measurement temperature and polarity of the bias applied to the top Au contact are inserted in the figure.

corresponding purple emission was clearly observed with the naked eye through the top semitransparent Au contact. Figure 5.30 shows the photograph of the QW-MIS LED at 77 K. The process of EL from this type of MIS structure is probably explained by the following mechanism. The minority carriers (holes) are injected by tunneling from the Au electrode, as stated above. However, if the applied bias is low, i.e., the current density is low, injected holes can probably recombine with electrons in the I-ZnSSe layer before they reach the ZnCdSSe well layer because electric field in the I-layer is also low. With increasing the bias voltage, most injected holes drift to the well and recombine with electrons at the quaternary well layer, which results in efficient near-UV emission.

With the detection of the emission through the n-ZnSSe layer by removing a part of the GaP substrate, further improvement of the EL efficiency will be possible. At RT, the emission intensity of the near-UV light was weak at the present stage, which may be caused by the increase of the nonradiative recombination of the carriers or
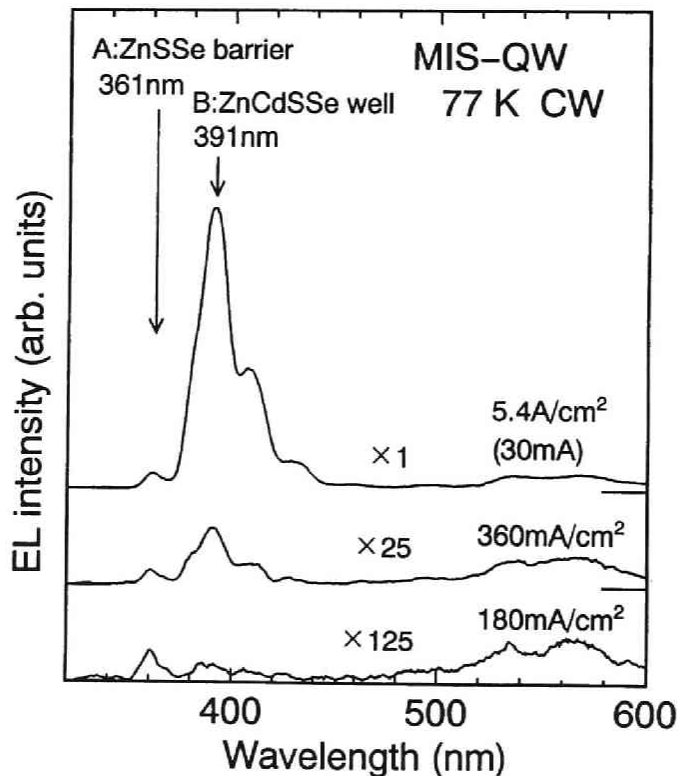
Figure 5.29: Electroluminescence spectra of the QW-MIS LED at 77 K for various current densities.
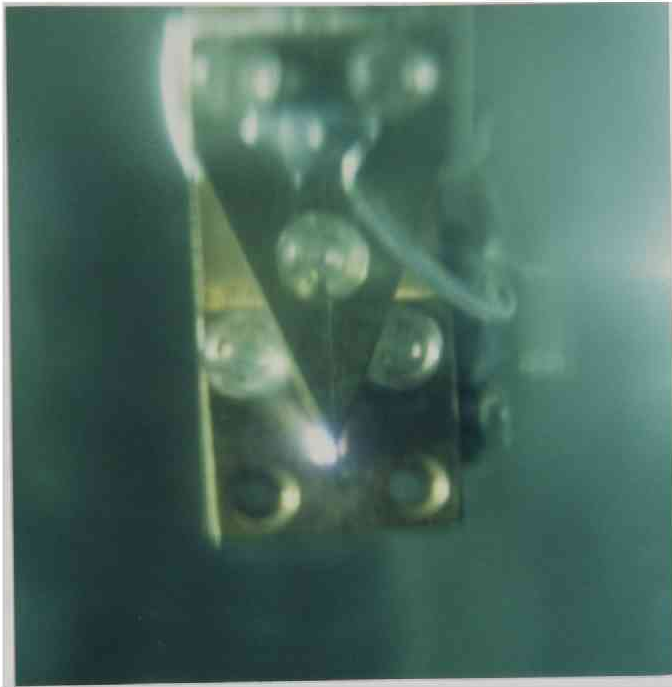
Figure 5.30: Photograph of QW-MIS LED at 77 K. Whitish purple emission was clearly observed.

insufficient injection of the holes to the well layer. Relatively large FWHM values of the PL peak at 4.2 K (about 120 meV) and the EL peak at 77 K (about 200 meV) may be caused by the fluctuation in alloy composition or well thickness or by large defect density, although we have not yet identified which is the main factor. In any case, it is suggested that further improvement in the crystal quality is needed. Moreover, it is necessary to attain low-resistance p-type conduction in ZnS as well as in ZnSSe or ZnCdS alloy with a large S composition, which will enable us to fabricate pn-junction near-UV or UV devices.

5.4.4 QW LED with N-doped layer

Figure 5.31 shows the structure. Compared with the QW-MIS LED mentioned above, thicker N-doped layer was used as an I layer instead of the undoped layer. As mentioned in section 5.3.4, N-doped layers were electrically high resistive. However, if the N-doped layers are high-resistive p-type, hole injection from N-doped layer can be expected, and some differences may be observed in *I-V* characteristics and

Semitransparent Au

$ZnS_{0.88}Se_{0.12}$:N $1.0\,\mu m$
$Zn_{0.77}Cd_{0.23}S_{0.77}Se_{0.23}$ 80Å
$ZnS_{0.88}Se_{0.12}$:Cl $1.3\,\mu m$ $n=5\times10^{17}cm^{-3}$
ZnS:Cl buf. 200Å
GaP:S $n\sim5\times10^{17}cm^{-3}$

AuGeNi

Figure 5.31: Schematic structure of QW LED with N-doped layer.

Figure 5.32: EL spectrum of the QW LED with N-doped layer.

EL spectra of the QW LED with N-doped layer, compared with those of the QW-MIS LED. Figure 5.32 shows EL spectrum of the QW LED with N-doped layer. Being different from EL from the MIS device, emission from the ZnCdSSe well was not clearly observed especially when the bias voltage was low. This result suggests that the emission originated from the N-doped ZnSSe layer owing to hole injection from the electrode, and most of injected holes recombined before they reached the QW, especially under the low bias, because N-doped layer was relatively thick. This implies that N-doped layer was not converted to p-type, which coincides with the results in section 5.3.4. In addition,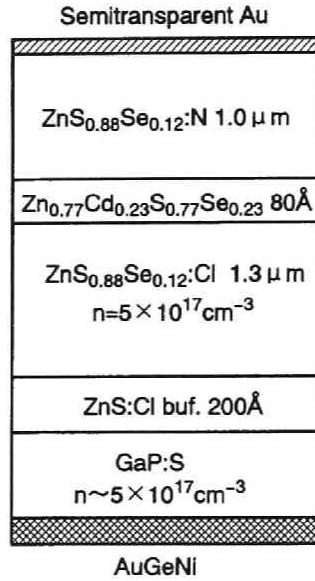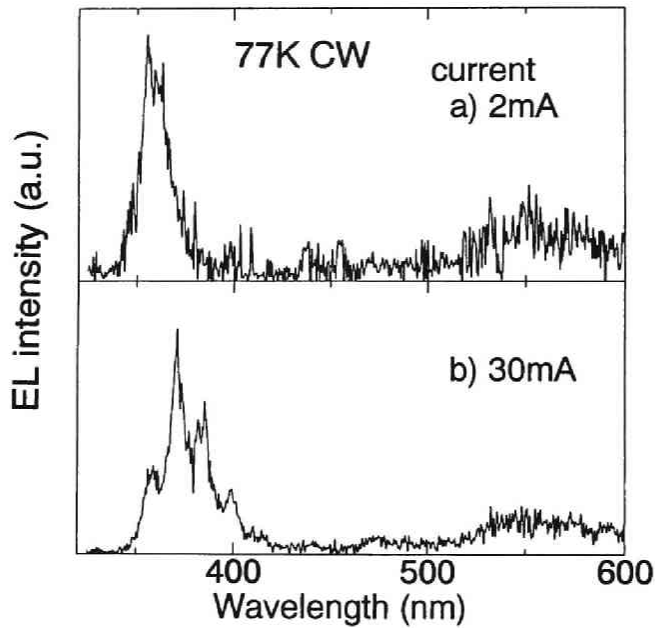 turn on voltage increased by about 10 V relative to the QW-MIS LED. This seems to be due to increased thickness of N-doped layer, because the voltage needed to cause tunneling is proportional to the thickness of high-resistive layer. This also suggests that the N-doped layer is as high-resistive as the undoped layers.

5.5 Summary

In this chapter, growth and characterization of ZnS-based crystals were described. The growth process of ZnS was investigated by *in situ* monitorring by RHEED. The film quality was characterized by XRC measurement and TEM observation, and relationship with growth process has been discussed. It was found that the use of ZnS buffer layer grown at high temperature improves the quality of upper epitaxial layers of not only ZnS but also ZnSSe ternary alloys. However, for alloys, lattice-matching effect to GaP, such as narrowing of XRC, was not clearly observed. On the other hand, it was found from the XRC measurement that quality of ZnCdS layers was worse than ZnSSe. n-type conduction control using $ZnCl_2$ was successfully achieved in ZnS and ZnSSe; minimum resistivity was about 0.1 Ω·cm at $n=2\times10^{18}$ cm^{-3}. However, the epitaxial layers doped with nitrogen using microwave-excited-plasma remained high resistive, even if the doping was carried out under the condition where the effective doping was achieved in ZnSe ($N_a-N_d>10^{17}$ cm^{-3}).

On the basis of these results, light-emitting devices which consists of MIS structures were fabricated. From the ZnCdSSe/ZnSSe QW-MIS LED, strong near-UV emission was observed at 77 K. This is the first observation of near-UV electroluminescence from pseudomorphic ZnS-based structures on GaP substrates, and strongly suggests high potential of ZnCdSSe system for the application to UV/near-UV light-emitting devices. However, more effort is still needed to improve crystallographic quality and to achieve p-type conduction of these ZnS-based crystals.

Chapter 6

Conclusion

In this study, the utilization of ZnCdSSe quaternary alloys has been proposed for the structural improvement of blue/blue-green light-emitting devices toward the practical use and for the developement of new material system for UV/near-UV devices. On the basis of estimated physical parameters, a ZnSe-based structure on a GaAs substrate has been proposed for the blue/blue-green device, while a ZnS-based structure on a GaP substrate has been proposed for the UV/near UV device. For the construction of such structures, epitaxial layers were grown by metal-organic molecular beam epitaxy (MOMBE), gas-source molecular beam epitaxy (GSMBE) and molecular beam epitaxy (MBE), and were characterized in terms of crystallographic, optical and electrical properties.

In Chapter 2, structural design of short-wavelength light-emitting devices with ZnCdSSe quaternary alloys has been described. First, the physical parameters of ZnCdSSe quaternary system, such as, the lattice constant, bandgap and band-edge energy, were estimated from those of binary compounds. From this estimation, it was predicted that strained layer heterostructures have to be used for carrier confinent, which is necessary for the light emitting devices such as laser diodes. On the basis of these results, two types of pseudomorphic device structures have been proposed. One is the ZnSe-based structure on the GaAs substrate for the blue/blue-green spectral region, in which ZnCdSSe is used to increase flexibility in device design, and the other is the ZnS-based structure on the GaP substrate for the UV/near-UV region, in which desirable band-lineup is realized by using ZnCdSSe. The critical thickness of the strained layer and refractive indices of the constituent layers have also been estimated. These results suggest that the ZnCdSSe quaternary alloy will be useful for the short-wavelength light-emitting devices.

In Chapter 3, MOMBE and characterization of ZnCdSSe quaternary alloys and ZnSe-based heterostructures were described. ZnCdSSe quaternary alloys were grown

by MOMBE for the first time. The solid composition of $Zn_{1-x}Cd_xS_ySe_{1-y}$ could be controlled by changing source supply in the composition range of $0 \leq x \leq 0.1$ and $0 \leq y \leq 0.25$. Reflection high-energy electron diffraction (RHEED) intensity oscillation was observed during the growth of ZnCdSSe on GaAs, which indicated two dimensional growth mode. ZnCdSSe layers thus grown exhibited excellent crystallographic and optical properties. For example, for a 0.96 μm thick $Zn_{0.95}Cd_{0.05}S_{0.15}Se_{0.85}$ layer, which is nearly lattice-matched to the GaAs substrate, the full-width at half maximum (FWHM) of (400) X-ray rocking curve (XRC) was as small as 40 arcsec, and a 4.2 K photoluminescence (PL) spectrum was dominated by exciton emission. In addition, optically pumped lasing was observed in the multi-layered structure using ZnCdSSe at 77 K. The threshold excitation intensity was as low as 18 kW/cm^2. From these results, it was shown that the ZnCdSSe system grown by the MOMBE technique has high potential for the use in ZnSe-based light-emitting devices.

In Chapter 4, GSMBE and characterization of ZnS-based epitaxial layers and their heterostructures were described. The solid compositions of ZnSSe and ZnCdSSe with the large sulfur content could be well controlled. Some physical parameters of ZnCdSSe were investigated, and agreed with estimated values described in Chapter 2. A ZnCdSSe/ZnSSe double-heterostructure (DH structure) was also fabricated. From the active layer of the DH structure, photoluminescence was observed at 4.2 K, which suggests that carriers were confined in the active layer in accordance with band-lineup estimation. However, crystallographic quality of the epitaxial layers was rather poor; FWHM of XRC for about 1 μm thick layers was about 1000 arcsec. This may be related to the mechanism of the growth using hydrogen sulfide as a sulfur source. Therefore, it was suggested that an alternative sulfur source should be used to grow high quality epitaxial layers.

In Chapter 5, MBE and characterization of ZnS-based epitaxial layers using an elemental sulfur source was described. First, since MBE growth technique of such ZnS-based crystals on the GaP substrate is not well established, the relationship between growth process and film quality has been investigated for ZnS, by using RHEED, XRC measurement and transmission electron microscope observation. It was found that crystallographic quality is improved by using the ZnS buffer layer grown at high temperature onto the GaP substrate. This effect was also seen for the ZnSSe ternary alloy, however, lattice-matching effect was not clearly observed; FWHM of XRC was almost constant at about 500 arcsec for about 1 μm thick layers irrespective of sulfur composition. This may result from the imperfect interface of the epitaxial layer and the substrate. n-type conduction control was successfully achieved by chlorine doping. The resistivity at room temperature

could be reduced down to 0.1 $\Omega\cdot$cm, when the electron concentration was 2×10^{18} cm^{-3}. On the other hand, p-type conduction was not obtained by nitrogen doping with microwave-excited nitrogen plasma, unlike the case for ZnSe. On the basis of these results, metal-insulator-semiconductor light-emitting diodes (LEDs) were fabricated. Strong near-UV emission was observed from the LED with the pseudo-morphic ZnCdSSe/ZnSSe quantum well at 77 K. These results strongly suggest high potential of the ZnCdSSe/ZnSSe on GaP system for the application to UV/near-UV light emitting devices.

It is considered that the results obtained in this study are very useful for the de-velopement of short-wavelength light-emitting devices made from the wide-bandgap II-VI semiconductor. However, especially for UV/near-UV devices, further investi-gation for the improvement of crystallographic quality and the realization of p-type conduction in ZnS-based crystals is still needed. And these are the subject in future.

References

[1] Sg. Fujita, Oyo Buturi **54** (1984) 39, [in Japanese].

[2] R. N. Bhargava, J. Cryst. Growth **117** (1992) 894.

[3] H. Kobayashi and S. Tanaka, *Proc. 5th Intern. Workshop on Electrolumnescence, Helsinki, 1990, Acta Polytechnica Scandinavica, Applied Physics Series No. 170*, p. 69, (1990).

[4] H. Sato, Oyo Buturi **61** (1992) 52, [in Japanese].

[5] G. E. Thomas, Philips Tech. Rev. **44** (1988) 51.

[6] D. Theis, Phys. Status Solidi b **79** (1979) 125.

[7] J. Camassel, J. Physique **35** (1974) suppl. 35-4 C3-67, [in French].

[8] H. Matsunami, Oyo Buturi **48** (1979) 565, [in Japanese].

[9] Y. Matsusita, K. Koga, Y. Ueda, and T. Yamaguchi, Oyo Buturi **60** (1991) 159, [in Japanese].

[10] H. Matsunami, Physica B **185** (1993) 65.

[11] M. Sano and M. Aoki, Oyo Buturi **52** (1983) 374, [in Japanese].

[12] H. Amano and I. Akasaki, Oyo Buturi **60** (1991) 163, [in Japanese].

[13] T. Matsuoka, J. Cryst. Growth **124** (1992) 433.

[14] T. D. Moustakas, T. Lei, and R. J. Molnar, Physica B **185** (1993) 36.

[15] R. N. Bhargava, J. Cryst. Growth **59** (1982) 15.

[16] M. D. Ryall and J. W. Allen, J. Phys. Chem. Solids **34** (1973) 2137.

[17] M. Yamaguchi, A. Yamamoto, and M. Kondo, J. Appl. Phys. **48** (1977) 196.

[18] M. Yamaguchi and A. Yamamoto, Jpn. J. Appl. Phys. **16** (1977) 77.

[19] X. W. Fan and J. Woods, IEEE Trans. Electron Devices **ED-28** (1981) 428.

[20] H. Katayama, S. Oda, and H. Kukimoto, Appl. Phys. Lett. **27** (1975) 697.

[21] L. G. Walker and G. W. Pratt, Jr., J. Appl. Phys. **47** (1976) 2129.

[22] N. B. Lukyanchikova, G. S. Pekar, N. N. Tkachenko, H. M. Shin, and M. K. Sheinkman, Phys. Status Solidi a **41** (1977) 299.

[23] N. B. Lukyanchikova, T. M. Pavelko, G. S. Pekar, N. N. Tkachenko, H. M. Shin, and M. K. Sheinkman, Phys. Status Solidi a **64** (1977) 697.

[24] T. Yokogawa, T. Taguchi, Sg. Fujita, and M. Satoh, IEEE Trans. Electron Devices **ED-30** (1983) 271.

[25] T. Taguchi and T. Yokogawa, J. Phys. D: Appl. Phys. **17** (1984) 1067.

[26] J. Nishizawa, K. Itoh, Y. Okuno, and F. Sakurai, J. Appl. Phys. **57** (1985) 2210.

[27] H. M. Manasevit, J. Electrochem. Soc. **118** (1971) 644.

[28] W. Stutius, Appl. Phys. Lett. **33** (1978) 656.

[29] W. Stutius, J. Cryst. Growth **59** (1982) 1.

[30] P. J. Wright and B. Cockayne, J. Cryst. Growth **59** (1982) 148.

[31] Sg. Fujita, Y. Tomomura, and A. Sasaki, Jpn. J. Appl. Phys. **22** (1983) 583.

[32] A. Yoshikawa, S. Yamaga, and K. Tanaka, Jpn. J. Appl. Phys. **23** (1984) L388.

[33] D. L. Smith and V. Y. Pickhardt, J. Appl. Phys. **46** (1975) 2366.

[34] T. Yao, Y. Miyoshi, Y. Makita, and S. Maekawa, Jpn. J. Appl. Phys. **16** (1977) 369.

[35] T. Yao, Y. Makita, and S. Maekawa, Appl. Phys. Lett. **35** (1979) 97.

[36] T. Yao, M. Ogura, S. Matsuoka, and T. Morishita, Jpn. J. Appl. Phys. **22** (1983) L144.

[37] K. Yoneda, Y. Hishida, T. Toda, H. Ishii, and T. Niina, Appl. Phys. Lett. **45** (1984) 1300.

[38] T. Yao and S. Maekawa, J. Cryst. Growth **53** (1981) 423.

[39] K. Yoneda, T. Toda, Y. Hishida, and T. Niina, J. Cryst. Growth **67** (1984) 125.

[40] T. Yasuda, I. Mitsuishi, and H. Kukimoto, Appl. Phys. Lett. **52** (1988) 57.

[41] A. Ohki, N. Shibata, and S. Zenbutsu, Jpn. J. Appl. Phys. **27** (1988) L909.

[42] I. Suemune, K. Yamada, H. Masato, T. Kanda, Y. Kan, and M. Yamanishi, Jpn. J. Appl. Phys. **27** (1988) 2195.

[43] H. Cheng, J. M. Depuydt, J. E. Potts, and T. L. Smith, Appl. Phys. Lett. **52** (1988) 147.

[44] K. Akimoto, T. Miyajima, and Y. Mori, Jpn. J. Appl. Phys. **28** (1989) 531.

[45] A. Taike, M. Migita, and H. Yamamoto, Appl. Phys. Lett. **56** (1990) 1989.

[46] R. M. Park, M. B. Troffer, C. M. Rouleau, J. M. DePuydt, and M. A. Haase, Appl. Phys. Lett. **57** (1990) 2127.

[47] K. Ohkawa, T. Karasawa, and T. Mitsuyu, J. Cryst. Growth **111** (1991) 797.

[48] R. B. Bylsma, W. M. Becker, T. C. Bonsett, L. A. Kolodziejski, R. L. Gunshor, M. Yamanishi, and S. Datta, Appl. Phys. Lett. **47** (1985) 1039.

[49] L. A. Kolodziejski, R. L. Gunshor, N. Otsuka, S. Datta, W. M. Becker, and A. V. Nurmikko, IEEE J. Quantum Electron. **QE-22** (1986) 1666.

[50] I. Suemune, K. Yamada, H. Masato, Y. Kan, and M. Yamanishi, Appl. Phys. Lett. **54** (1989) 981.

[51] G. Sun, K. Shahzad, J. M. Gaines, and J. B. Khurgin, Appl. Phys. Lett. **59** (1991) 310.

[52] K. Nakanishi, I. Suemune, Y. Fujii, Y. Kuroda, and M. Yamanishi, Appl. Phys. Lett. **59** (1991) 1401.

[53] H. Jeon, J. Ding, A. V. Nurmikko, H. Luo, N. Samarth, J. K. Furdyna, W. A. Bonner, and R. E. Nahory, Appl. Phys. Lett. **57** (1990) 2413.

[54] H. Jeon, J. Ding, A. V. Nurmikko, H. Luo, N. Samarth, and J. Furdyna, Appl. Phys. Lett. **59** (1991) 1293.

[55] Y. Kawakami, S. Yamaguchi, Y. -h. Wu, K. Ichino, Sz. Fujita, and Sg. Fujita, Jpn. J. Appl. Phys. **30** (1991) L605.

[56] H. Okuyama, F. Hiei, and K. Akimoto, Jpn. J. Appl. Phys. **31** (1992) L340.

[57] Y. Morinaga, H. Okuyama, and K. Akimoto, Jpn. J. Appl. Phys. **32** (1993) 678.

[58] M. A. Haase, J. Qiu, J. M. DePuydt, and H. Cheng, Appl. Phys. Lett. **59** (1991) 1272.

[59] H. Jeon, J. Ding, W. Patterson, A. V. Nurmikko, W. Xie, D. C. Grillo, M. Kobayashi, and R. L. Gunshor, Appl. Phys. Lett. **59** (1991) 3619.

[60] N. Nakayama, S. Ito, T. Ohata, K. Nakano, H. Okuyama, M. Ozawa, A. Ishibashi, M. Ikeda, and Y. Mori, Electron. Lett. **29** (1993) 1488.

[61] W. Xie, D. C. Grillo, R. L. Gunshor, M. Kobayashi, H. Jeon, J. Ding, A. V. Nurmikko, G. C. Hua, and N. Otsuka, Appl. Phys. Lett. **60** (1992) 1999.

[62] I. Mitsuishi, J. Shibatani, M.-H. Kao, M. Yamamoto, J. Yoshino, and H. Kukimoto, Jpn. J. Appl. Phys. **29** (1990) L733.

[63] M. Kitagawa, Y. Tomomura, K. Nakanishi, A. Suzuki, and S. Nakajima, *Collected abstracts of fifth international conference on II-VI compounds, Tamano, Okayama, Japan*, p. 152, (1991).

[64] S. Iida, T. Yatabe, and H. Kinto, Jpn. J. Appl. Phys. **28** (1989) 535.

[65] C. T. Walker, J. M. DePuydt, M. A. Haase, J. Qiu, and H. Cheng, Physica B **185** (1993) 27.

[66] W. Xie, D. C. Grillo, M. Kobayashi, L. He, R. L. Gunshor, H. Jeon, J. Ding, A. V. Nurmikko, G. C. Hua, and N. Otsuka, J. Cryst. Growth **127** (1993) 287.

[67] S. Hayashi, A. Tsujimura, S. Yoshii, K. Ohkawa, and T. Mitsuyu, Jpn. J. Appl. Phys. **31** (1992) L1478.

[68] Y. Kawaguchi, T. Ohno, and T. Matsuoka, *Extended abstracts of the 1992 International Conference on Solid State Devices and Materials, Tsukuba, 1992*, p. 345, (1992).

[69] S. Y. Wang, J. Simpson, H. Stewart, S. J. A. Adams, I. Hauksson, Y. Kawakami, M. R. Taghizadeh, K. A. Prior, and B. C. Cavenett, Physica B **185** (1993) 508.

[70] Z. Yu, J. Ren, Y. Lansari, B. Sneed, K. A. Bowers, C. Boney, D. B. Eason, R. P. Vaudo, K. J. Gossett, J. W. Cook Jr., and J. F. Schetzina, Jpn. J. Appl. Phys. **32** (1993) 663.

[71] H. Okuyama, K. Nakano, T. Miyajima, and K. Akimoto, Jpn. J. Appl. Phys. **30** (1991) L1620.

[72] T. Taguchi and Y. Endoh, Jpn. J. Appl. Phys. **30** (1991) L952.

[73] T. Taguchi, Y. Endoh, and Y. Nozue, Appl. Phys. Lett. **59** (1991) 3434.

[74] Y. Yamada, Y. Masumoto, J. Mullins, and T. Taguchi, Appl. Phys. Lett. **61** (1992) 2190.

[75] Y. Yamada, Y. Masumoto, and T. Taguchi, Physica B **191** (1993) 83.

[76] T. Taguchi, C. Onodera, Y. Yamada, and Y. Masumoto, Jpn. J. Appl. Phys. **32** (1993) L1308.

[77] Sz. Fujita, S. Hayashi, M. Funato, T. Yoshie, and Sg. Fujita, J. Cryst. Growth **107** (1991) 674.

[78] T. Ido, J. Electron. Mater. **9** (1980) 869.

[79] S. Shionoya, *Luminescence of inorganic solids*, ed. P. Goldberg, Chap. 4, Academic press, New York, (1966).

[80] *Physics and chemistry of II-VI compounds*, eds. M. Aven and J. S. Prener, North-Holland, Amsterdam, (1967).

[81] *II-VI semiconducting compounds, 1967 International Conference*, ed. D. G. Thomas, W. A. Benjamin, New York, (1967).

[82] S. Shionoya, Oyo Buturi **41** (1972) 869, [in Japanese].

[83] A. Sasaki, M. Nishiuma, and Y. Takeda, Jpn. J. Appl. Phys. **19** (1980) 1695.

[84] H. Nagai, S. Adachi, and T. Fukui, *III-V mixed crystals*, Corona, Tokyo, (1988), [in Japanese].

[85] I. Hayashi, M. B. Panish, P. W. Foy, and S. Sumski, Appl. Phys. Lett. **17** (1970) 109.

[86] M. Kobayashi, N. Mino, H. Katagiri, R. Kimura, M. Konagai, and K. Taka-hashi, Appl. Phys. Lett. **48** (1986) 296.

[87] H. Fujiyasu, A. Ishida, H. Kuwabara, S. Shinohara, and H. Murase, Surf. Sci. **142** (1984) 579.

[88] Sg. Fujita, Y. Matsuda, and A. Sasaki, Appl. Phys. Lett. **47** (1985) 955.

[89] Y. Kawakami, T. Taguchi, and A. Hiraki, J. Cryst. Growth **89** (1988) 331.

[90] Y. Endoh, Y. Kawakami, T. Taguchi, and A. Hiraki, Jpn. J. Appl. Phys. **27** (1988) L2199.

[91] Sz. Fujita, M. Funato, S. Hayashi, and Sg. Fujita, Jpn. J. Appl. Phys. **28** (1989) L898.

[92] Sz. Fujita, S. Hayashi, M. Funato, and Sg. Fujita, J. Cryst. Growth **99** (1990) 437.

[93] N. Samarth, H. Luo, J. K. Furdyna, S. B. Qadri, Y. R. Lee, A. K. Ramdas, and N. Otsuka, Appl. Phys. Lett. **54** (1989) 2680.

[94] N. Samarth, H. Luo, J. K. Furdyna, R. G. Alonso, Y. R. Lee, A. K. Ramdas, S. B. Qadri, and N. Otsuka, Appl. Phys. Lett. **56** (1990) 1163.

[95] H. Fujiyasu, T. Sasaya, M. Katayama, K. Ishino, A. Ishida, H. Kuwabara, Y. Nakanishi, and G. Shimaoka, Appl. Surf. Sci. **33/34** (1988) 854.

[96] K. Ichino, Y. -h. Wu, Y. Kawakami, Sz. Fujita, and Sg. Fujita, J. Cryst. Growth **117** (1992) 527.

[97] K. Ichino, Y. Kawakami, Sz. Fujita, and Sg. Fujita, Oyo Buturi **61** (1992) 117, [in Japanese].

[98] K. Ichino, Y. Kawakami, Sz. Fujita, and Sg. Fujita, Jpn. J. Appl. Phys. **32** (1993) Suppl. 32-1, 169.

[99] K. Ichino, K. Iwami, Y. Kawakami, Sz. Fujita, and Sg. Fujita, J. Electron. Mater. **22** (1993) 445.

[100] W. L. Roth, *Physics and Chemistry of II-VI Compounds*, eds. M. Aven and J. S. Prener, p. 127, North-Holland, Amsterdam, (1967).

[101] A. Ebina and T. Takahashi, J. Cryst. Growth **59** (1982) 51.

[102] A. Ebina, Y. Sato, and T. Takahashi, Phys. Rev. Lett. **32** (1974) 1366.

[103] T. Taguchi, T. Yokogawa, and H. Yamashita, Solid State Commun. **49** (1984) 551.

[104] K. Mohammed, D. A. Cammack, R. Dalby, P. Newbury, B. L. Greenberg, J. Petruzzello, and R. N. Bhargava, Appl. Phys. Lett. **50** (1987) 37.

[105] A. Ebina, E. Fukunaga, and T. Takahashi, Phys. Rev. **B10** (1974) 2495.

[106] H. Venghaus, Phys. Rev. **B19** (1979) 3071.

[107] P. J. Dean, D. C. Herbert, C. J. Werkhoven, B. J. Fitzpztrick, and R. N. Bhargava, Phys. Rev. **B23** (1981) 4888.

[108] R. Kiriyama and H. Kiriyama, *Structural Inorganic Chemistry*, p. 146, *Kyoritsu Series No. 16*, Kyoritsu, Tokyo, 3rd edition, (1979), [in Japanese].

[109] H. Tai, S. Nakajima, and S.Hori, J. Jpn. Inst. Metals **40** (1976) 474, [in Japanese].

[110] T. Ando, Kotai Buturi **21** (1986) 508, [in Japanese].

[111] S. W. Corzine and R.-H. Yanand L. A. Coldren, *Quantum well lasers*, ed. P. S. Zory, Jr., Chap. 1, Academic Press, San Diego, (1993).

[112] H. Kukimoto and S. Shionoya, J. Phys. Chem. Solids **29** (1968) 935.

[113] P. Lawaetz, Phys. Rev. **B4** (1971) 3460.

[114] J. M. Luttinger, Phys. Rev. **102** (1956) 1030.

[115] C. S. Wang and B. M. Klein, Phys. Rev. **B24** (1981) 3393.

[116] M.-Z. Huang and W. Y. Ching, J. Phys. Chem. Solids **46** (1985) 977.

[117] T. Nakayama, (1993), private communication.

[118] M. Aven, D. T. F. Marple, and B. Segall, J. Appl. Phys. **32** (1961) suppl., 2261.

[119] D. T. F. Marple, J. Appl. Phys. **35** (1964) 1879.

[120] J. L. Mertz, H. Kukimoto, K. Nassau, and J. W. Shiever, Phys. Rev. **B6** (1972) 545.

[121] T. Ohyama, E. Otsuka, T. Yoshida, M. Isshiki, and K. Igaki, Jpn. J. Appl. Phys. **23** (1984) L382.

[122] H. W. Hölscher, A. Nöthe, and Ch. Uihlein, Phys. Rev. **B31** (1985) 2379.

[123] M. Isshiki, T. Kyotani, K. Masumoto, W. Uchida, and S. Suto, Phys. Rev. **B36** (1987) 2568.

[124] G. E. Hite, D. T. F. Marple, M. Aven, and B. Segall, Phys. Rev. **156** (1967) 850.

[125] H. E. Ruda, J. Appl. Phys. (1986) 3516.

[126] T. Ohyama, K. Sakakibara, E. Otsuka, M. Isshiki, and K. Masumoto, Jpn. J. Appl. Phys. **26** (1987) L136.

[127] J. J. Hopfield and D. G. Thomas, Phys. Rev. **122** (1961) 35.

[128] W. A. Harrison, *Electronic Structure and the Properties of Solids*, W. H. Freeman and Company, San Francisco, (1980).

[129] R. G. Wheeler and J. O. Dimmock, Phys. Rev. **125** (1962) 1805.

[130] K. Shahzad, D. J. Olego, and C. G. Van de Walle, Phys. Rev. **B38** (1988) 1417.

[131] B. Segall and D. T. F. Marple, *Physics and chemistry of II-VI compounds*, eds. M. Aven and J. S. Prener, p. 345, North-Holland, Amsterdam, (1967).

[132] D. Berlincourt, H. Jaffe, and L.R. Shiozawa, Phys. Rev. **129** (1963) 1009.

[133] R. M. Martin, Phys. Rev. **B6** (1972) 4546.

[134] L. Soonckindt, D. Etienne, J. P. Marchand, and L. Lassabatere, Surface Science **86** (1979) 378.

[135] L. G. Suslina, D. L. Fedorov, S. G. Konnikov, F. F. Kodzhespirov, A. A. Andreev, and E. G. Sharlai, Sov. Phys. Semicond. **11** (1977) 1132.

[136] R. Hill, J. Phys. **C7** (1974) 521.

[137] H. Tai and S.Hori, J. Jpn. Inst. Metals **41** (1977) 33, [in Japanese].

[138] H. J. Lozykowski and V. K. Shastri, J. Appl. Phys. **69** (1991) 3235.

[139] S. Gonda, Oyo Buturi **55** (1986) 570, [in Japanese].

[140] R. L. Anserson, Solid-State Electon. **5** (1962) 341.

[141] A. D. Katnani and G. Margaritondo, J. Appl. Phys. **54** (1983) 2522.

[142] S. P. Kowalczyk, R. W. Grant, J. R. Waldrop, and E. A. Kraut, J. Vac. Sci. Technol. **B1** (1983) 684.

[143] R. Dingle, W. Wiegmann, and C. H. Henry, Phys. Rev. Lett. **33** (1974) 827.

[144] R. C. Miller, D. A. Kleinman, and A. C. Gossard, Phys. Rev. **B29** (1984) 7085.

[145] A. G. Milnes and D. L. Feucht, *Heterojunctions and Metal-Semiconductor Junctions*, Academic Press, New York, (1972).

[146] H. Kroemer, W.-Y. Chien, J. S. Harris, Jr., and D. D. Edwall, Appl. Phys. Lett. **36** (1980) 295.

[147] H. Kroemer, Surf. Sci. **174** (1986) 299.

[148] W. R. Frensley and H. Kroemer, Phys. Rev. **B16** (1977) 2642.

[149] W. A. Harrison, J. Vac. Sci. Technol. **14** (1977) 1016.

[150] J. Tersoff, Phys. Rev. **30** (1984) 4874.

[151] J. M. Langer and H. Heinrich, Phys. Rev. Lett. **55** (1985) 1414.

[152] C. G. Van de Walle and R. M. Martin, Phys. Rev. **B34** (1986) 5621.

[153] C. G. Van de Walle and R. M. Martin, Phys. Rev. **B35** (1987) 8154.

[154] C. G. Van de Walle, Phys. Rev. **B39** (1989) 1871.

[155] S.-H. Wei and A. Zunger, Phys. Rev. Lett. **59** (1987) 144.

[156] S.-H. Wei and A. Zunger, Phys. Rev. **B37** (1988) 8958.

[157] M. Sugawara, Phys. Rev. **B47** (1993) 7588.

[158] S. Adachi, J. Appl. Phys. **53** (1982) 5863.

[159] S. Adachi, Phys. Rev. **B35** (1987) 7454.

[160] Y. Kawakami, private communication.

[161] J. W. Matthews and A. E. Blakeslee, J. Cryst. Growth **27** (1974) 118.

[162] R. People and J. C. Bean, Appl. Phys. Lett. **47** (1985) 322.

[163] H. Mitsuhashi, I. Mitsuishi, M. Mizuta, and H. Kukimoto, Jpn. J. Appl. Phys. **24** (1985) L578.

[164] Y. -h. Wu, Y. Kawakami, Sz. Fujita, and Sg. Fujita, Jpn. J. Appl. Phys. **30** (1991) L555.

[165] H. Jeon, J. Ding, A. V. Nurmikko, W. Xie, D. C. Grillo, M. Kobayashi, R. L. Gunshor, G. C. Hua, and N. Otsuka, Appl. Phys. Lett. **60** (1992) 2045.

[166] W. T. Tsang, Appl. Phys. Lett. **39** (1981) 786.

[167] W. T. Tsang, Appl. Phys. Lett. **40** (1982) 217.

[168] Y. Arakawa and A. Yariv, IEEE J. Quantum Electron. **QE-22** (1986) 745.

[169] M. B. Panish, H. Temkin, and S. Sumski, J. Vac. Sci. Technol. **B3** (1985) 657.

[170] W. T. Tsang, Appl. Phys. Lett. **45** (1984) 1234.

[171] Y. Kawaguchi, H. Asahi, and H. Nagai, Jpn. J. Appl. Phys. **24** (1985) L221.

[172] H. Ando, A. Taike, M. Konagai, and K. Takahashi, J. Appl. Phys. **62** (1987) 1251.

[173] H. Oniyama, S. Yamaga, A. Yoshikawa, and H. Kasai, J. Cryst. Growth **93** (1988) 679.

[174] M. Migita, A. Taike, and H. Yamamoto, J. Appl. Phys. **68** (1990) 880.

[175] Sz. Fujita, N. Yoshimura, Y.-h. Wu, and Sg. Fujita, J. Cryst. Growth **101** (1990) 78.

[176] Y. -h. Wu, Y. Kawakami, Sz. Fujita, and Sg. Fujita, Jpn. J. Appl. Phys. **30** (1991) L451.

[177] K. Ichino, Y. -h. Wu, Y. Kawakami, Sz. Fujita, and Sg. Fujita, Jpn. J. Appl. Phys. **30** (1991) L1624.

[178] Y. Nannichi, Oyo Buturi **58** (1989) 1340, [in Japanese].

[179] Y. -h. Wu, Y. Kawakami, Sz. Fujita, and Sg. Fujita, Jpn. J. Appl. Phys. **29** (1990) L1062.

[180] *Semiconductor lasers*, eds. R. Ito and M. Nakamura, Chap. 3, Baihukan, Tokyo, (1989), [in Japanese].

[181] J. F. Schetzina, D. B. Eason, C. Boney, J. Ren, Z. Yu, J. W. Cook, Jr., and N. A. El-Masry, J. Cryst. Growth , to be published; presented at 6th International Conference on II-VI Compounds and Related Optoelectronic Materials, New Port, (1993).

[182] T. Yasuda, K.Hara, and H Kukimoto, J. Cryst. Growth **77** (1986) 485.

[183] S. Yamaga, A. Yoshikawa, and H. Kasai, J. Cryst. Growth **106** (1990) 683.

[184] M. Kitagawa, Y. Tomomura, , A. Suzuki, and S. Nakajima, J. Cryst. Growth **95** (1989) 509.

[185] I. Mitsuishi, H. Mitsuhashi, and H. Kukimoto, Jpn. J. Appl. Phys. **28** (1989) L275.

[186] T. Karasawa, K. Ohkawa, and T. Mitsuyu, J. Appl. Phys. **69** (1991) 3226.

[187] T. Karasawa, K. Ohkawa, and T. Mitsuyu, J. Cryst. Growth **95** (1989) 547.

[188] N. Matsumura, K. Ishikawa, J. Saraie, and Y. Yodogawa, J. Cryst. Growth **72** (1985) 41.

[189] N. Matsumura, M. Tsubokura, K. Miyagawa, N. Nakamura, and J. Saraie, J. Cryst. Growth **99** (1990) 446.

[190] K. A. Prior, J. M. Wallace, J. J. Hunter, S. J. A. Adams, M. J. L. S. Haines, M. Saoudi, and B. C. Cavenett, J. Cryst. Growth **101** (1990) 176.

[191] S. Kaneda, S. Sato, T. Setoyama, S Motoyama, M. Yokoyama, and N. Ota, J. Cryst. Growth **76** (1986) 440.

[192] O. Kanehisa, M. Shiiki, M. Migita, and H. Yamamoto, J. Cryst. Growth **86** (1988) 367.

[193] A. Yoshikawa, H. Oniyama, and H. Kasai, J. Cryst. Growth **95** (1989) 572.

[194] Y. -h. Wu, T. Toyoda, Y. Kawakami, Sz. Fujita, and Sg. Fujita, Jpn. J. Appl. Phys. **29** (1990) L144.

[195] T. Ohnakado, Y.-h. Wu, Y. Kawakami, Sz. Fujita, and Sg. Fujita, Jpn. J. Appl. Phys. **30** (1991) 1668.

[196] H. Oigawa, J. Fan, Y. Nannnichi, H. Sugahara, and M. Oshima, Jpn. J. Appl. Phys. **30** (1991) L322.

[197] A. Wakahara, X.L. Wang, and A. Sasaki, J. Cryst. Growth **124** (1992) 118.

[198] Y. -h. Wu, *Metalorganic molecular beam epitaxial growth and characterization of ZnSe-based II-VI semiconductors*, Ph. D. thesis, Kyoto University, (1991).

[199] Y. Tomomura, M. Kitagawa, A. Suzuki, and S. Nakajima, J. Cryst. Growth **99** (1990) 451.

[200] M. Yokoyama, K Kashiro, and S Ohta, J. Cryst. Growth **81** (1987) 73.

[201] M. Kitagawa, Y. Tomomura, K. Nakanishi, A. Suzuki, and S. Nakajima, J. Cryst. Growth **101** (1990) 52.

[202] J. W. Cook, Jr., D. B. Eason, R. P. Vaudo, and J. F. Schetzina, J. Vac. Sci. Technol. **B10** (1992) 901.

[203] M. Yoneta, M. Ohishi, H. Saito, and T. Hamasaki, J. Cryst. Growth **127** (1993) 314.

[204] K. Ichino, T. Onishi, Y. Kawakami, Sz. Fujita, and Sg. Fujita, J. Cryst. Growth , to be published; presented at 6th International Conference on II-VI Compounds and Related Optoelectronic Materials, New Port, (1993).

[205] K. Ichino, T. Onishi, Y. Kawakami, Sz. Fujita, and Sg. Fujita, Jpn. J. Appl. Phys. **32** (1993) L1200.

[206] Y. Kawakami, T. Taguchi, and A. Hiraki, J. Vac. Sci. Technol. **B5** (1987) 1171.

[207] T. Taguchi, Z. Kawazu, T. Ohno, and A. Sawada, J. Cryst. Growth **101** (1990) 294.

[208] J. Qiu, D. R. Menke, M. Kobayashi, R. L. Gunshor, D. Li, Y. Nakamura, and N. Otsuka, Appl. Phys. Lett. **58** (1991) 2788.

[209] Z. Kawazu Y. Kawakami, T. Taguchi, and A. Hiraki, Technol. Rep. Osaka Univ. **39** (1989) 1970.

[210] K. Ohkawa, T. Mitsuyu, and O. Yamazaki, J. Appl. Phys. **62** (1987) 3216.

[211] H. E. Ruda and B. Lai, J. Appl. Phys. **68** (1990) 1714.

[212] J. S. Prener and D. J. Weil, J. Electrochem. Soc. **106** (1959) 409.

[213] T. Koda and S. Shionoya, Phys. Rev. **136** (1964) A541.

[214] T. Taguchi, T. Yokogawa, Sg. Fujita, M. Satoh, and Y. Inuishi, J. Cryst. Growth **59** (1982) 317.

[215] T. Ohno, K. Kurisu, and T. Taguchi, J. Cryst. Growth **99** (1990) 737.

[216] S. Yamaga, Jpn. J. Appl. Phys. **30** (1991) 437.

Addendum

List of publications

I. Full length papers and Letters

(1) "Metalorganic molecular beam epitaxy of $Zn_{1-x}Cd_xS_ySe_{1-y}$ quaternary alloys on GaAs substrate"
K. Ichino, Y.-h Wu, Y. Kawakami, Sz. Fujita and Sg. Fujita,
Jpn. J. Appl. Phys. **30** (1991) pp. L1624–L1626.

(2) "Fabrication of ZnCdSSe alloys by MOMBE and their applications for double-hetero and quantum-well structures"
K. Ichino, Y.-h Wu, Y. Kawakami, Sz. Fujita and Sg. Fujita,
J. Cryst. Growth **117** (1992) pp. 527–531.

(3) "Growth and characterization of strained-layer quantum wells with wide gap ZnCdSSe alloy system"
K. Ichino, Y. Kawakami, Sz. Fujita and Sg. Fujita,
Jpn. J. Appl. Phys. **32** (1993) Suppl. 32-1 pp. 169–171.

(4) "Ultraviolet semiconductor laser structures with pseudomorphic ZnCdSSe quaternary alloys on GaP substrates"
K. Ichino, K. Iwami, Y. Kawakami, Sz. Fujita and Sg. Fujita,
J. Electron. Mater. **22** (1993) pp. 445–452.

(5) "Near-UV electroluminescence from a ZnCdSSe/ZnSSe metal-insulator-semiconductor diode on GaP grown by molecular beam epitaxy"
K. Ichino, T. Onishi, Y. Kawakami, Sz. Fujita and Sg. Fujita,
Jpn. J. Appl. Phys. **32** (1993) pp. L1200–L1202.

(6) "Growth of ZnS and ZnCdSSe alloys on GaP using an elemental sulfur source by molecular beam epitaxy"
K. Ichino, T. Onishi, Y. Kawakami, Sz. Fujita and Sg. Fujita,
to be published in J. Cryst. Growth.

II. Presentations at international conferences

(1) "Fabrication of ZnCdSSe alloys by MOMBE and their applications for double-hetero and quantum-well structures"

K. Ichino, Y.-h Wu, Y. Kawakami, Sz. Fujita and Sg. Fujita,

Fifth International Conference on II-VI compounds, Tamano, Okayama, (1991).

(2) "Growth and characterization of strained-layer quantum wells with wide gap ZnCdSSe alloy system"

K. Ichino, Y. Kawakami, Sz. Fujita and Sg. Fujita,

5th International Conference on High Pressure in Semiconductor Physics, Kyoto, (1992).

(3) "Growth of ZnS and ZnCdSSe alloys on GaP using an elemental sulfur source by molecular beam epitaxy"

K. Ichino, T. Onishi, Y. Kawakami, Sz. Fujita and Sg. Fujita,

6th International Conference on II-VI Compounds and Related Optoelectronic Materials, Newport, (1993).

III. Review article

(1) "Design and fabrication of II-VI semiconductor heterostructures"

K. Ichino, Y. Kawakami, Sz. Fujita and Sg. Fujita,

Oyo Buturi, **61** (1992) pp. 117–125 [in Japanese].

IV. Related publications

(1) "Optically pumped blue-green laser operation above room-temperature in $Zn_{0.80}Cd_{0.20}Se$-$ZnS_{0.08}Se_{0.92}$ multiple quantum well structures grown by metalorganic molecular beam epitaxy"

Y. Kawakami, S. Yamaguchi, Y.-h Wu, K. Ichino, Sz. Fujita and Sg. Fujita,

Jpn. J. Appl. Phys. **30** (1991) pp. L605–L607.

(2) "Growth of II-VI semiconductor quantum well structures under *in situ* RHEED observations",

Y.-h Wu, K. Ichino, Y. Kawakami, Sz. Fujita and Sg. Fujita,

J. Cryst. Growth **115** (1991) pp. 664–669.

(3) "Estimation of critical thickness and band lineups in ZnCdSe/ZnSSe strained-layer system for design of carrier confinement quantum well structures"
Y.-h Wu, <u>K. Ichino</u>, Y. Kawakami, Sz. Fujita and Sg. Fujita,
Jpn. J. Appl. Phys. **31** (1992) pp. 1737–1744.

(4) "Raman spectra of cubic $Zn_{1-x}Cd_xS$"
M. Ichimura, A. Usami, T. Wada, M. Funato, <u>K. Ichino</u>, Sz. Fujita and Sg. Fujita,
Phys. Rev. **B46** (1992) pp. 4273–4276.

(5) "Optical properties of ZnCdSe/ZnSSe strained-layer quantum wells"
Y.-h Wu, <u>K. Ichino</u>, Y. Kawakami, Sz. Fujita and Sg. Fujita,
Jpn. J. Appl. Phys. **31** (1992) pp. 3608–3614.

(6) "Photoluminescence excitation spectroscopy of the lasing transition in ZnCdSe-ZnSSe multiple quantum wells"
Y. Kawakami, B. C. Cavenett, <u>K. Ichino</u>, Sz. Fujita and Sg. Fujita,
Jpn. J. Appl. Phys. **32** (1993) pp. L730–733.